



UNIVERSITAT POLITÈCNICA
DE CATALUNYA
BARCELONATECH

Advanced pixel selection and optimization algorithms for persistent scatterer interferometry (PSI)

Feng Zhao

ADVERTIMENT La consulta d'aquesta tesi queda condicionada a l'acceptació de les següents condicions d'ús: La difusió d'aquesta tesi per mitjà del repositori institucional UPCCommons (<http://upcommons.upc.edu/tesis>) i el repositori cooperatiu TDX (<http://www.tdx.cat/>) ha estat autoritzada pels titulars dels drets de propietat intel·lectual **únicament per a usos privats** emmarcats en activitats d'investigació i docència. No s'autoritza la seva reproducció amb finalitats de lucre ni la seva difusió i posada a disposició des d'un lloc aliè al servei UPCCommons o TDX. No s'autoritza la presentació del seu contingut en una finestra o marc aliè a UPCCommons (*framing*). Aquesta reserva de drets afecta tant al resum de presentació de la tesi com als seus continguts. En la utilització o cita de parts de la tesi és obligat indicar el nom de la persona autora.

ADVERTENCIA La consulta de esta tesis queda condicionada a la aceptación de las siguientes condiciones de uso: La difusión de esta tesis por medio del repositorio institucional UPCCommons (<http://upcommons.upc.edu/tesis>) y el repositorio cooperativo TDR (<http://www.tdx.cat/?locale-attribute=es>) ha sido autorizada por los titulares de los derechos de propiedad intelectual **únicamente para usos privados enmarcados** en actividades de investigación y docencia. No se autoriza su reproducción con finalidades de lucro ni su difusión y puesta a disposición desde un sitio ajeno al servicio UPCCommons. No se autoriza la presentación de su contenido en una ventana o marco ajeno a UPCCommons (*framing*). Esta reserva de derechos afecta tanto al resumen de presentación de la tesis como a sus contenidos. En la utilización o cita de partes de la tesis es obligado indicar el nombre de la persona autora.

WARNING On having consulted this thesis you're accepting the following use conditions: Spreading this thesis by the institutional repository UPCCommons (<http://upcommons.upc.edu/tesis>) and the cooperative repository TDX (<http://www.tdx.cat/?locale-attribute=en>) has been authorized by the titular of the intellectual property rights **only for private uses** placed in investigation and teaching activities. Reproduction with lucrative aims is not authorized neither its spreading nor availability from a site foreign to the UPCCommons service. Introducing its content in a window or frame foreign to the UPCCommons service is not authorized (*framing*). These rights affect to the presentation summary of the thesis as well as to its contents. In the using or citation of parts of the thesis it's obliged to indicate the name of the author.



UNIVERSITAT POLITÈCNICA
DE CATALUNYA
BARCELONATECH

Advanced Pixel Selection and Optimization Algorithms for Persistent Scatterer Interferometry (PSI)

Author

Feng Zhao

Thesis Advisor

Jordi J. Mallorquí Franquet

Thesis by compendium of publications

submitted to the Universitat Politècnica de Catalunya (UPC) in
partial fulfillment of the requirements for the degree of
DOCTOR OF PHILOSOPHY

Ph.D. program on Signal Theory and Communications
CommSensLab - Unidad de Excelencia Maria de Maeztu
Barcelona, July 2019

Thesis written by Feng Zhao

Advanced Pixel Selection and Optimization Algorithms for Persistent Scatterer Interferometry (PSI)

Ph.D. program on Signal Theory and Communications

Copyright ©2019 by Feng Zhao, TSC, UPC, Barcelona, Spain

This work has been supported by the China Scholarship Council (Grant 201606420041), the Spanish Ministry of Economy, Industry and Competitiveness (MINECO), the State Research Agency (AEI) and the European Funds for Regional Development (EFRD) under project TEC2017-85244-C2-2-P, by the National Natural Science Foundation of China (Grant 51574221, 41874044). CommSensLab is Unidad de Excelencia Maria de Maeztu MDM-2016-0600 financed by the State Research Agency (AEI), Spain

献给我的爷爷、奶奶，我的父亲、母亲，我的弟弟，
我的女朋友王冰冰。

To my grandparents, my parents, my brother and my beloved
Bingbing Wang.

博学之，审问之，慎思之，明辨之，笃行之。

——孔子《中庸》

*Study Extensively, Enquire Accurately, Reflect Carefully, Discriminate
Clearly, Practice Earnestly.*

--- from Confucius in "The Doctrine of the Mean"

*Everybody is a genius. But if you judge a fish by its ability to climb a
tree, it will live its whole life believing that it is stupid.*

--- Albert Einstein

ACKNOWLEDGMENTS

Every journey has an end. This three-year stay in Universitat Politècnica de Catalunya (UPC) Barcelona to pursue my Ph.D. degree will for sure be one of the most beautiful and impressive journey in my life. It is impossible for me to enjoy this journey and complete the research work presented in this thesis without the support and help of many people. I hope these lines could express my gratitude to them.

First of all, my greatest gratitude goes to my supervisor professor Jordi J. Mallorquí. It is him who made this work possible and provided any support I need in my research. Without his guidance, encouragement, inspiration and patience, I absolutely could not complete this work. He taught me how to be a researcher, and his knowledge and vision on SAR interferometry are always helpful when I was in difficulties. He is always full of energy, his sense of humor and his passion on both science and life influence me a lot, which are priceless for me in the future.

I would like to thank my colleagues and friends Dr. Zhongbo Hu and Dr. Sen Du for their help and for the happy moments we shared. Dr. Zhongbo Hu bridged me and professor Jordi J. Mallorquí, and he helped me a lot for the application of the scholarship, accommodation in Barcelona, and starting my research work in UPC. I am really appreciate their help and the time we had together.

I would like to thank professors Yunjia Wang and Shiyong Yan of China University of Mining and Technology (CUMT) for their help and support during my master degree. They provided me the opportunity and guidance to the magic world of SAR. Besides, I would like to thank some graduated Ph.D. students of the CommSensLab as my research is based on works of them. There is no way for me to finish this work in this short period by starting from zero. Particularly, I think my work can be considered as a continuation of that of Dr. Rubén Iglesias and Dr. Dani Monells.

Last but not least, I would like to express my gratitude to my family and my girl friend Bingbing Wang. My parents trust and support me unconditionally all the time, and they are always trying their best to give me everything I need. My beloved Bingbing Wang has sacrificed a lot for me during this journey, and I am very grateful for all the things she has done for me. I hope we can together build a lovely family soon after my graduation.

This work has been financially supported in part by the China Scholarship Council under

Grant 201606420041, in part by the Spanish Ministry of Economy, Industry and Competitiveness (MINECO), the State Research Agency (AEI) and the European Funds for Regional Development (EFRD) under Project TEC2017-85244-C2-2-P, in part by the National Natural Science Foundation of China under Grant 51574221 and Grant 41874044, and in part by CommSensLab, Unidad de Excelencia Maria de Maeztu through the State Research Agency (AEI), Spain, under Grant MDM-2016-0600.

ABSTRACT

Ground deformation measurements can provide valuable information for minimization of associated loss and damage caused by natural and environmental hazards (e.g., earthquakes, landslides, ground subsidence and volcanism). As a kind of remote sensing technique, Differential Interferometry Synthetic Aperture Radar (DInSAR) or Persistent Scatterer Interferometry (PSI) SAR is able to measure ground deformation independent of light and weather with high spatial resolution, efficiently. Moreover, thanks to the short wavelength (typically 3-25 cm) and coherent nature of SAR system, the ground deformation monitoring accuracy of PSI techniques can reach up to millimeter level. However, low coherence could hinder the exploitation of SAR data, and high-accuracy deformation monitoring can only be achieved by PSI for high quality pixels slightly affected by decorrelation. ***Therefore, pixel optimization and identification of coherent pixels are crucial for PSI techniques as they directly determine the quality of final PSI products.*** In this thesis, advanced pixel selection and optimization algorithms have been investigated for PSI or Polarimetric PSI (PolPSI) applications.

Firstly, a full-resolution pixel selection method based on the Temporal Phase Coherence (TPC) has been proposed. This method first estimates noise phase term of each pixel at interferogram level. Then, for each pixel, its noise phase terms of all interferograms are used to assess this pixel's temporal phase quality (i.e., TPC). In the next, based on the relationship between TPC and phase Standard Deviation (STD), a threshold can be posed on TPC to identify high phase quality pixels. This pixel selection method can work with both deterministic or Permanent Scatterers (PSs) and Distributed Scatterers (DSs). To validate the effectiveness of the developed TPC pixel selection algorithm, it has been used to monitor the Canillo (Andorra) landslide with a super high resolution TerraSAR-X data set. The results show that the TPC method can obtain the highest density of valid pixels among the employed three approaches in this challenging area with X-band SAR data.

Second, to balance the polarimetric DInSAR phase optimization effect and the computational cost, a new PolPSI algorithm is developed. This proposed PolPSI algorithm is based on the Coherency Matrix Decomposition result to determine the optimal scattering mechanism of each pixel, thus it is named as CMD-PolPSI. CMD-PolPSI do not need to search for the solution within the full space of solutions, it is therefore much computationally faster than the classical Equal Scattering Mechanism (ESM) method, but with lower optimization performance. On the other hand, its opti-

mization performance outperforms the most computational efficient BEST method as a more extended solution space has been explored.

Third, an adaptive algorithm SMF-POLOPT has been proposed to adaptive filtering and optimizing PolSAR pixels for PolPSI applications. This proposed algorithm is based on PolSAR classification results to firstly identify Polarimetric Homogeneous Pixels (PHPs) for each pixel, and at the same time classify PS and DS pixels. After that, DS pixels are filtered by their associated PHPs, and then optimized based on the coherence stability phase quality metric; PS pixels are unfiltered and directly optimized based on the D_A phase quality metric. PolSAR filtering results show that SMF-POLOPT can simultaneously reduce speckle noise and retain structures' details. Meanwhile, SMF-POLOPT presents good interferogram optimization results, and thus it is able to obtain much higher densities of valid pixels for deformation monitoring than the ESM method.

To conclude, an innovative pixel selection method has been developed and tested by applying it to landslide monitoring, and two PolPSI algorithms have been proposed in this thesis. I hope the work presented in this thesis could make some contributions to the research area of *“Advanced Pixel Selection and Optimization Algorithms for Persistent Scatterer Interferometry (PSI) ”*.

RESUM

Les mesures de deformació del sòl poden proporcionar informació valuosa per minimitzar les pèrdues i els danys associats causats pels riscos naturals i ambientals. Com a tècnica de teledetecció, la interferometria de dispersors persistents (Persistent Scatter Interferometry, PSI) SAR és capaç de mesurar de forma eficient la deformació del terreny amb una alta resolució espacial. A més, la precisió de monitorització de la deformació del sòl de les tècniques PSI pot arribar a nivells del mil·límetre. No obstant això, una baixa coherència pot dificultar l'explotació de dades SAR i el control de deformació d'alta precisió només es pot aconseguir mitjançant PSI per a píxels d'alta qualitat. ***Per tant, l'optimització de píxels i la identificació de píxels coherents són crucials en les tècniques PSI.*** En aquesta tesi s'han investigat algorismes avançats de selecció i optimització de píxels.

En primer lloc, s'ha proposat un mètode de selecció de píxels de resolució completa basat en la coherència temporal de fase (Temporal Phase Coherence, TPC). Aquest mètode estima per primera vegada el terme de fase de soroll de cada píxel a nivell d'interferograma. A continuació, per a cada píxel, s'utilitzen els termes de la fase de soroll de tots els interferogrames per avaluar la qualitat de fase temporal d'aquest píxel (és a dir, TPC). A la següent, basant-se en la relació entre el TPC i la desviació estandard de fase (STD), es pot plantejar un llindar de TPC per identificar píxels de qualitat de fase alta. Aquest mètode de selecció de píxels es capaç de detectar tant els dispersors deterministes (PS) com els distribuïts (DS). Per validar l'eficàcia del mètode desenvolupat, s'ha utilitzat per controlar l'esllavissada de Canillo (Andorra). Els resultats mostren que el mètode TPC pot obtenir la major densitat de píxels vàlids, comparat amb els mètodes clàssics de selecció, en aquesta àrea difícil amb dades de SAR de banda X.

En segon lloc, per equilibrar l'efecte d'optimització de fase DInSAR polarimètrica i el cost de càlcul, es desenvolupa un nou algorisme de PolPSI. Aquest algorisme proposat de PolPSI es basa en el resultat de la descomposició de la matriu de coherència per determinar el mecanisme de dispersió òptim de cada píxel, de manera que es denomina CMD-PolPSI. CMDPolPSI no necessita buscar solucions dins de l'espai complet de la solució, per tant, és molt més eficient computacionalment que el mètode clàssic de mecanismes d'igualtat de dispersió (Equal Scattering Mechanism, ESM), però amb un efecte d'optimització no tant òptim. D'altra banda, el seu efecte d'optimització supera el mètode BEST, el que té un menor cost computacional.

En tercer lloc, s'ha proposat un algorisme adaptatiu SMF-POLOPT per al filtratge adaptatiu i l'optimització de píxels PolSAR per a aplicacions PolPSI.

Aquest algorisme proposat es basa en els resultats de classificació PolSAR per identificar primer els píxels homogenis polarimètrics (PHP) per a cada píxel i , alhora, classificar els píxels PS i DS. Després d'això, els píxels DS es filtren pels seus PHP associats i , a continuació, s'optimitzen en funció de la mètrica de qualitat de la fase d'estabilitat de coherència; els píxels classificats com PS no es filtren i s'optimitzen directament en funció de la mètrica de qualitat de la fase DA. SMF-POLOPT pot reduir simultàniament el soroll de la fase interferomètrica i conservar els detalls de les estructures. Mentrestant, SMF-POLOPT aconsegueix obtenir una densitat molt més alta de píxels vàlids per al seguiment de la deformació que el mètode ESM.

Per concloure, en aquesta tesi s'ha desenvolupat i provat un mètode de selecció de píxels, i s'han proposat dos algorismes PolPSI. Aquest treball contribueix a la recerca en "***Advanced Pixel Selection and Optimization Algorithms for Persistent Scatterer Interferometry (PSI)***".

CONTENTS

1	Introduction	1
1.1	Background	1
1.2	State of the Art	2
1.2.1	Pixel selection algorithms	2
1.2.2	Polarimetric Persistent Scatterer Interferometry	6
1.2.3	Permanent and Distributed Scatterers Joint Processing	8
1.3	Motivations and objectives	8
1.4	Thesis outline	9
2	Theoretical Basis	11
2.1	SAR Imaging	11
2.2	SAR Interferometry	14
2.3	Differential SAR Interferometry	16
2.4	Persistent Scatterer Interferometry	17
2.4.1	Linear Deformation Estimation Block (LDEB)	18
2.4.2	Non-linear Deformation Estimation Block (NLDEB)	20
2.5	Polarimetric Persistent Scatterers Interferometry (PolPSI)	21
2.5.1	Polarimetric SAR interferometry (PolInSAR)	21
2.5.2	Polarimetric Optimization for Deterministic Scatterers (PSs)	22
2.5.3	Polarimetric Optimization for Distributed Scatterers (DSs)	23
3	Results	25
3.1	A Temporal Phase Coherence Estimation Algorithm for the Selection of Persistent Scatterers	25
3.1.1	Introduction	25
3.1.2	Main Results	26
3.2	Landslide Monitoring Using PSI With Advanced Persistent Scatterers Selection Methods	28
3.2.1	Introduction	28
3.2.2	Main Results	28
3.3	Coherency Matrix Decomposition Based Polarimetric Persistent Scatterer Interferometry	31
3.3.1	Introduction	32
3.3.2	Main Results	32
3.4	Deterministic and Distributed Scatterers Joint Processing For Polarimetric PSI (PolPSI)	36

CONTENTS

3.4.1	Introduction	36
3.4.2	Main Results	37
4	Conclusions	41
4.1	Main Conclusions	41
4.2	Future Research Lines	46
5	Publications	49
5.1	Article 1. A Temporal Phase Coherence Estimation Algorithm and Its Application on DInSAR Pixel Selection	49
5.2	Article 2. Landslide monitoring using multi-temporal SAR interferometry with advanced persistent scatterers identification methods and super high-spatial resolution TerraSAR-X images	62
5.3	Article 3. Coherency Matrix Decomposition Based Polarimetric Persistent Scatterer Interferometry	86
5.4	Article 4. SMF-POLOPT: An Adaptive Multi-temporal Pol(DIn)SAR Filtering and Phase Optimization Algorithm for PSI Applications	100
5.5	List of Conference Articles	114
	Acronyms	115
	List of Figures	117
	Bibliography	119

1

CHAPTER 1

INTRODUCTION

1.1 Background

Ground deformation induced by crustal movement (e.g., earthquakes, volcanoes, etc.) or human activities (e.g., extractions of underground natural resources and constructions of underground infrastructures) may cause environmental or structural hazards [1–5]. These hazards caused by ground deformation could bring massive economic loss and may even threaten people’s life. It is therefore essential to monitor ground deformation with high accuracy and adequate spatial resolution. In this way, ground displacements can be better understood and managed to minimize the associated loss and damage. Conventional point-based monitoring techniques such as leveling and Global Positioning System (GPS) are with very high accuracy. However, ground deformation monitoring with these techniques are time and money consuming, especially for large areas. Moreover, some monitoring areas could be unreachable or very dangerous for these conventional techniques, as instruments have to be deployed and people have to come into the investigated areas.

As a remote sensing technique, Differential Interferometry SAR (DInSAR) can provide high resolution ground deformation monitoring results, efficiently [6, 7]. Theoretically, the ground deformation monitoring accuracy of DInSAR can reach up to millimeter level, which makes it a powerful tool in land motion detection [8]. However, there are some limitations, mainly due to temporal and geometrical decorrelations as well as atmospheric artifacts, that restrict the number of image pairs suitable for interferometric applications, and compromise its ground deformation monitoring accuracy [9, 10]. To overcome these limitations, Multi-Temporal InSAR (MTInSAR) or Persistent Scatterer Interferometry

(PSI) techniques have been proposed and developed in the last two decades, where a set of Synthetic Aperture Radar (SAR) images of the same area acquired on different dates are jointly analyzed to retrieve information of ground deformation [10–22].

As SAR pixels are affected by decorrelations [9], only a part of them are able to preserve high phase quality along the whole observing period. PSI only exploits these high phase quality pixels for deformation monitoring. Therefore, pixel optimization and selection is an essential step of all PSI techniques, and there are still some open research questions. It is actually a trade-off between density and phase quality of the selected pixels. On the one hand, as many as possible pixels should be selected to guarantee that more details of the ground deformation can be retrieved. Also the atmospheric artifacts will be better eliminated if selected pixels' density is higher, as they are assumed to be low-pass in the spatial domain. On the other hand, to ensure the accuracy of final products of PSI, only those pixels with high phase quality should be selected.

1.2 State of the Art

1.2.1 Pixel selection algorithms

1.2.1.1 Permanent scatterers (PSs) and distributed scatterers (DSs)

The reflected signal of a SAR pixel is the coherent sum of contributions from all scatterers within it. There are in general two kinds of scatterers, one are the so-called deterministic scatterers or Permanent Scatterers (PSs) and the other are known as Distributed Scatterers (DSs).

Permanent Scatterer (PS)s are those targets that are time-invariant and spatially concentrated, which are typically characterized by high reflectivities generated by dihedral or trihedral reflection or simple (deterministic) single-bounce scattering [23]. Man-made structures, boulders, and outcrops can all generate good PSs [16, 18].

Contrary to PSs, Distributed Scatterer (DS)s are those extended targets that are affected by angular decorrelation and with electromagnetic responses variable between satellite passes [20]. Vegetation, roads, debris, desert and water areas are typical DSs [16, 18]. Based on their phase characteristics, DSs can be further classified into Random Distributed Scatterer (RDS) and Coherent Distributed Scatterer (CDS). RDS is the kind of DS whose phase is totally randomly distributed between $[-\pi, \pi]$, like water areas, and thus it should be treated as noise; while CDSs are those scatterers with coherent information for small-baseline interferograms, for instance some roads or non-cultivated lands with short vegetation, and thus they could be used for information extraction in PSI.

Corresponding with the two kind of scatterers above-mentioned, there are two categories

of SAR pixels can be used for ground deformation monitoring, one are PS pixels and the other are CDS pixels. A pixel that is dominated by a PS is a PS pixel, as Fig. 1.1(a) shows. Since the dominant PS is much brighter than the background DSs within one PS pixel, it contributes mostly to (or determines) the final signal (i.e., amplitude and phase) of this pixel. And because this dominant PS's phase is with high Signal to Noise Ratio (SNR), the phase quality of this PS pixel is good as well. Thus, PS pixels, more particularly PS pixels' phases, can be utilized to extract underlying ground deformation signal [16, 18]. CDS pixels, on the other hand, contain many similar slowly changing distributed scatterers (CDSs), as Fig. 1.1(b) shows. These pixels contain coherent information in small-baseline interferograms, thus, they can be exploited for deformation inversion by using these small-baseline interferograms. Besides, one CDS pixel is usually surrounded by other neighboring CDS pixels with similar characteristics, as they are usually belong to same ground objects like roads or desert areas [18].

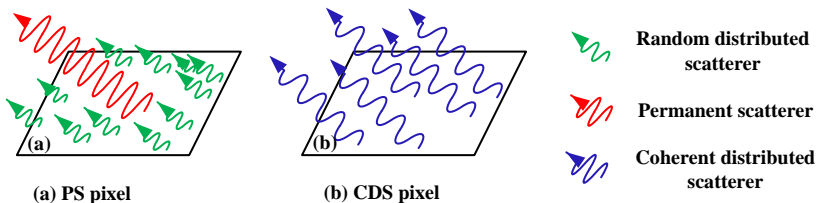


Figure 1.1: Two categories of pixels.

Correspondingly, two classical phase quality metrics, Dispersion of Amplitude (D_A) (better for PS pixel selection) and coherence stability (better for DS pixel selection), have been proposed to identify high quality pixels for PSI techniques. Each selection method explores a particular characteristic, thus they can be considered complementary. Other sophisticated methods [18] [20] have been also developed based on these two methods. Those closely related to this thesis will be introduced in the following sections.

1.2.1.2 Permanent scatterer pixel selection

(1) PS pixel selection by amplitude dispersion (D_A)

This PS pixel selection approach is based on the assumption that amplitude stable pixels are high phase quality pixels [10]. High reflectivity pixels which remain amplitude stable along the temporal span of the acquisitions exhibit a low D_A , defined as [10]

$$D_A = \sigma_A/m_A \quad (1.1)$$

where m_A and σ_A refer to the mean and the Standard Deviation (STD) of the temporal amplitude evolution, respectively. It should note that SAR images have to be radiometrically calibrated before calculating D_A by (1.1). Pixels with low values of D_A are associated with a low phase STD, as Fig. 1.2 (a) demonstrated [10]. Therefore, D_A can be used as the metric of phase stability.

D_A criterion allows to detect those pixels that are dominated by PSs, and the typical PSI technique that uses this criterion is the so-called PSInSAR algorithm [10]. This criterion can preserve the full resolution of a SAR image and it has no theoretical limitation on the length of interferometric baselines, as PS pixels are supposed to be slightly affected by both temporal and geometrical decorrelations. Nevertheless, it has the disadvantage of low density of selected pixels, especially in non-urbanized areas where DSs account for the majority. What is more, a large number of SAR images, usually more than 20 [10,24], are required to ensure the reliability of this method.

(2) PS Pixel selection in the spectral domain

Another PS pixel selection method, i.e., the Temporal Sublook Coherence (TSC) method, which is aimed at finding those point-like pixels that are highly spectral correlated, works in the spectral domain [19,25]. The rationale of this approach is that targets exhibiting high values of TSC (i.e., highly spectral correlated) are directly related to as point-like scatterers and, consequently, as high phase quality pixels [19,25]. Fig. 1.2 (b) shows the relationship between TSC and the phase STD. It can be seen from this figure that PS pixels with high phase quality (i.e., those pixels with low phase STD) can be selected by posing a threshold on the TSC. Comparing with D_A based pixel selection algorithm, this method has several advantages. On the one hand, it is able to work on a reduced number of SAR images, and the radiometric calibration is not required. On the other hand, it can detect targets which are stable in phase but with high amplitude fluctuations, like highly directive objects. By combing D_A and TSC selection method together, a significant increase of PS pixels' density can be obtained [19]. Despite the good performance of the TSC approach on pixel selection, it only allows the identification of deterministic point-like scatterers.

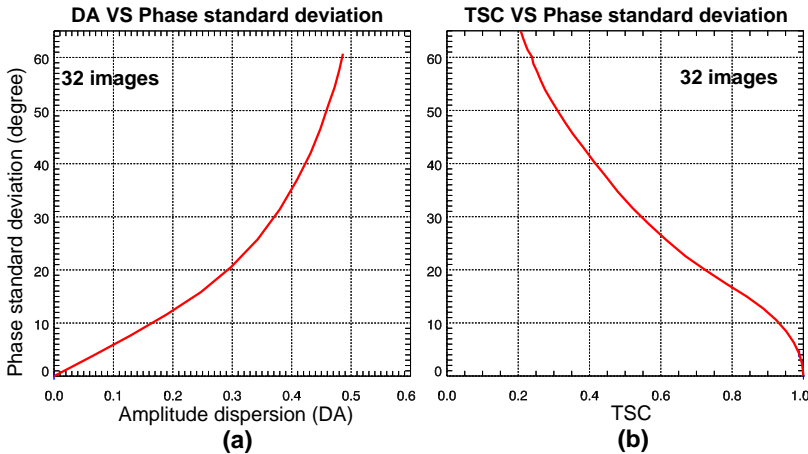


Figure 1.2: Standard deviation of the phase as a function of (a) D_A , (b) TSC for the data set of 32 SAR images.

(3) Other PS Pixel selection methods

Except the above-mentioned two PS selection algorithms, there are other approaches. For instance Hooper proposed the so-called temporal coherence for PS identification, which is calculated directly based on the estimated noisy phase component in stacks of interferograms [15, 16]. The maximum likelihood estimation approach has been also used to identify PSs subjected to a given phase Probability density function (PDF) [26, 27]. More recently, the polarimetric information has been employed for PSs identification in cases long-term PolSAR data sets are available [27–29]. Meanwhile, by setting a threshold on the highest eigenvalue of the interferometric coherence matrix [30] or on the consistency between PS clusters [31], two new PS pixel selection strategies have been developed.

1.2.1.3 Coherent Distributed scatterer pixel selection

The selection of CDS pixels is based on the coherence stability criterion. This phase quality metric is based on pixels' coherence of each interferogram. The coherence γ_{SPC} of one pixel in an interferogram can be expressed as [6]

$$\gamma_{SPC} = |\gamma_{SPC}| \cdot e^{j\psi} = \frac{E[S_1 \cdot S_2^*]}{\sqrt{E[|S_1|^2] \cdot E[|S_2|^2]}} \quad (1.2)$$

where S_1 and S_2 are the complex pixels of the two SAR images forming the interferogram, $E[\cdot]$ and $*$ stand for the expectation and conjugate operator, respectively. The modulus $|\gamma_{SPC}|$ of the complex coherence, which varies between the range $[0, 1]$, indicates the quality of the interferometric phase ψ . With 1 for fully correlated data, and 0 for totally uncorrelated data. Ideally, a large number of interferograms, which should be acquired under identical circumstances, would be needed to obtain the expectation values in (1.2). However, this is impossible as every pixel is observed only once during each SAR acquisition [32].

In practical situations, the accuracy of phase observations of a uniform region is assumed to be stationary. Under the assumption of ergodicity, the expectation operator in (1.2) is replaced by the spatial average, leading to the maximum likelihood estimator $|\hat{\gamma}_{SPC}|$

$$|\hat{\gamma}_{SPC}| = \frac{|\sum_{n=1}^N S_1^n \cdot (S_2^n)^*|}{\sqrt{\sum_{n=1}^N |S_1^n|^2 \cdot \sum_{n=1}^N |S_2^n|^2}} \quad (1.3)$$

where N indicates the number of looks, i.e. the effective number of independent pixels involved in the spatial averaging [32]. For simplicity, γ_{SPC} means the value of $|\gamma_{SPC}|$, and $\hat{\gamma}_{SPC}$ means the value of $|\hat{\gamma}_{SPC}|$ hereafter. The coherence $\hat{\gamma}_{SPC}$ can be calculated over each interferogram of all the employed interferograms by (1.3). And then the mean coherence along the stack of the included interferograms can be used as the pixel phase quality metric for pixel selection. Particularly, if an interferometric phase STD threshold is set, the threshold on the mean coherence can be determined from the relationship between coherence and phase STD [32], as Fig. 1.3 shows.

The PSI algorithms like SBAS [12, 14] and Coherent Pixel Technique (CPT) [13, 17] use coherence stability to identify CDS pixels. The coherence magnitude provides an

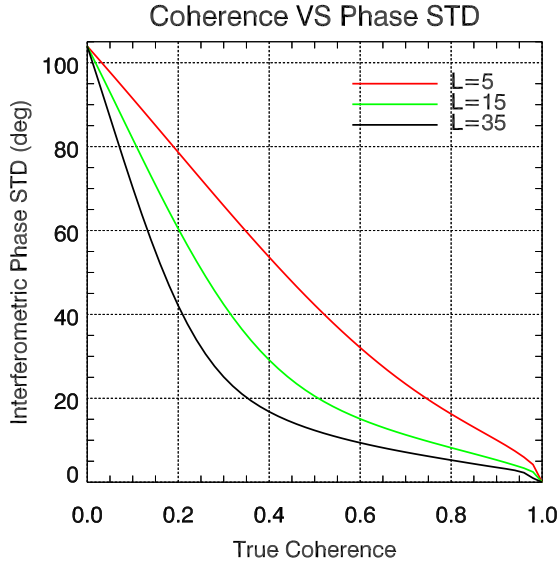


Figure 1.3: Interferometric phase standard deviation vs. coherence for different number of effective looks (different color lines).

estimation of the pixel's phase quality for each interferogram, and it is not dependent on the number of provided images. For this reason, a good estimation of the phase quality can be reached even when a reduced number of SAR data are available. In addition, a higher pixels' density can be obtained in suburban areas by using this criterion, when compared with the PS pixel selection approaches.

However, the resolution is naturally reduced as spatial averaging is employed in the coherence calculation. On the one hand, the accuracy of the estimated coherence increases as the number of the involved samples (i.e., the effective looks) grows, as Fig. 1.4 shows. On the other hand, the resolution decreases as the estimation window size increases. Thus, to ensure the robustness of the coherence criterion, the loss of the resolution is inevitable. Moreover, in heterogeneous areas, coherence estimations of central pixels that obtained through surrounding pixels could be unreliable and important details could be lost. In addition, the estimated coherence is always greater than the true one, especially for low-coherence pixels with smaller estimation window sizes the bias are more significant, as Fig. 1.4 shows. This could affect the pixel selection by this approach, as some low phase quality pixels' coherence values could be overestimated and thus be wrongly selected.

1.2.2 Polarimetric Persistent Scatterer Interferometry

PSI techniques have been traditionally applied to single-polarization data, mainly due to the shortage of long-term polarimetric SAR (PolSAR) datasets. As more satellite sen-

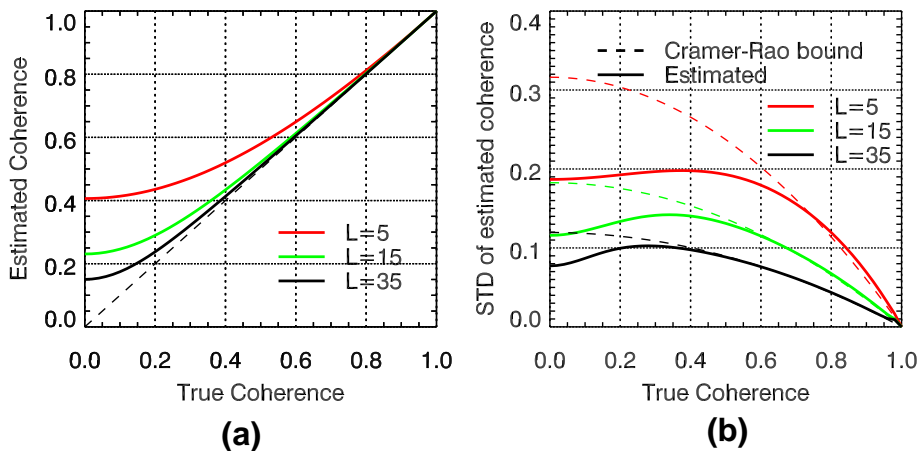


Figure 1.4: Coherence estimator validity: (a) True coherence γ_{SPC} vs estimated coherence $\hat{\gamma}_{SPC}$. (b) True coherence γ_{SPC} vs coherence estimation STD. Lines of different colors shows the cases of different effective looks.

sors with polarimetric capabilities were launched, such as RADARSAT-2, TerraSAR-X, Advanced Land Observing Satellite (ALOS-2) or Sentinel-1, the possibility of extending PSI to the polarimetric case became a reality. Therefore, the polarimetric DInSAR (PolDInSAR), or Polarimetric Permanent Scatterer Interferometry (PolPSI), was introduced [33] and developed to improve the detection and characterization of deformation phenomena by increasing the density and quality of valid pixels in comparison with the single polarization case. Starting from the so-called BEST method [33], which selects the polarimetric channel with the highest quality estimator among all available channels, PolPSI techniques have been evolved to more sophisticated methods that search the optimal polarimetric channel in a more extended space [34–44].

Conventional PolPSI techniques improve interferograms through either the optimization of an amplitude-based criterion (e.g., D_A , suitable for PSs) [34–36, 44, 45] or the maximization of the coherence stability (γ , suitable for DSs) [27, 34–36, 41–43, 46–48]. Another phase quality metric, the TSC [19, 49], has also been proposed to optimize interferograms [49], and it is effective mainly for point-like scatterers (i.e., PSs). More recently, by using the phase-based criterion temporal coherence [15], Sadeghi et al. [50] proposed a new PolPSI algorithm. This algorithm is able to retain the full spatial resolution of Single Look Complex (SLC) images, and it is more applicable than the amplitude-based PolPSI approaches in vegetated areas. Nevertheless, it works mainly for PSs and the computational cost of optimizing the temporal coherence is higher [50].

1.2.3 Permanent and Distributed Scatterers Joint Processing

As PSs and DSs are present in real scenarios more adaptive PSI algorithms have been proposed to deal simultaneously with both.

SqueeSAR [18], which is the so-called second generation of PSInSAR technique, is proposed and incorporated into the traditional PSInSAR framework to exploit both PS and DS pixels. SqueeSAR and its variants [51–54] utilize similarity tests, e.g., Kolmogorov-Smirnov (KS) [55] or Anderson-Darling (AD) [56], to search for Statistically Homogeneous Pixel (SHP)s and perform an adaptive filtering based on the SHPs found. These techniques assume that a DS pixel is usually surrounded by its SHPs. Thus, by setting a threshold on the number of identified SHPs, pixels can be classified as PS or DS pixels. PSs are processed by the original PSI method, DSs are treated as a segment with its SHPs to estimate the covariance matrix. And then based on the covariance matrix, the maximum likelihood estimation of phase history of the segment can be obtained.

Another category of adaptive PSI algorithm is CAESAR [20] and its variants [47, 57], which try to separate different scattering mechanisms within one pixel by decomposing pixels' covariance matrices using a principal component analysis. Thus, they are able to mitigate the effects of layover in urban areas for PS pixels and reduce decorrelation of DS pixels [20]. It is worth to mention that the interferometric covariance matrices for the decomposition analysis are built in an adaptive way similar with that in SqueeSAR. Particularly, for PS pixels their covariance matrices are directly obtained on pixel level while an adaptive averaging should be applied for the case of DS pixels.

For PolPSI techniques, inspired by SqueeSAR [18], Navarro-Sanchez proposed an adaptive PolDInSAR optimization method, which is based on a spatial adaptive speckle filtering approach that can jointly process DS and PS pixels [58]. As expected, this new method can achieve higher pixel densities than the conventional ones. However, as it has to carry out a similarity test to identify Polarimetric Homogeneous Pixel (PHP)s [58] for each pixel, its computation burden is high.

1.3 Motivations and objectives

As the aforementioned literature shows, there are some hot topics and open questions related with pixel optimization and selection for (Pol)PSI techniques. And the two overall research questions this thesis would like to answer are:

- *How can high quality pixels be adequately selected for single-polarimetric PSI techniques?*
- *How can polarimetric SAR data sets be utilized in a more efficient and adaptive way for PolPSI applications?*

The more detailed questions this thesis would like to cope with are:

- *How to identify high phase quality pixels from both PS and DS pixels for PSI applications?*
- *How can the interferometric phases be efficiently optimized by polarimetric optimization techniques?*
- *How can PS and DS pixels of multi-temporal PolSAR images be jointly processed to reduce the influence of decorrelation on PSI applications?*

Corresponding to the research questions above, the research objectives are summarized as follows:

- ▶ 1) Develop an inclusive phase quality metric for the identification of high phase quality pixels from both PS and DS pixels.
- ▶ 2) Study a fast and effective phase optimization method for PolPSI techniques.
- ▶ 3) Investigate an adaptive multilooking and inclusive pixel selection scheme to jointly process PS and DS pixels for PolPSI techniques.
- ▶ 4) Integrate the above-mentioned methodologies into the SUBSIDENCE-GUI software, which is the DInSAR processing chain developed by TSC-UPC based mainly on the CPT [13,17] technique.

1.4 Thesis outline

This thesis is dedicated to develop advanced pixel optimization and identification algorithms for PSI applications by using single- or multi-polarimetric SAR image stacks. Corresponding to the research objectives, it is structured as follows:

- **Chapter 2** briefly introduces some basic concepts of SAR imaging, DInSAR and PSI techniques. Meanwhile, fundamentals of PolPSI have also been given to ease the comprehension of the following chapters related.
- In **Chapter 3**, the main results of this thesis, which are also the most significant results related to the four articles construct this thesis, are presented and discussed.
- **Chapter 4** summarizes the main contributions and conclusions of this thesis, and some possible future research outlines related with this thesis are given.

- **Chapter 5** lists the four articles generated during the development of this thesis.

2

CHAPTER 2

THEORETICAL BASIS

2.1 SAR Imaging

A SAR system consists of an active microwave sensor mounted in a moving platform (space-born, air-born or ground-based). This microwave sensor, i.e., the radar, transmits electromagnetic pulses with a certain Pulse Repetition Frequency (PRF) towards the observed scene and simultaneously receives the reflected echoes that contain the scene information. These echoes associated with the observing area are usually stored in a $2D$ matrix called *raw-data*. Fig. 2.1 shows the acquisition geometry of the SAR system. When it is working, the platform moves along the *azimuth* direction while the sensor transmits electromagnetic pulses towards the *range* direction. The acquired SAR image is a projection of the observing targets on the Earth surface, known as the *ground-range* plane, into the radar acquisition plane, i.e., *slant-range* plane. The *incidence angle* θ is defined as the angle between the range direction and the normal direction of the *ground-range* plane as Fig. 2.1 shows.

The range resolution Δr of a SAR image can be expressed as

$$\Delta r = \frac{c\tau}{2} \approx \frac{c}{2B_w} \quad (2.1)$$

where τ is the time duration of the radar transmitted electromagnetic pulses, c the speed of light, 2 accounts for the round trip delay and B_w refers the pulse bandwidth. As (2.1) shows, reducing the pulse transmission duration τ or increasing B_w can improve the range resolution Δr . However, in order to maintain a required SNR the pulse time

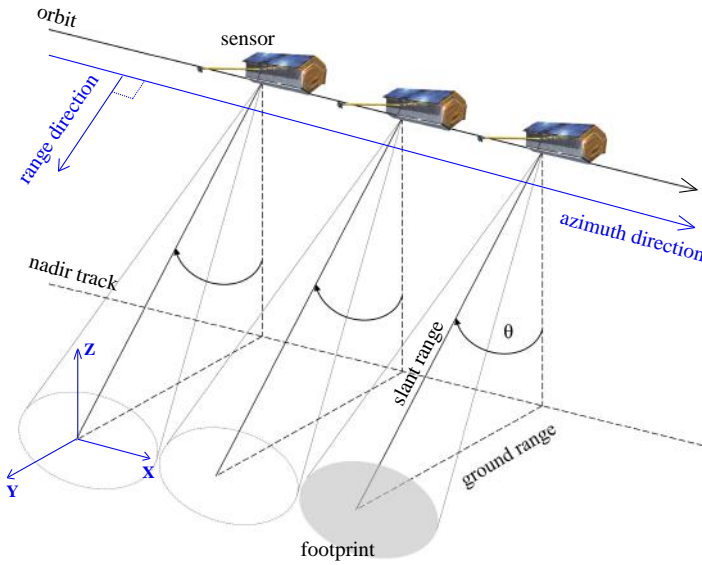


Figure 2.1: SAR acquisition geometry.

should be kept long enough to guarantee a reasonable level of transmitted power. To solve this dilemma, the pulse compression technique is typically used. This technique is based on transmitting a long modulated pulse and processing it afterwards by a matched filter. The most popular waveform used in range compression of SAR systems is named as *chirp* [59], which is a linear frequency-modulated pulse. The bandwidth B_w of the chirp signal directly depends on the duration of the pulse and the chirp rate α , which can be expressed as

$$B_w = \alpha\tau. \quad (2.2)$$

By introducing the *chirp* signal, the new range resolution can be derived as (2.3) according to (2.1) and (2.2)

$$\Delta r = \frac{c}{2B_w} \approx \frac{c}{2\alpha\tau}. \quad (2.3)$$

At this point, according to (2.3), the range resolution of SAR image can be improved thanks to this pulse compression technique.

For a Real Aperture Radar (RAR), its azimuth resolution Δx is limited by the used antenna's beamwidth as follows

$$\Delta x \approx r \frac{\lambda}{L} \quad (2.4)$$

where r is the slant-range distance (i.e., target-to-sensor distance), L the effective antenna dimension in the azimuth direction, and λ the wavelength. As indicated by (2.4), to achieve high azimuth resolution an extremely large antennas would be required, which is technically impossible. To overcome this limitation, the synthetic aperture concept was invented, which is demonstrated by Fig. 2.2. When a SAR system is working, a certain target P in the scene is being observed by the sensor during a period t_{obs} that

depends both on the antenna beamwidth and the velocity of the platform, as Fig. 2.2 shows. Within this observing period several pulse echoes are acquired by the antenna every $\Delta t = \frac{1}{PRF}$, and then by coherently combining all these acquired echoes, a larger equivalent antenna can be synthesized. The length of this synthesized antenna is

$$L_{SA} = v_s t_{obs} = \frac{2r\lambda}{L} \quad (2.5)$$

where v_s refers to the platform moving velocity along the orbit. Introducing (2.5) into (2.4), the new azimuth resolution can be expressed as

$$\Delta x \approx \frac{L}{2}. \quad (2.6)$$

Notice how now the azimuth resolution of SAR image has been improved to the level of the physical length of the real antenna. Moreover, it does not depend on the very long sensor-to-target distance any more, and it is constant along the swath.

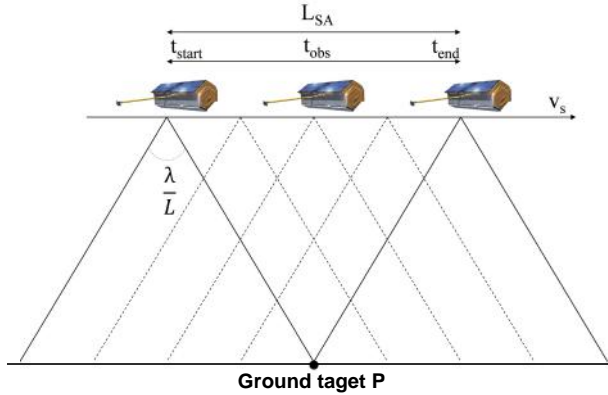


Figure 2.2: Synthetic aperture radar concept.

The data obtained through the above procedure is the raw image in the range-azimuth domain. It has to be processed in both azimuth and range directions to concentrate each target's information distributed along these two directions. This processing is the so-called focusing, and there are several focusing algorithms [60–62].

After focusing processing of SAR raw images, the complex SAR images called Single Look Complex (SLC) images have been obtained. SLC images contain amplitude and phase information of the observed scene. For PSI applications, the most useful information contained in SLC is the phase φ , and for a single target it can be expressed as

$$\varphi = -\frac{4\pi}{\lambda}(r) + \varphi_{scatterer} + \varphi_{atm} + \varphi_{noise} \quad (2.7)$$

where r is the sensor-to-target distance, and $\varphi_{scatterer}$ is the intrinsic phase that relates to the target's electric properties, φ_{atm} is the extra delay caused by the propagation through atmospheric layers, and φ_{noise} the SAR system thermal noise.

Because of the side-looking geometry of space-born SAR systems, three main geometric distortions may occur in space-born SAR images, as Fig. 2.3 shows.

- **Foreshortening.** For slopes oriented toward the SAR system, they are compressed in SLC images after the slant-range projection, for instance, from $A - B$ to $A' - B'$ in Fig. 2.3(a).
- **Layover.** When the angle of a slope facing to the radar ($A - B$ in Fig. 2.3(b)) exceeds the radar incidence angle, scatterers on this slope are imaged in a reverse order. In other words, targets at higher elevations appear earlier in SAR image and they could superimpose on the contribution from the other areas, $A - B$ to $B' - A'$ in Fig. 2.3(b).
- **Shadowing.** When a slope away from the radar illumination is steeper than the incidence angle, there are some parts (e.g., $C - D$ in Fig. 2.3(c)) that are not illuminated by the radar. As a consequence, no useful information of this area can be collected and very low amplitudes will appear in SLC, $C - D$ to $C' - D'$ in Fig. 2.3(c).

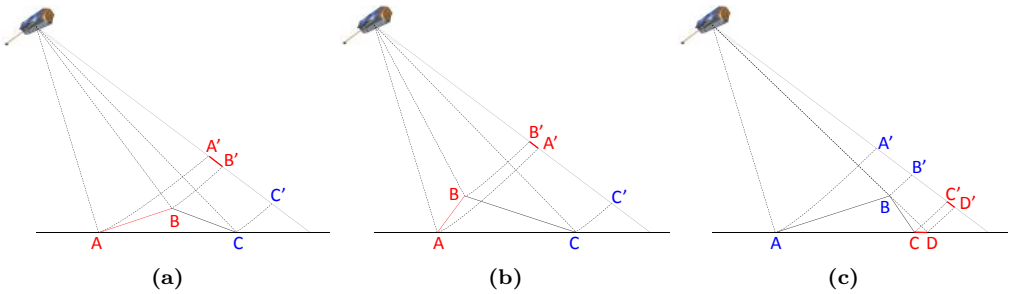


Figure 2.3: SAR image geometrical acquisition distortions: (a) foreshortening, (b) layover, and (c) shadowing.

2.2 SAR Interferometry

Once two SLC images (*master* image \mathbf{S}_1 and *slave* image \mathbf{S}_2) corresponding to the same area are co-registered, the interferogram \mathbf{I} is defined as the complex product of this pair of SLC images

$$\mathbf{I} = \mathbf{S}_1 \mathbf{S}_2^* \quad (2.8)$$

and the related interferometric phase of a target in the scene can be derived as (2.9) by referring to (2.7)

$$\phi = \varphi_1 - \varphi_2 = -\frac{4\pi}{\lambda}(r_1 - r_2) + (\varphi_{scatterer_1} - \varphi_{scatterer_2}) + (\varphi_{atm_1} - \varphi_{atm_2}) + (\varphi_{noise_1} - \varphi_{noise_2}) \quad (2.9)$$

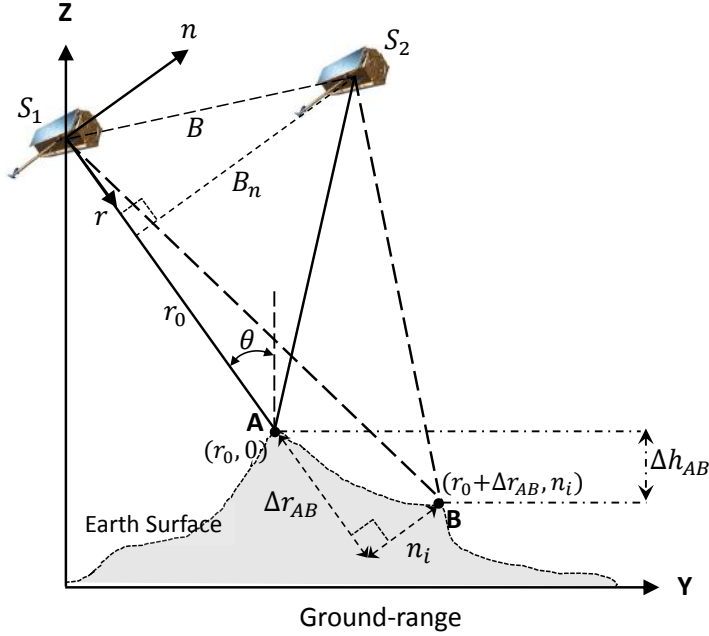


Figure 2.4: Interferogram acquisition geometry.

where φ_1 and φ_2 are the targets' phases of the master and slave images, respectively. Under the assumption that the target characteristics do not change that much from one image to the other, i.e. $\varphi_{scatterer_1} \approx \varphi_{scatterer_2}$, (2.9) turns to

$$\phi = -\frac{4\pi}{\lambda}(r_1 - r_2) + \phi_{atm} + \phi_{noise} \quad (2.10)$$

where $\phi_{atm} = \varphi_{atm_1} - \varphi_{atm_2}$ accounts for the difference between the two atmospheric phase terms of these two acquisitions, and $\phi_{noise} = \varphi_{noise_1} - \varphi_{noise_2}$.

For space-born SAR systems, the two SLC images are acquired at slightly different positions separated by a distance known as baseline B , as Fig. 2.4 shows. For two given generic targets A and B, as Fig.2.4 shows, the related interferometric phase increment $\Delta\phi_{AB}$ between these two targets can be expressed as a function of their slant-range distances difference Δr_{AB} , the reference distance r_0 , the radar incidence angle θ , the height difference between the two points Δh_{AB} and the perpendicular baseline B_n . The latter is the projection of the baseline into the perpendicular direction of the incidence angle, as it shows in Fig. 2.4.

Particularly, the increment of the interferometric phase $\Delta\phi_{AB}$ can be expressed as

$$\Delta\phi_{AB} = \Delta\phi_{flat} + \Delta\phi_{topo} + \Delta\phi_{atm} + \Delta\phi_{noise} \quad (2.11)$$

where

- $\Delta\phi_{flat}$ is the flat earth phase contribution, which accounts for a phase trend generated by an ideally flat earth. This phase term appears as a phase ramp that depends on the perpendicular baseline B_n , and it grows from the near-range (minimum distance) to the far-range (maximum distance).

$$\Delta\phi_{flat} = \frac{4\pi}{\lambda} \frac{B_n}{r_0 \tan(\theta)} \Delta r_{AB} \quad (2.12)$$

- $\Delta\phi_{topo}$ is the topographic phase term induced by the height variation Δh , and it contains the topographic information of the scene. The larger the spatial separation (perpendicular baseline B_n) between acquisitions, the higher the topographic phase variation, as (2.13) shows.

$$\Delta\phi_{topo} = \frac{4\pi}{\lambda} \frac{B_n}{r_0 \sin(\theta)} \Delta h_{AB} \quad (2.13)$$

- $\Delta\phi_{atm}$ accounts for changes in the atmospheric conditions between the two different temporal acquisitions.
- $\Delta\phi_{noise}$ is the noise phase term introduced by all the decorrelation factors that degrade interferometric phase quality.

A Digital Elevation Model (DEM) can be generated by the exploitation of the topographic phase term $\Delta\phi_{topo}$, which was the first application of SAR interferometry. Particularly, by removing the flat earth term and neglecting (or canceling) atmospheric and noise phase ones in (2.11), only $\Delta\phi_{topo}$ left. And then, because of the cyclical nature of the interferometric phase, an unwrapping process has to be applied to $\Delta\phi_{topo}$ [63–65]. In the next, the unwrapped phase can be converted into heights through the inversion of (2.13) and this floating solution can be fixed by one or more tie points with known heights.

2.3 Differential SAR Interferometry

The Differential interferometry SAR (DInSAR) technique quantifies ground deformation by exploiting interferometric phase difference. The differential interferometric phase equation, which accounts for the possible terrain deformation undergo between the two SAR acquisitions, can be expressed as

$$\phi = \phi_{flat} + \phi_{topo} + \phi_{def} + \phi_{atm} + \phi_{noise} \quad (2.14)$$

with

$$\phi_{flat} = \frac{4\pi}{\lambda} \frac{B_n}{r_0 \tan(\theta)} \Delta r, \quad \phi_{topo} = \frac{4\pi}{\lambda} \frac{B_n}{r_0 \sin(\theta)} \Delta h, \quad \phi_{def} = \frac{4\pi}{\lambda} \rho \quad (2.15)$$

where Δr is the target-to-radar distance difference between the two acquisitions (caused by the perpendicular baseline), Δh represents the target's height (w.r.t. the flat earth plane), and ρ in ϕ_{def} is the deformation to be estimated.

The deformation phase term is the objective of DInSAR techniques and thus the other interferometric phase should be canceled. Based on an external DEM and orbital information, the topographic term ϕ_{topo} and flat earth phase term ϕ_{flat} can be canceled. Once these two phase terms have been canceled from (2.14), the remain residual phase can be exploited for deformation extraction. However, two important aspects must be taken into account when retrieving displacement by DInSAR techniques:

- There could be undesirable phase fringes caused by the changes of atmospheric artifacts between the two SAR acquisitions (i.e., ϕ_{atm}). These atmospheric fringes, in some cases, are hard to be canceled from differential interferograms as they may be similar with the ones generated by deformation.
- The differential phase can be wrapped for case of abrupt terrain displacement, which could be solved by employing unwrapping techniques or relating close targets to avoid phase cycles.

2.4 Persistent Scatterer Interferometry

The classic DInSAR technique is effective for large and abrupt deformation, such as those caused by earthquakes or volcanic eruptions. However, it is difficult to apply it in monitoring low velocity deformations where differential interferograms with large temporal baselines should be used. In this case, temporal decorrelation can degrade interferometric phases, making the extraction of useful information almost impossible, unless large coherent areas are present. Moreover, the presence of atmospheric artifacts and geometrical decorrelation can also undermine qualities of interferometric phases, consequently, reducing deformation estimation accuracy. To overcome these limitations, various techniques have been proposed during the last two decades to investigate the temporal evolution of deformations from large image datasets. These techniques are known as the advanced DInSAR, the Multi-Temporal InSAR (MTInSAR) or the Persistent Scatterer Interferometry (PSI) [10–20].

The work in this thesis is developed based on the Coherent Pixels Technique (CPT) [13,17], which is the PSI algorithm proposed by CommSensLab of the Signal Theory and Communications department of the Universitat Politècnica de Catalunya (UPC). It has now been implemented in the SUBSIDENCE-GUI processor. CPT has been successfully applied to different scenarios for ground deformation monitoring [66–72], and it consists of mainly four blocks: *Interferogram selection and generation*, *Pixel optimization and selection*, *Linear deformation estimation*, *Non-linear deformation estimation*.

The interferogram selection block determines the approach of interferogram generation (e.g., the single-master or multi-master approach), and both spatial and temporal maximum baseline lengths allowed for interferograms. Details about this block can be found in [73]. The second block, i.e. the pixel optimization and selection block, is employed

to optimize pixels' interferometric phases and identify those high phase quality pixels along the observing period. This thesis is focused on this block, and its state-of-art has been described in detail in **Chapter 1**. The other two blocks that aimed respectively at linear and non-linear deformation estimation will be briefly introduced in this section. More details of CPT and the SUBSIDENCE-GUI processor can be found by referring to [73], [74].

2.4.1 Linear Deformation Estimation Block (LDEB)

Starting from the differential interferograms and a map of selected Persistent Scatterer Candidate (PSC)s, the Linear Deformation Estimation Block (LDEB) estimates the linear deformation velocity v and the residual topographic error ε , which is due to inaccuracies of the DEM employed for the generation of differential interferograms. This is accomplished by adjusting a linear model of v and ε to the data (i.e., the phases of differential interferograms). This linear model, on interferogram level, of one pixel can be expressed as

$$\phi_{model} = \frac{4\pi}{\lambda} \cdot T \cdot v + \frac{4\pi}{\lambda} \cdot \frac{B_n}{r \cdot \sin(\theta)} \cdot \varepsilon \quad (2.16)$$

where λ is the wavelength, T and B_n are respectively the temporal and perpendicular baselines of the interferogram, r the sensor-to-target distance, θ the local incidence angle.

The LDEB can be divided into three sub-blocks, i.e., *Triangulation*, *Minimization* and *Integration*, as Fig. 2.5 shows:

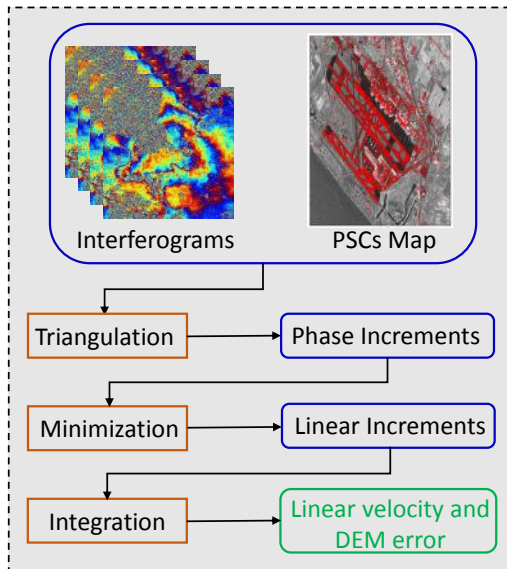


Figure 2.5: Diagram for the estimation of the linear components of CPT.

1) Triangulation

Due to different phase offsets among differential interferograms, it is very difficult to derive v and ε through (2.16) by using phases of individual pixels, directly. On the other hand, the differential interferometric phases are wrapped and may contain atmospheric artifacts, which can affect the adjustment of (2.16). These problems are overcome by relating neighboring PSCs by the means of Delaunay triangulation, where the PSCs are nodes and links between nodes are arcs. Then phase increments along arcs are calculated on the interferogram level, and the phase increment along $arc_{m,n}$ of the i -th differential interferogram can be expressed as

$$\Delta\phi^i(T_i, B_{n,i}, x_m, y_m, x_n, y_n) = \Delta\phi^i(T_i, B_{n,i}, arc_{m,n}) = \phi^i(x_m, y_m) - \phi^i(x_n, y_n) \quad (2.17)$$

where the (x_m, y_m) and (x_n, y_n) are locations of the two nodes (i.e., the two selected pixels) forming this arc. In this way, CPT is able to work with interferometric phase increments rather than absolute phases. On the other side, for the i -th differential interferogram, the linear model along $arc_{m,n}$ can be derived as (2.18) according to (2.16)

$$\Delta\phi_{model}^i(T_i, B_{n,i}, arc_{m,n}) = \frac{4\pi}{\lambda} \cdot T_i \cdot \Delta v(arc_{m,n}) + \frac{4\pi}{\lambda} \cdot \frac{B_{n,i}}{r_i \cdot \sin(\theta_i)} \cdot \Delta\varepsilon(arc_{m,n}) \quad (2.18)$$

where $\Delta v(arc_{m,n})$ and $\Delta\varepsilon(arc_{m,n})$ are respectively the linear velocity and DEM error increment along $arc_{m,n}$ [73, 74].

2) Minimization

As $\Delta v(arc_{m,n})$ and $\Delta\varepsilon(arc_{m,n})$ are constants for all the interferograms, they can be estimated by adjusting $\Delta\phi_{model}^i$ to the data $\Delta\phi^i$. This is achieved through the minimization of a designed cost function $\Gamma(arc_{m,n})$ as

$$\Gamma(arc_{m,n}) = \frac{1}{N_{int}} \cdot \sum_{i=1}^{N_{int}} \left| e^{-j\Delta\phi^i(T_i, B_{n,i}, arc_{m,n})} - e^{-j\Delta\phi_{model}^i(T_i, B_{n,i}, arc_{m,n})} \right|^2 \quad (2.19)$$

where N_{int} is the number of interferograms. This minimization is done in the complex plane, thus, any kind of phase unwrapping on interferograms is not required at this step. By doing this minimization from one arc to the other, increments of linear velocity and DEM error of all arcs in the network can be obtained. Meanwhile, the model quality (or model coherence) of each arc is calculated to assess the quality of its related solution (i.e., Δv and $\Delta\varepsilon$). After this, to ensure final products' reliabilities of LDEB, bad quality arcs are eliminated by discarding those with model coherence values below a threshold [73, 74].

3) Integration

From the arc increments obtained in the previous step, the linear displacement and DEM error for each selected pixel are derived through an integration process. And then this float solution can be fixed by using one or multiple pixels with known DEM errors and linear velocities as tie points. The flow-chart of LDEB is depicted in Fig. 2.5.

2.4.2 Non-linear Deformation Estimation Block (NLDEB)

The LDEB obtains linear component of the displacement, to retrieve a complete estimation, the non-linear deformation has to be retrieved. This is completed by Non-linear Deformation Estimation Block (NLDEB) of CPT, and it consists of two parts, i.e., *atmospheric artifacts estimation* and *temporal non-linear displacement estimation*, as Fig. 2.6 shows.

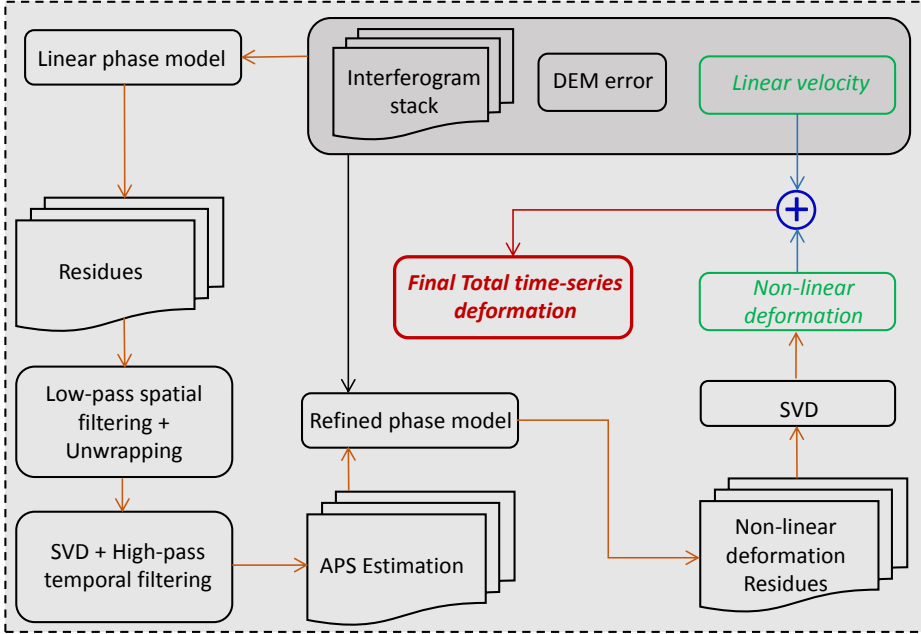


Figure 2.6: Diagram for the estimation of the non-linear displacement of CPT.

1) atmospheric artifacts estimation

The residual interferometric phase ϕ_{res} for each interferogram can be obtained by subtracting the linear components obtained by LDEB from the differential interferometric phase ϕ as

$$\phi_{res} = \phi - \phi_{model} \quad (2.20)$$

where ϕ_{model} is the linear model phase that can be obtained according to (2.16). Then based on ϕ_{res} , the atmospheric phase can be isolated by taking advantage of its different spatio-temporal frequency properties with that of the non-linear deformation component. Particularly, the atmospheric phase can be considered as a spatial low-pass signal in each interferogram (or image) and a white noise process in time. On the other hand, the non-linear deformation presents a narrower spatial correlation window compared with Atmospheric Phase Screen (APS) and presents a low-pass behavior in time. It is worth to note that due to the white noise process of atmospheric artifacts, their frequencies fill the whole temporal spectra and, thus, partially overlap with that of non-linear deformation.

Firstly, a low-pass spatial filtering is applied to the interferometric residue of each interferogram and the filtered residue should become

$$\phi_{res,SLR} = \phi_{non-linear,SLR} + \phi_{atm} \quad (2.21)$$

where $\phi_{non-linear,SLR}$ is the Spatial Low Resolution (SLR) non-linear component of the displacement, and ϕ_{atm} the APS as it is assumed to be low-pass in spatial domain and not affected by the spatial filter.

After the spatial low-pass filter, an offset for each $\phi_{res,SLR}$ can be estimated through an histogram analysis. And this new set of residual interferometric phases are easy to unwrap since they should be very smooth in spatial as almost all fringes have been removed. Once unwrapped the phase and removed an offset for each one of the residual interferograms, the Singular Value Decomposition (SVD) is applied to transform the phase from differential time domain to the image time one.

After the above inversion, the result is integrated with respect to the first image. And then a high-pass temporal filter is employed to extract the image level APS term. Until now, the atmospheric phase ϕ_{APS} for any interferogram can be calculated. It is worth to note that the high-pass cut frequency for the temporal filter should be set as the highest possible frequency of the non-linear displacement.

2) temporal non-linear displacement estimation

Once the APS has been estimated, a new residual interferometric phase free of atmospheric artifacts can be calculated as

$$\phi_{res,APSfree} = \phi - \phi_{model} - \phi_{APS} - \phi_{off} = \phi_{non-linear} + \phi_{noise} \quad (2.22)$$

where ϕ_{APS} and ϕ_{off} are the APS and phase offset estimated in the previous step, $\phi_{non-linear}$ the non-linear deformation component, and ϕ_{noise} the interferometric phase noise term. Then by employing a new SVD process on $\phi_{res,APSfree}$ of all the interferograms, the temporal phase profile corresponding with non-linear deformation can be retrieved and converted to displacement. Finally, the total deformation is obtained by adding the linear and non-linear terms together, as it is shown in Fig. 2.6.

2.5 Polarimetric Persistent Scatterers Interferometry (PolPSI)

2.5.1 Polarimetric SAR interferometry (PolInSAR)

Polarimetric SAR interferometry (PolInSAR) is based on two polarimetric SAR images acquired from two spatially separated locations [40, 75]. In monostatic systems the assumption of reciprocity can be applied and for quad-pol SAR data sets the PolSAR

scattering vector \mathbf{k} under Pauli basis can be obtained with

$$\mathbf{k} = \frac{1}{\sqrt{2}}[S_{hh} + S_{vv}, S_{hh} - S_{vv}, 2S_{hv}]^T \quad (2.23)$$

where T means the transpose, S_{hh} and S_{vv} stand for the horizontal and vertical co-polar channels, respectively, and S_{hv} , equal to S_{vh} in the monostatic case, is the cross-polar channel of the scattering matrix [76]. If the data is dual-pol, (2.23) is replaced by (2.24) if only the co-polar channels are available,

$$\mathbf{k} = \frac{1}{\sqrt{2}}[S_{hh} + S_{vv}, S_{hh} - S_{vv}]^T \quad (2.24)$$

or by (2.25) if a co-polar xx and the cross-polar channels are available,

$$\mathbf{k} = [S_{xx}, 2S_{hv}]^T. \quad (2.25)$$

Then the PolInSAR vector can be defined as

$$\mathbf{K} = [\mathbf{k}_1, \mathbf{k}_2]^T \quad (2.26)$$

where \mathbf{k}_1 and \mathbf{k}_2 are the two scattering vectors from the master and slave PolSAR images that form the interferogram. To generate a single interferogram based on \mathbf{K} , two normalized complex projection vectors $\boldsymbol{\omega}_1$ and $\boldsymbol{\omega}_2$ are introduced [75, 76]. These two vectors can be interpreted as two scattering mechanisms (SMs), and the two PolInSAR vectors \mathbf{k}_1 and \mathbf{k}_2 can be projected onto them, respectively

$$\mu_i = \boldsymbol{\omega}_i^\dagger \cdot \mathbf{k}_i, \quad i = 1, 2 \quad (2.27)$$

where \dagger refers to the conjugate transpose, μ_1 and μ_2 are the two scattering coefficients, analogous to single-polarization SAR images [75], [76]. To avoid introducing artificial changes in the phase centers of the scatterers in PolPSI applications, $\boldsymbol{\omega}_1$ and $\boldsymbol{\omega}_2$ are forced to be identical to one optimal projection vector $\boldsymbol{\omega}$ for all the interferograms [35, 36, 75].

The rationale of polarimetric optimization techniques, i.e. PolPSI techniques, is to enhance the phase quality of the interferograms by combining adequately the different polarization channels available to produce an improved one according to a figure of merit. And as it will be introduced in the following two subsections, there are two common phase quality metrics used for the polarimetric optimization in PolPSI techniques. One is D_A , which is better for the optimization of PS pixels, and the other is coherence stability better for DS pixels' optimization.

2.5.2 Polarimetric Optimization for Deterministic Scatterers (PSs)

For deterministic scatterers, \mathbf{k}_i in (2.27) corresponds to a deterministic vector [36, 58, 76]. The expression for vector interferogram can be obtained as [75]

$$Intf = \mu_1 \cdot \mu_2^* \quad (2.28)$$

where $*$ is the complex conjugate. The commonly used pixel phase quality criterion for PSs is the amplitude dispersion D_A , which can be expressed as [34, 36]

$$D_A = \frac{\sigma_A}{m_A} = \frac{1}{|\overline{\omega^\dagger \mathbf{k}}|} \sqrt{\frac{1}{N} \sum_{i=1}^N \left(|\omega^\dagger \mathbf{k}_i| - |\overline{\omega^\dagger \mathbf{k}}| \right)^2} \quad (2.29)$$

with

$$|\overline{\omega^\dagger \mathbf{k}}| = \frac{1}{N} \sum_{i=1}^N |\omega^\dagger \mathbf{k}_i| \quad (2.30)$$

where σ_A and m_A are the standard deviation and mean of the images' amplitudes, N is the number of images and the over line indicates the empirical mean value [34, 36].

2.5.3 Polarimetric Optimization for Distributed Scatterers (DSs)

For distributed scatterers, (2.26) behaves as a random vector due to the complex stochastic scattering process within one resolution cell [36, 58]. In this case, the 6×6 (for full-pol data) or 4×4 (for dual-pol data) PolInSAR coherency matrix \mathbf{T}_6 or \mathbf{T}_4 are defined as (2.31) to characterize the scatterers' behaviors

$$\mathbf{T}_6 \setminus \mathbf{T}_4 = E\{\mathbf{k}\mathbf{k}^\dagger\} = \begin{bmatrix} \mathbf{T}_{11} & \boldsymbol{\Omega}_{12} \\ \boldsymbol{\Omega}_{12}^\dagger & \mathbf{T}_{22} \end{bmatrix} \quad (2.31)$$

where E is the expectation operator, which is usually implemented with a spatial neighboring average [75, 76]. \mathbf{T}_{11} and \mathbf{T}_{22} are the individual coherency matrices and $\boldsymbol{\Omega}_{12}$ is the PolInSAR coherency matrix given by [75]

$$\mathbf{T}_{11} = E\{\mathbf{k}_1\mathbf{k}_1^\dagger\} \quad \mathbf{T}_{22} = E\{\mathbf{k}_2\mathbf{k}_2^\dagger\} \quad \boldsymbol{\Omega}_{12} = E\{\mathbf{k}_1\mathbf{k}_2^\dagger\}. \quad (2.32)$$

Then the vector interferogram can be obtained with

$$\begin{aligned} Intf &= E\{\mu_1 \cdot \mu_2^*\} = E\{(\omega^\dagger \mathbf{k}_1)(\omega^\dagger \mathbf{k}_2)^\dagger\} \\ &= \omega^\dagger E\{\mathbf{k}_1\mathbf{k}_2^\dagger\} \omega = \omega^\dagger \boldsymbol{\Omega}_{12} \omega \end{aligned} \quad (2.33)$$

from which the interferometric phase can be derived as $arg(\omega^\dagger \boldsymbol{\Omega}_{12} \omega)$. The corresponding coherence $\gamma(\omega)$ is then given by [75, 76]

$$\gamma(\omega) = \frac{|\omega^\dagger \boldsymbol{\Omega}_{12} \omega|}{\sqrt{\omega^\dagger \mathbf{T}_{11} \omega} \sqrt{\omega^\dagger \mathbf{T}_{22} \omega}}. \quad (2.34)$$

For PolPSI applications, the mean coherence $\bar{\gamma}$ expressed by (2.35) is used as the interferometric phase quality estimation [34, 36, 58]

$$\bar{\gamma} = \frac{1}{N_{intf}} \sum_{k=1}^{N_{intf}} \gamma(\omega)_k \quad (2.35)$$

where N_{intf} is the number of interferograms.

It can be seen from (2.29) and (2.35) that the two phase quality estimators D_A and $\bar{\gamma}$ are both influenced by the projection vector ω . Therefore, phase optimization in PolPSI consists in searching for the optimal projection vector ω that minimizes D_A or maximizes $\bar{\gamma}$. The simple BEST method simply selects the polarization channel with the highest estimated phase quality. The ESM approach explores the full space of solutions while SOM just a subspace, both at the price of a high computational burden. The detailed implementation of the three methods can be found in [36].

It has to be noted that in PolPSI applications the same projection vector ω has to be used for all images. If not, the choice of different projection vectors for each image of the interferograms may lead to undesired changes in the phase centers of the scatterers [36]. So, it has to be ensured for any pixel that $\omega_1 = \omega_2 = \omega$ for all images of the data set.

3

CHAPTER 3 RESULTS

The objectives of this thesis are addressed in four peer-reviewed journal articles. This chapter briefly presents the core idea and main results of the four articles, and the full contents of these four journal articles can be found in **Chapter 5**.

3.1 A Temporal Phase Coherence Estimation Algorithm for the Selection of Persistent Scatterers

This section is based on: Feng Zhao and Jordi Mallorqui, *A Temporal Phase Coherence Estimation Algorithm and Its Application on DInSAR Pixel Selection*, IEEE Transactions on Geoscience and Remote Sensing, 2019 [77] (See **Section 5.1**).

3.1.1 Introduction

Pixel selection is a crucial step of all advanced DInSAR techniques that has a direct impact in the quality of the final PSI products. The conventional D_A or coherence stability approach has shortcomings as discussed in **Chapter 1**. To overcome these shortcomings, in [77] (i.e., **Section 5.1**), we propose a full-resolution phase quality estimation and pixel selection approach for PSI processing. The proposed algorithm is similar to the conventional coherence method, but it estimates the phase coherence temporally. Since

the conventional coherence is estimated based on the spatial neighboring pixels and the new coherence is obtained in the temporal dimension, we refer the classical coherence as spatial coherence (SPC) and the new coherence as Temporal Phase Coherence (TPC). As the coherence is now evaluated temporally at pixel level, the method is able to work on both PS and DS pixels. The idea of TPC is similar with that was proposed by Hooper [15], but a different approach has been used to estimate it. Also, the influence of different interferograms' combinations on the estimation of TPC and its relationship with the interferometric phase standard deviation (phase STD), which had not been sufficiently discussed in Hooper's paper [15], [16], have been deeply investigated in [77] (i.e., **Section 5.1**).

3.1.2 Main Results

Together with the classical coherence and amplitude dispersion methods, the TPC pixel selection algorithm has been tested on 37 VV polarization Radarsat-2 images of Barcelona Airport. The derived deformation maps by employing the three pixel selection methods are shown in Fig. 3.1 (i.e., Fig. 11 in [77]), where very similar subsidence trends are detected by all the three approaches. The derived subsidence patterns and deformation values are in good accordance with previous studies [35, 36, 58], which further validates the reliability of the results. The subsidence mainly occurred over the airport access road and Terminal T1 areas, and the maximum subsidence velocity reaches up to 2.5 cm/year.

As Fig. 3.1 illustrates, the TPC approach has much better performance in pixels' density than the other two methods. Particularly, the TPC method is able to select 22,744 pixels, which accounts for about 318% and 146% of that obtained by D_A (7,150 pixels) and SPC (15,547 pixels) approaches. For the SPC case it has to be pointed out that as a moving averaging window has been used the pixels are not at full resolution. Due to the obvious improvement on pixels' density, TPC can detect at full resolution more detailed subsidence patterns than the other two. Besides obvious improvements on the number of selected pixels, the new method shows some other advantages comparing with the other classical two [77]. The proposed pixel selection algorithm, which presents an affordable computational cost, is easy to be implemented and incorporated into any advanced DInSAR processing chain for high quality pixels' identification.

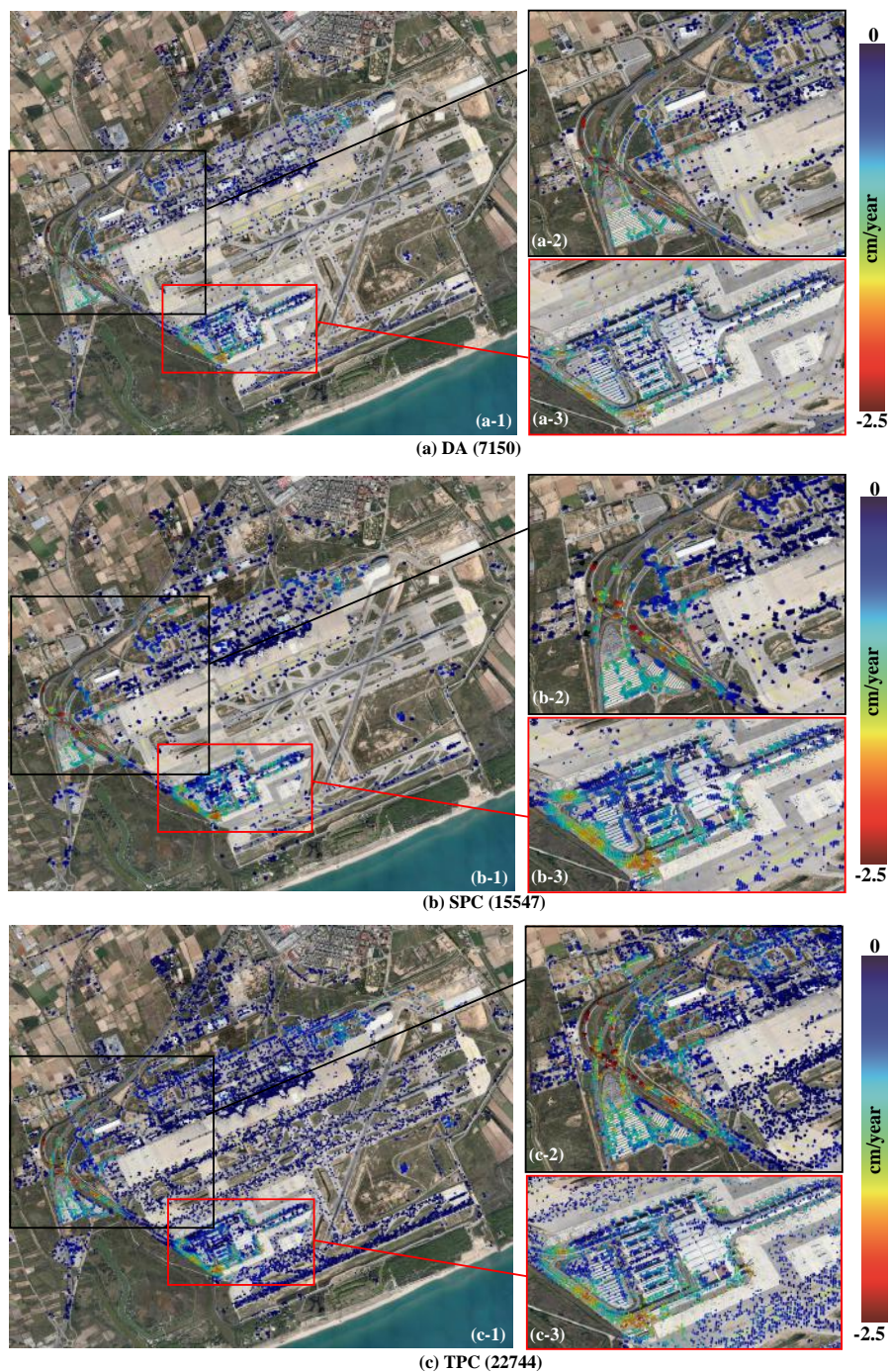


Figure 3.1: Deformation velocity map in Barcelona "El Prat" Airport retrieved by (a) the PS (D_A) approach, (b) the classical spatial coherence (SPC) approach, and (c) the proposed temporal phase coherence (TPC) approach. The number in the bracket represents the amount of selected pixels by each approach.

3.2 Landslide Monitoring Using PSI With Advanced Persistent Scatterers Selection Methods

This section is based on: Feng Zhao, Jordi Mallorqui, Rubén Iglesias, Josep Gili, and Jordi Corominas, *Landslide monitoring using multi-temporal SAR interferometry with advanced persistent scatterers identification methods and super high-spatial resolution TerraSAR-X images*, Remote Sensing, 2018, 10(6), 921 [78] (See **Section 5.2**).

3.2.1 Introduction

The TPC pixel selection approach has been proposed and tested in a small area with the C-band Radarsat-2 data set in [77] (i.e., **Section 5.1**). However, its validity and advantages have not been demonstrated by other SAR data set of different band over different scenario. On the other hand, landslides are usually located in mountainous areas and the area of interest can be partially or even heavily vegetated. The inherent temporal decorrelation that dramatically reduces the number of Coherent Scatterers (Coherent Scatterer (CS)s) of the scene limits in practice the application of PSI technique for landslide monitoring. It is thus crucial to be able to detect as much CSs as possible that can be usually embedded in decorrelated areas. High resolution imagery combined with efficient pixel selection methods can make possible the application of DInSAR techniques in landslide monitoring. Therefore, in [78] (**Section 5.2**), the TPC approach with the other two full-resolution PS identification algorithms are employed together with 32 super high-spatial resolution (Super High-spatial Resolution (SHR)) TerraSAR-X (TSX) images, staring-spotlight mode, to monitor the Canillo landslide (Andorra) [See Fig. 1 in **Section 5.2**]. The performance of TPC is assessed by comparing with the other two pixel selection methods in this challenging area with a X-band SAR data set.

3.2.2 Main Results

3.2.2.1 Line-of-Sight (LOS) Monitoring Results

The Line of Sight (LOS) displacement rate maps derived by the three full-resolution pixel selection methods (i.e., the D_A , TSC and TPC) are shown in Fig. 3.2(a-c) (i.e., Fig. 8(a-c) in [78]), respectively. To make a fair comparison, the pixel selection thresholds for all the three methods were established based on a phase standard deviation of around 15° . Then the corresponding thresholds for each strategy can be selected. Similar displacement trends have been detected by all of them, and the maximum displacement velocity reaches up to -3.5 cm/year (the minus sign means movement away from the satellite, i.e., downslope motion due to the landslide orientation). Within the landslide limits, there are mainly three large displacement subareas (indicated by the red rectangles in Fig. 3.2),

located at the El Pic de Maians (subarea A), costa de les Gerqueres (subarea B) and Cal Borró-Cal Ponet (subarea C), respectively. These three subareas' locations and displacement patterns are coincident with the monitoring results obtained with another data set in 2011 [79]. The data set consisted on Sliding-spotlight TerraSAR and GB-SAR images, and data from inclinometers deployed in the landslide, all acquired from October 2010 until October 2011. Previous results have confirmed that the location and evolution of the landslide body have not changed significantly during the recent years. This fact is in good agreement with the geological expectations.

Among the three pixel selection methods, D_A and TSC select pixels that behave as point scatterers while TPC can work on both point and distributed scatterers (DSs). Since there are many DS pixels (e.g., the road) in the study area, TPC obtains a much higher density of pixels than D_A and TSC approaches. Notice in Fig. 3.2 how well the TPC method has identified those pixels along the downhill road, while the other two have just selected a reduced set of them. At the same time, the TSC method obtains more PSs than D_A . This can be explained by the fact that the D_A method is very sensitive to the amplitude changes that highly directive scatterers produce when the local incidence angle changes from image to image. Specifically, the number of CSs obtained by TPC method is 757,086, the counterparts of TSC and D_A methods are 139,065 and 294,484, respectively. The improvement of the TPC and TSC methods on D_A is around $\times 5.4$ and $\times 2.1$, respectively. The TPC method thus has the best performance in terms of obtained valid pixels' density.

3.2.2.2 Comparison with GPS Measurements

The displacement velocities of the 37 GPS control points have been projected to the LOS direction to compare them with the DInSAR results, as shown in Fig. 3.2(d). In subarea A of Fig. 3.2(d), a small displacement with a velocity around -1 cm/yr has been detected. In the subarea C, significant movement with velocity around -4 cm/yr has been monitored by the GPS. In the subareas A and C, the GPS and PSI measured displacement velocities are consistent with each other. Unfortunately, no GPS points were available in the subarea B for comparison. On the contrary, large displacements have been recorded by the GPS within the subarea D (highlighted by the red rectangle in Fig. 3.2(d)), where there are no counterpart PSI pixels in its near vicinity. However, the further neighboring PSI pixels present LOS velocities about -1.5 cm/yr, providing evidence of the agreement of the GPS and PSI results also in this subarea.

To summarize the comparison, a scatter plot with the GPS and PSI derived displacements is shown in Fig. 3.3 (i.e., Fig. 11 in [78]). In this plot, the PSI displacements are estimated by averaging those of the neighbouring pixels of the related GPS measurement point (less than 50 m apart). In addition, they have been determined from the displacement time-series taking the overall two year displacement from October 2014 to October 2016, as the GPS date campaigns. As Fig. 3.3 reveals, the GPS and PSI displacements follow the same trends and present a correlation coefficient of $R^2 = 0.90$. For GPS measurement points with noticeable displacement (highlighted by the red ellipse in Fig. 3.3), their

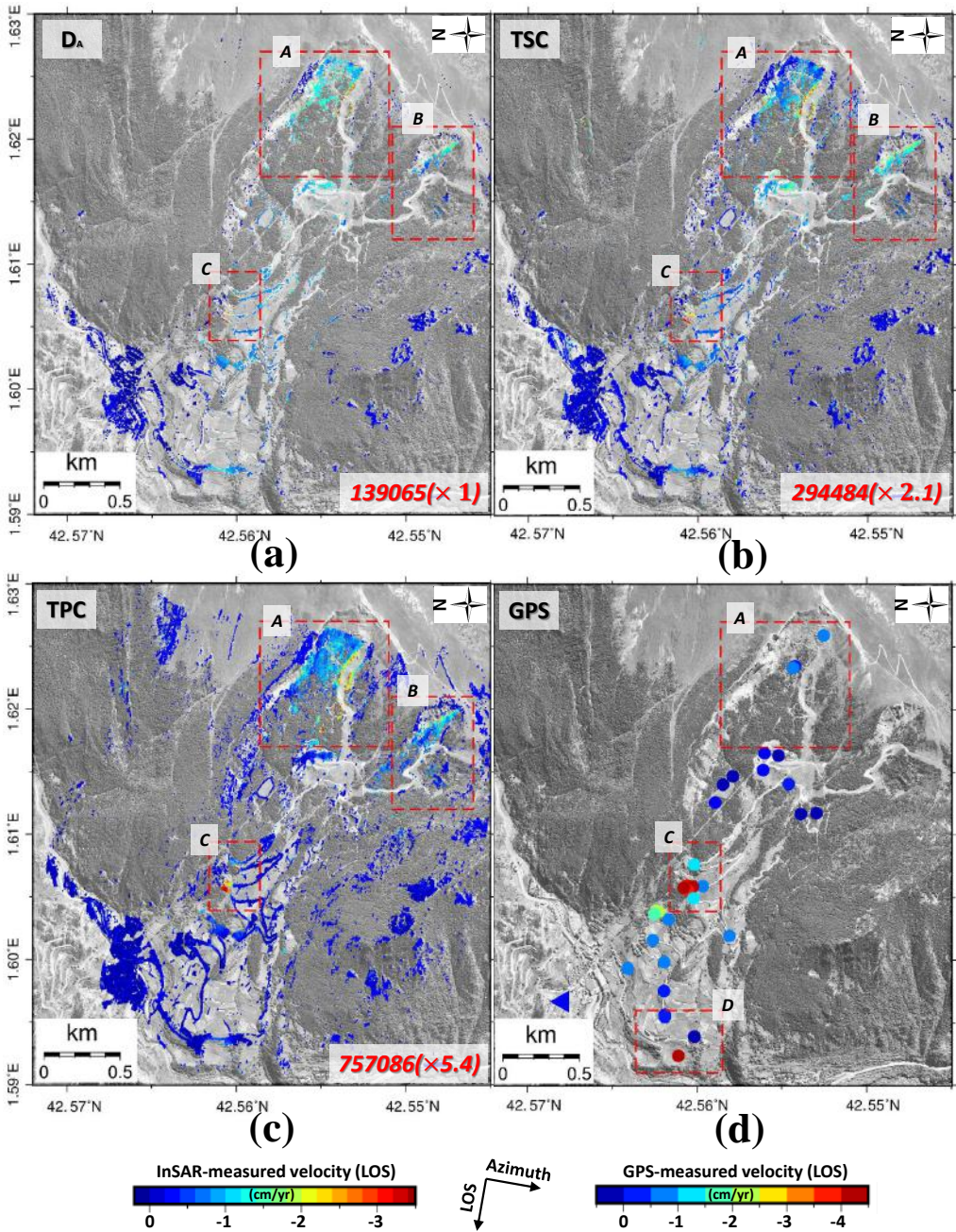


Figure 3.2: LOS displacement velocity maps derived by (a) D_A , (b) TSC, (c) TPC and (d) GPS approaches, respectively. The filled blue triangle in (d), i.e., E1, indicates the location of the GPS base point. GPS displacements have been projected to LOS. The red rectangles highlight the areas of deformation. The red numbers at the right bottom corner of (a–c) represent the amount of valid pixels obtained by each method.

surrounding PSI pixels show large displacements as well. Meanwhile, for those stable GPS measurement points (limited by the blue rectangle), with displacements between -2 to 2 cm, their corresponding PSI displacements are also within this range.

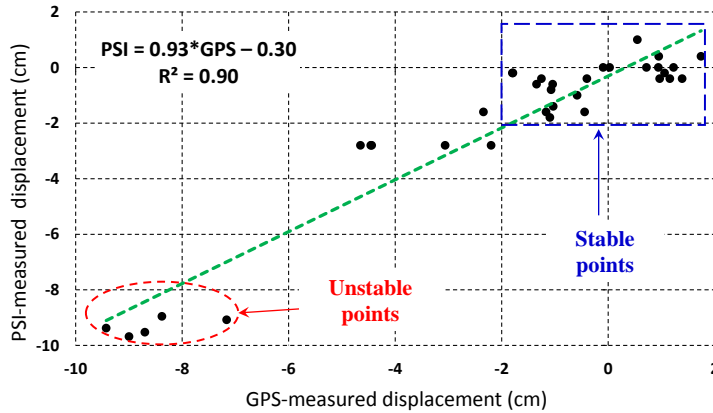


Figure 3.3: Comparison of PSI and GPS derived displacements (October 2014 to October 2016).

3.2.2.3 Summary

The results show that advanced full-resolution pixel selection strategies (i.e., the temporal sub-look coherence (TSC) and temporal phase coherence (TPC) methods) are able to obtain much more valid pixels than the classical amplitude dispersion (D_A) method. In addition, the TPC method presents the best performance among all three full-resolution strategies employed. Thanks to the huge amount of valid pixels obtained by the TPC method with SHR TSX images, the complexity of the structure of the Canillo landslide has been highlighted and three different slide units have been identified. The results of this study indicate that the TPC approach together with SHR SAR images can be a powerful tool to characterize displacement rates and extension of complex landslides in challenging areas.

3.3 Coherency Matrix Decomposition Based Polarimetric Persistent Scatterer Interferometry

This section is based on: Feng Zhao and Jordi Mallorqui, *Coherency Matrix Decomposition Based Polarimetric Persistent Scatterer Interferometry*, IEEE Transactions on Geoscience and Remote Sensing, 2019 [80] (See **Section 5.3**).

3.3.1 Introduction

In [77] and [78] the TPC pixel selection approach for single-polarimetric PSI techniques has been proposed and tested in different scenario. As more and more SAR sensors are capable of acquiring polarimetric SAR data sets, it is necessary to investigate pixel optimization and selection methods by employing polarimetric SAR images. The rationale of polarimetric optimization techniques, i.e. PolPSI techniques, is to enhance the phase quality of the interferograms by combining adequately the different polarization channels available to produce an improved one. Different approaches have been proposed for interferometric phase optimization of Polarimetric Persistent Scatterer Interferometry (PolPSI). They range from the simple and computationally efficient BEST, where for each pixel the polarimetric channel with the best response in terms of phase quality is selected, to those with high computational burden like the Equal Scattering Mechanism (ESM) and the Sub-Optimum Scattering Mechanism (SOM).

BEST is fast and simple but it does not fully exploit the potentials of polarimetry. On the other side, ESM explores all the space of solutions and finds the optimal one, which is very time-consuming and may limit its applications in practice for large scenes. Other efficient methods [41,42] have been investigated to reduce the computation time of polarimetric coherence optimization. Unfortunately, they can hardly be applied on polarimetric optimizations that based on full-resolution quality metrics, like D_A .

In [80] (i.e., **Section 5.3**), a new PolPSI approach with a good compromise between computation burden and phase optimization performance is proposed. This approach has been named as CMD-PolPSI and it uses the coherency matrix decomposition to determine the optimal polarimetric channel. It does not have to search for the solution within the full space of solutions and the optimization, despite it is not as optimal than with ESM, outperforms BEST. To assess the performance of the proposed CMD-PolPSI, it has been tested with three different PolSAR data sets. One is the quad-pol Radarsat-2 images acquired over Barcelona (Spain), the other two are dual-pol TerraSAR-X and Sentinel-1B data sets acquired over Murcia (Spain) and Mexico City (Mexico), respectively. All the three test sites are affected by subsidence phenomena. The benefits of the proposed CMD-PolPSI regarding phase quality improvement and pixel densities of the final deformation maps have been evaluated and discussed in [80] (i.e., **Section 5.3**). The main results corresponding with the Barcelona study area are presented in the following section (i.e., **Section 3.3.2**) to demonstrate the effectiveness of the proposed CMD-PolPSI.

3.3.2 Main Results

D_A is a good estimator of phase quality for values below 0.4 [10]. The smaller the D_A , the better the phase quality. Typical thresholds are set to 0.25 as they lead to a good compromise between phase quality and pixels' density.

3.3.2.1 Phase Optimization Results

D_A histograms obtained with the different approaches over Barcelona are presented in Fig. 3.4 (i.e., Fig. 2 in [80]). It can be seen from Fig. 3.4(a) that all optimization methods improve pixels' phase qualities, w.r.t the HH channel, for D_A below 0.4. Fig. 3.4(b) shows a detailed view of the histograms in the pixel selection range, this is $D_A < 0.25$. As expected, ESM is the technique that has the best optimization performance. Except ESM, the proposed CMD-PolPSI achieves the best optimization results, closely followed by SM-BEST and SM1 in the range of pixel selection. SM1 performs a little slightly below SM-BEST, as the two histograms (black and blue lines in Fig. 3.4(b)) overlap, but much better than BEST. This implies that if there is one dominant scattering mechanism (SM) within one pixel, which is the case for good PSs, it can be well represented by the first eigenvector of its full-pol coherency matrix. For lower quality pixels out of the selection range, the first eigenvalue produces worst results and its performance is even below the single HH channel, as it is shown by Fig. 3.4(a).

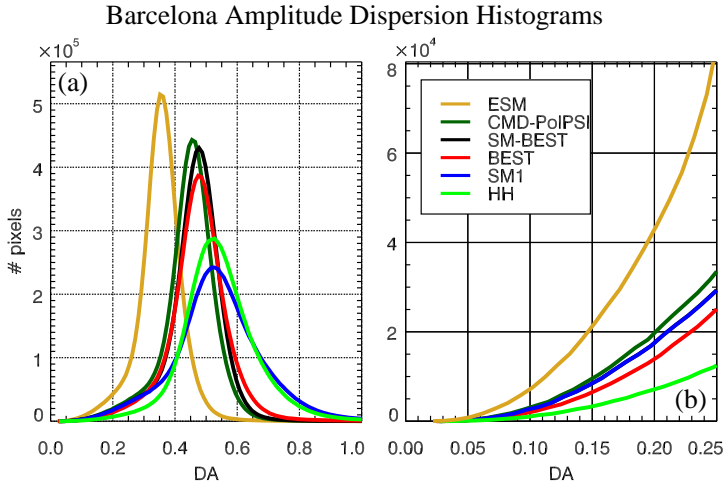


Figure 3.4: (a) Dispersion of amplitude (D_A) histograms using HH polarimetric channel or the SM1, BEST, SM-BEST, ESM and the proposed CMD-PolPSI D_A optimization methods over Barcelona. (b) Detail for D_A values from 0 to 0.25.

3.3.2.2 Ground Deformation Monitoring Results

Ground deformation results estimated by the BEST, CMD-PolPSI and ESM approaches are shown in Fig. 3.5 (i.e., Fig. 3 in [80]). All methods, using a D_A threshold of 0.25 (around 15°), have provided similar results in terms of location, magnitude and extend of the different deformation bowls but with different final PS pixel densities. In order to compare the final densities, the results of the HH channel have been used as a reference. Using only the HH channel 78,454 valid pixels have been obtained. BEST is able to rise its number to 164,152, which implies an improvement of 109%. CMD-PolPSI achieves

203,030 pixels, an improvement of 159%. Comparing both methods, the proposed CMD-PolPSI is able to retrieve 38,878 additional pixels w.r.t. the BEST method, which accounts for 24% more than BEST. This better performance of CMD-PolPSI is due to the fact that it explores the optimal SM in a more extended space (HH, VV, HV, SM1, SM2 and SM3). As shown in Table II of [80] (i.e., **Section 5.3**), SM1 represents the 63.5% of the final PS pixels while the other two SM have a marginal contribution. HH and VV channels have similar weights in the obtained pixels, around 10.7%, and HV channel a 15.0%. As expected, the ESM optimization is able to reach the highest density with 499,028 final PS pixels obtained, which represents improvements of 536% w.r.t. the HH case and 146% w.r.t the CMD-PolPSI. However, the computational burden of ESM is much higher than that of CMD-PolPSI. Particularly, for the Barcelona full-pol data set (1602×4402 pixels), ESM takes 271,900 seconds (around 75.5 hours) for the D_A based phase optimization and the CMD-PolPSI just 1,068 seconds (around 0.3 hours), which is 255 times faster than ESM. The experiment has been carried out on a workstation equipped with an 8-core Intel(R) Xeon(R) E5620 processor (2.4 GHz) and 60 GB of RAM. The implementation of the software is in IDL.

To conclude, the results show that CMD-PolPSI presents better optimization results than BEST method. Compared with the ESM algorithm, CMD-PolPSI is much more faster but its performance is not as optimal.

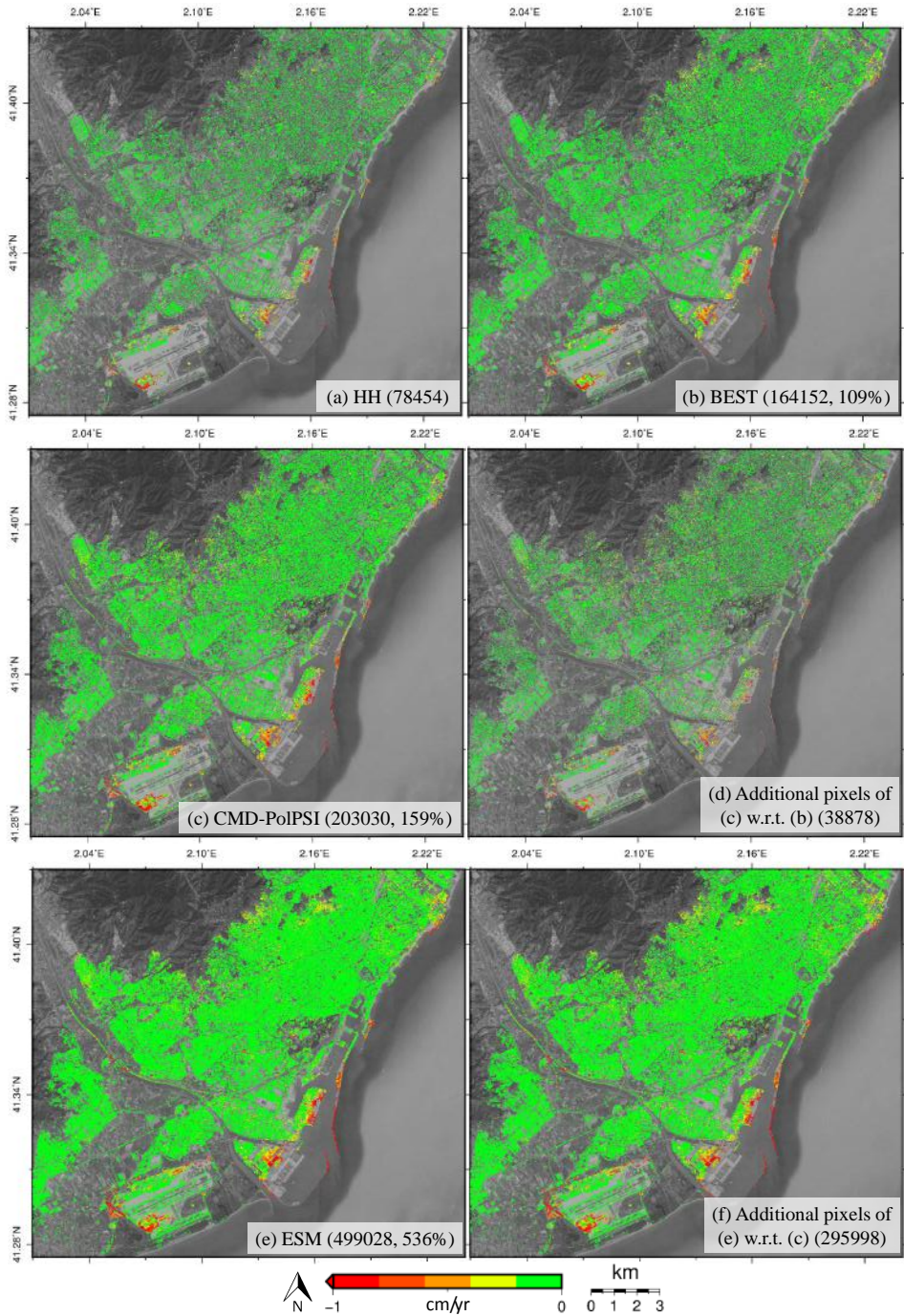


Figure 3.5: Ground deformation estimated by (a) HH, (b) BEST, (c) CMD-PolPSI and (e) ESM approaches over **Barcelona**. (d) the additional pixels of CMD-PolPSI w.r.t. BEST, and (f) the additional pixels of ESM w.r.t. CMD-PolPSI. The number in brackets represents the final number of PS pixels for each approach, and the improvement percentage is w.r.t. those derived by the HH approach.

3.4 Deterministic and Distributed Scatterers Joint Processing For Polarimetric PSI (PolPSI)

This section is based on: Feng Zhao and Jordi Mallorqui, *SMF-POLOPT: An Adaptive Multi-temporal Pol(DIn)SAR Filtering and Phase Optimization Algorithm for PSI Applications*, IEEE Transactions on Geoscience and Remote Sensing, 2019 [81] (See **Section 5.4**).

3.4.1 Introduction

In [80] (i.e., **Section 5.3**), an efficient PolPSI technique CMD-PolPSI has been proposed. Like the other conventional PolPSI algorithms [36], it optimize interferometric phases through either D_A (good for PSs) or coherence stability (good for DSs). However, as PSs and DSs are present in real scenarios more adaptive PolDInSAR optimization algorithms have been proposed to deal simultaneously with both. Inspired by SqueeSAR [18], Navarro-Sanchez proposed an adaptive PolDInSAR optimization method, which is based on a spatial adaptive speckle filtering approach that can jointly process DS and PS pixels [58]. As expected, this new method can achieve higher pixel densities than the conventional ones. However, as it has to carry out a similarity test to identify polarimetric homogeneous pixels (PHPs) [58] for each pixel, its computation burden is high.

In [81] (i.e., **Section 5.4**), we propose an alternative adaptive Pol(DIn)SAR optimization algorithm that avoids the time-consuming similarity test for PSI applications. This algorithm is mainly based on the extension of Lee's PolSAR filter [82] and polarimetric optimization techniques [36, 58]. It first utilizes PolSAR classification results and pixels' scattering mechanisms to identify for each pixel its polarimetric homogeneous pixels (PHPs) [58] and classify it as DS or PS. Then, DS pixels are filtered with the Minimum Mean Square Error (MMSE) method [83] based on their associated PHPs, while PS pixels are preserved with no further modifications. After that, DS and PS pixels are optimized based on their coherence, γ , and dispersion of amplitude, D_A , respectively. Finally, the optimized DS and PS pixels are jointly processed to estimate the deformation.

To validate the feasibility and evaluate the performance of the proposed algorithm, it has been tested with two different data sets. One with quad-pol Radarsat-2 data acquired over Barcelona airport (Spain) and the other with dual-pol TerraSAR-X data acquired over Murcia (Spain). Both scenarios are affected by subsidence phenomena. The benefits of the proposed approach in terms of phase quality improvement and higher pixel densities of the final deformation maps have been assessed and discussed in [81] (i.e., **Section 5.4**). The main results of this study associated with the Barcelona airport area are employed to illustrate the effectiveness of this algorithm in the following section (i.e., **Section 3.4.2**).

3.4.2 Main Results

3.4.2.1 PolSAR Filtering Result

One PolSAR image over Barcelona airport has been used to illustrate the effectiveness of the SMF adaptive filter. Besides SMF, the PolSAR image has been also filtered with another two well established filters, i.e the Lee's scattering-model-based speckle filtering (Lee SM) [82] and the intensity-driven adaptive-neighborhood filtering (IDAN) [84], in order to compare their performances. The results are presented in Fig. 3.6 (i.e., Fig. 3 in [81]), where the original PolSAR image is also shown to visualize the noise reduction each filter is able to achieve. All the three filters have reduced the PolSAR image's speckle noise, however the proposed SMF strategy can better preserve the details of structures while the other two tend to blur their edges.

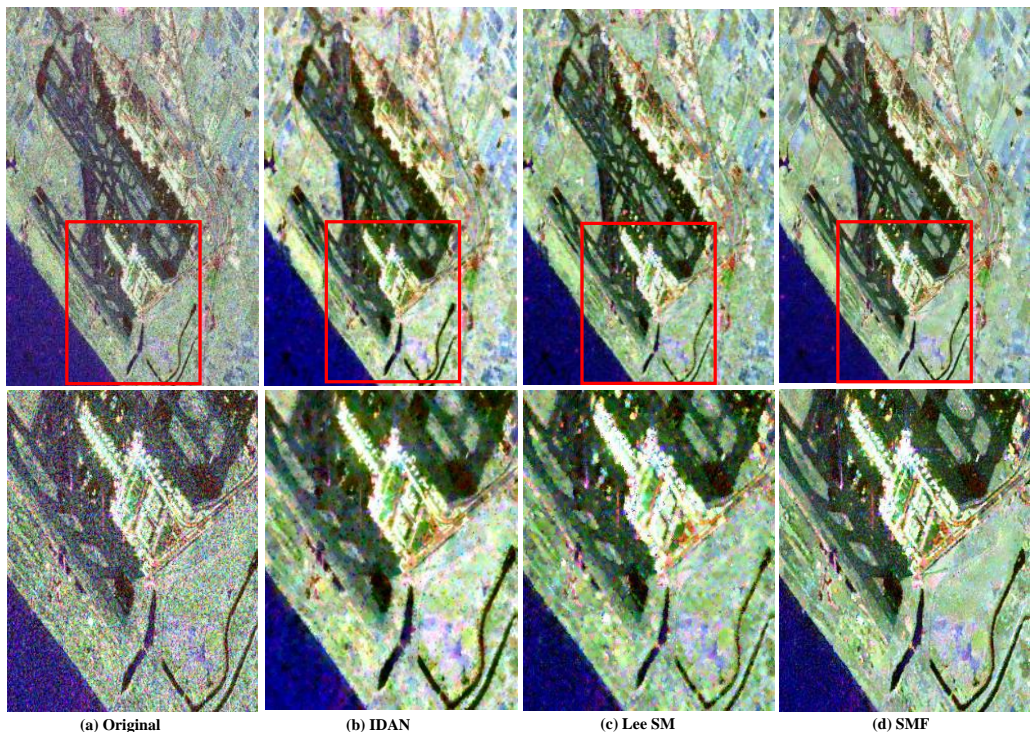


Figure 3.6: Original and filtered Pauli RGB composites over the Barcelona airport. Bottom row shows the close-up of the area limited by the red rectangle in the top row. The color channels are $R = HH - VV$, $G = 2HV$, and $B = HH + VV$.

3.4.2.2 Polarimetric Optimization Results

The performance of the proposed algorithms is evaluated in terms of phase optimization and pixels' densities of the derived deformation maps. In order to better illustrate the advantages of the proposed approaches, i.e. the SMF and SMF-POLOPT, they have been compared with other two conventional full resolution methods, i.e. D_A (only the HH channel) and ESM- D_A (referred hereafter as ESM for the sake of simplicity). SMF results correspond also to the HH channel.

During the generation of the interferograms, except for the D_A approach, the other three methods filter or optimize DInSAR phases taking advantage of the polarimetric data. Fig. 3.7 (i.e., Fig. 5 in [81]) shows the optimized phases with the different methods of a Radarsat-2 interferogram over Barcelona airport. The unfiltered HH channel's phase is also included for comparison purposes. The ESM method is able to maximize the phase quality mainly on PSs, like in the airport terminal and building areas as seen in Fig. 3.7(c). The SMF-POLOPT and SMF approaches significantly reduce the phase noise level on DSs, e.g., the runway areas as seen in Fig. 3.7(a) and Fig. 3.7(b). As expected, the SMF-POLOPT method shows a better performance than SMF thanks to the further polarimetric optimization of the adaptively filtered interferograms. Good examples of this are the roads highlighted by the black dashed lines in Fig. 3.7(a). Fig. 3.8 (i.e., Fig. 6 in [81]) shows the close-up of the airport terminal section of Fig. 3.7. As the SMF-POLOPT can adaptively optimize both PSs and DSs, it presents the best performance among all methods.

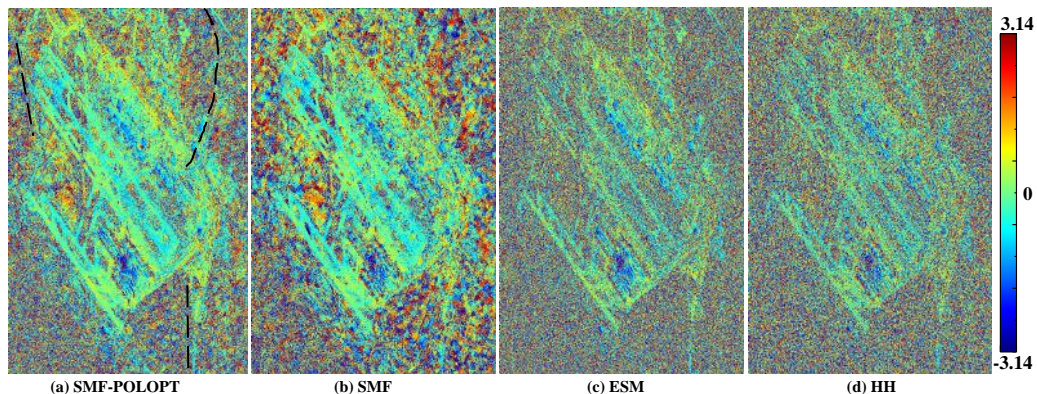


Figure 3.7: An interferogram phase optimization results of Barcelona airport by different algorithms. The black dashed lines in (a) indicate the locations of roads where the SMF-POLOPT approach presents the best optimization effect.

3.4.2.3 Ground Deformation Monitoring Results

After generating the differential interferograms, those pixels with phase qualities over a given threshold are selected. For D_A and ESM method, pixels with D_A values below 0.25

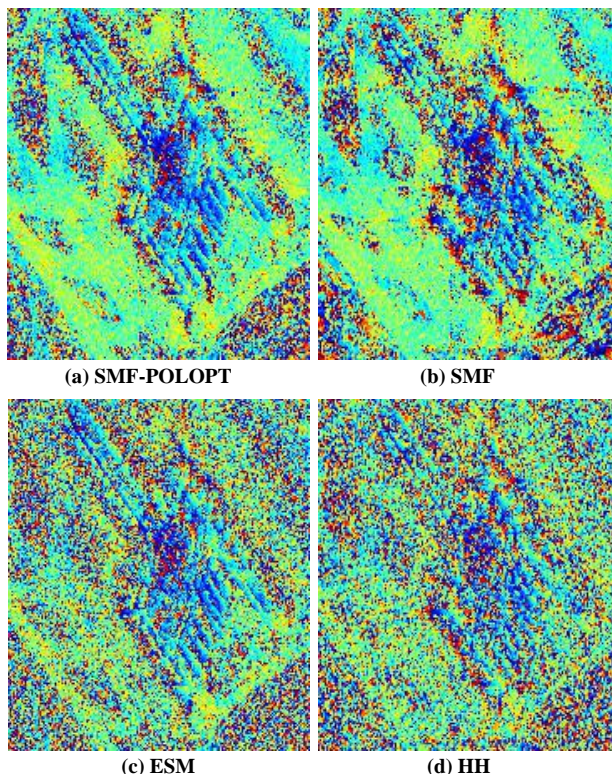


Figure 3.8: Close-up of the phase optimization results of Fig 3.7, which corresponds to the area of the airport terminal.

are selected. The pixel selection strategies for the SMF-POLOPT and SMF approaches are identical and they follow the method introduced in the previous section. To make a fair comparison, the same phase standard deviation threshold (around 15°) is used for all cases during pixel selection. Finally, based on the selected pixels and generated interferograms, the CPT algorithm is used to estimate the deformation.

For Barcelona Airport full-pol Radarsat-2 data, the retrieved deformation velocity maps are shown in Fig. 3.9 (i.e., Fig. 7 in [81]). Very similar subsidence trends are detected by all four approaches, which illustrates the goodness of the proposed algorithms. The subsidence areas are mainly located at the airport access road and terminal T1 areas, and the maximum subsidence velocity reaches up to 2.5 cm/year. The deformation amount and patterns are in good accordance with previous studies [35, 36, 58], which further validates the reliability of the results.

As Fig. 3.9 shows, all the three advanced algorithms perform better, in terms of pixels' densities, than the classical single-pol D_A method. The density improvement of ESM with respect to single-pol D_A is around $\times 2.7$ (11,248 compared to 4,149). The improvement is mostly due to the polarimetric optimization provided by ESM as the three polarimetric

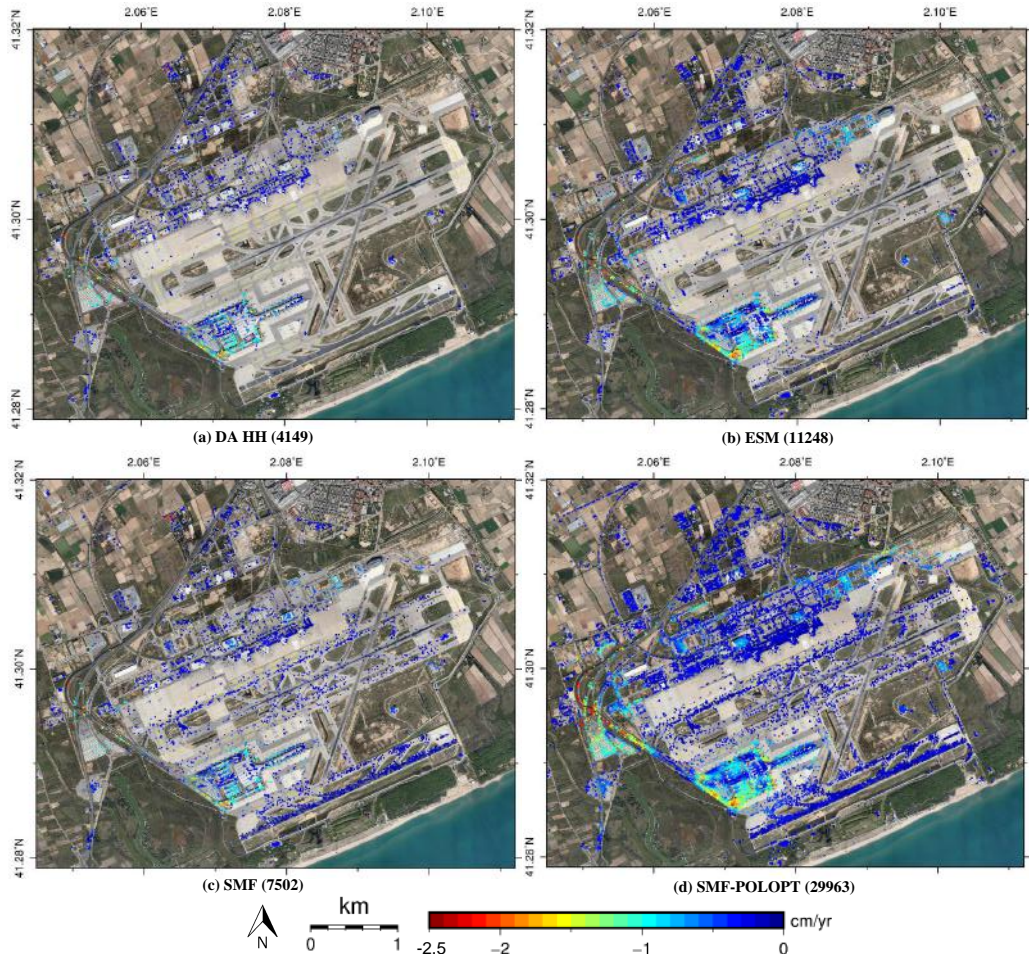


Figure 3.9: Barcelona airport ground deformation velocity maps obtained by (a) D_A , (b) ESM, (c) SMF and (d) SMF-POLOPT. The number in the brackets represents the amount of pixels in each algorithm derived deformation result.

channels are combined into a single one. The SMF method applied to HH channel achieves an increase of pixels of around $\times 1.8$ w.r.t. single-pol D_A (7,502 versus 4,149). This improvement is due to the inclusive pixel filtering and selection strategy in SMF, which is able to reduce DS pixels' noise and identify high quality pixels from both PS, over buildings, and DS, over runways. As expected, the highest pixel densities are obtained by SMF-POLOPT, as it combines the benefits of the adaptive filtering with the polarimetric optimization of data. The increase of SMF-POLOPT w.r.t. single-pol D_A is around $\times 7.2$ (29,963 compared to 4,149). The highest pixel density allows SMF-POLOPT to better detect and characterize the extend and details of ground motion than the other methods.

4

CHAPTER 4 CONCLUSIONS

4.1 Main Conclusions

This PhD thesis is dedicated to investigate advanced pixel optimization and selection methodologies for PSI applications by using both single- and multi-polarimetric SAR image stacks. To this end, related research work have been carried out and four related articles have been finished. Particularly, a new pixel selection approach based on TPC has been proposed in [77] (i.e., **Section 5.1**), its effectiveness and advantages have been further verified by applying it on landslid monitoring in [78] (i.e., **Section 5.2**). For PolPSI techniques, to overcome the limitation of high computation burden, a new computational efficient PolPSI method named as CMD-PolPSI has been proposed in [80] (i.e., **Section 5.3**). To adpative optimize PS and DS pixels, in [81] (i.e., **Section 5.4**), an adaptive pololarimetric phase optimization algorithm has been proposed.

The main contributions and conclusions of this thesis may be summarized as follows:

- **High phase quality pixel selection with TPC**

In [77] (i.e., **Section 5.1**) a full-resolution Interferometry SAR (InSAR) phase quality estimator, i.e. the temporal phase coherence (TPC), has been proposed and used to identify high quality pixels in SAR images. Instead of using the temporal variation of pixels' amplitude like D_A or the temporal stability of the coherence, TPC estimates pixels' phase quality directly from its interferometric phase noise at full

resolution. For each pixel, the interferometric phase systematic terms are firstly eliminated in order to leave just the noise term in the interferometric phase. Then, the TPC is calculated based on the pixel-based noise phase term of all interferograms.

The impact of the interferograms' generation way (single-master (SM) or the multi-master (MM)) on TPC estimation has been studied. It is found that the relationship between SM-TPC $\hat{\gamma}_{TPC}^{SM}$ and MM-TPC $\hat{\gamma}_{TPC}^{MM}$ is constrained by the lower bound $\hat{\gamma}_{TPC}^{MM} = (\hat{\gamma}_{TPC}^{SM})^2$ and the upper bound $\hat{\gamma}_{TPC}^{MM} = \hat{\gamma}_{TPC}^{SM}$. To better complete the pixel selection, the relationship between TPC and phase standard deviation (STD) has been derived through simulation. Thus, the TPC threshold can be accurately determined according to the requirement of the phase STD of the pixels. The influence of the neighboring window size on the value of TPC has been studied, as well. For the Barcelona airport data set, it is found that window sizes larger than 21×21 do not imply any noticeable improvement in the results and increase the processing time. Considering efficiency and reliability, window sizes of 21×21 are a good choice for TPC estimation.

To validate the feasibility of the proposed pixel selection algorithm, it has been tested together with the other two classical approaches (D_A and SPC). The detected deformation patterns of all three methods over Barcelona Airport are very similar and consistent with previous studies, which validates the feasibility and effectiveness of TPC. Comparing the results obtained with the three methods, TPC shows some advantages. When comparing with D_A , besides the pixels selected by D_A it can identify much more other (about 3.2 times of that obtained by the D_A approach over the Barcelona airport study area) as it is able to detect stable pixels, independently if they are PSs or DSs. Moreover, it is more flexible regarding the number of SAR images necessary for a reliable selection. When comparing with SPC, TPC preserves the original resolution of the SAR image as no multilooking is applied. Low quality pixels surrounded by high quality ones will not be wrongly selected as the multilooking causes an overestimation of its quality. Similarly, isolated high quality pixels have a lower probability to be underestimated due to their low quality neighbors. As a result, more pixels can be selected (about 1.5 times of that obtained by SPC approach over the study area).

The computation cost of TPC, which is determined mainly by the size of the neighboring window, is low and affordable for all cases. This pixel selection strategy is also easy to implement and incorporate into any advanced PSI processor.

- **Landslide monitoring by SHR SAR images together with advanced PS selection strategies**

In [78] (i.e., **Section 5.2**) the ability of SHR SAR images together with advanced PS selection strategies for regional-scale landslide monitoring in a challenging area has been studied. Thirty-two SHR TerraSAR-X (TSX) images (July 2014 to October 2016), with resolutions of 0.23 and 0.59 m in azimuth and range directions, have

been employed to monitor the Canillo landslide (Andorra) by using PSI techniques with three different pixel selection methods.

The study has demonstrated that improving the number of high-quality pixels for its later PSI processing results of crucial importance in landslide monitoring in natural environments. Under the application point of view, to the author's knowledge, it is one of the first times when such a high density of valid pixels has been obtained in mountainous areas. SHR SAR data jointly with advanced full-resolution PSI strategies allow the achievement of a more robust network of valid pixels (improving the linear estimation without propagation errors and the reliable estimation of APS) and thus favors the reliable estimation of displacement maps in a major number of points inside a landslide. This is a general conclusion that does not depend on the landslide. A different issue is if the particularities of a given landslide (orientation, type of vegetation coverage, local topography, snow episodes, etc.) made it unsuitable for PSI monitoring. Similarly, well-established interferometric techniques for DEM generation fail on forested areas. It is clear that the particular characteristics of the scenario may limit the application of the technique.

The landslide's overall displacement patterns observed by the three methods in El Forn de Canillo are similar. Three main subareas with noticeable displacement have been detected, which are similar to those obtained in previous PSI monitoring results. This indicates that the evolution of the landslide main body did not change significantly during recent years. The PSI measured displacement rates have been compared with GPS measurements of the same period, and they are both in good agreement. Although already highlighted in the literature, in the Canillo Landslide, the PSI capability for detecting incipient movements in zones not previously surveyed by the geological engineering specialists has been verified. The displacement time-series of two significant pixels are characterized by considerable nonlinear components, exhibiting some acceleration and stabilization periods within each year. These periods can be correlated with the averaged monthly precipitation amounts, revealing the important influence of rain/snow melting episodes on the development of this landslide.

SHR SAR data initially designed for improving monitoring capabilities over man-made structures, such as buildings, bridges, railways or highways, have also demonstrated an outstanding performance over natural reflectors, such as outcrops or exposed rocks with the proper pixel selection strategy. Indeed, this improvement in terms of density allows a better characterization and delineation of complex landslides. Among the three full-resolution pixel selection strategies, the advanced ones (i.e., the TSC and TPC) are able to obtain much more valid pixels than the classical D_A method. The TPC method presents the best performance. Thanks to these huge amount of valid pixels, the displacement details of the regional-scale landslides can be characterized with better precision when combining the TPC method with SHR TSX data. Compared with the lower-spatial resolution SAR data (Sentinel-1A in this study), SHR data can better characterize the landslide, particularly if the different subareas are small.

The results of this part of work show that the density of valid pixels can be greatly enhanced by using the TPC method together with SHR SAR images. Thus, they can together be used as a powerful tool for detailed landslide monitoring in difficult areas.

- **Computationally efficient PolPSI**

In [80] (i.e., **Section 5.3**) a new Polarimetric Persistent Scatterers Interferometry (PolPSI) algorithm based on the coherency matrix decomposition has been proposed. This PolPSI algorithm, referred as CMD-PolPSI, produces optimization results better than the simple BEST approach. On the other side, the ESM methods outperforms CMD-PolPSI but its high computational burden reduces its applicability to large areas. CMD-PolPSI, thus, constitutes a good compromise between pixel density improvement and computational burden. Two approaches have been developed, one oriented to permanent scatters (PS) that uses the dispersion of amplitude D_A as pixel selection criteria, and the other better for distributed scatterers (DS) based on the mean coherence from multilooked interferograms.

Three complementary data sets in terms of polarization (Radarsat-2 full-pol, TerraSAR-X and Sentinel-1 dual-pol), wavelength (C and X-band) and image resolution have been used to evaluate the performance of the proposed algorithm in different conditions. In terms of interferometric phase optimization, CMD-PolPSI presents better performance than BEST in all three data sets and, as expected, below ESM. The best results are always achieved with full-pol data at the highest resolution.

With the D_A approach, for full-pol data the improvement obtained by CMD-PolPSI in final PS pixels' density has been 159% w.r.t. the single-pol HH processing while BEST has been able to improve only by a 109%. The dual-pol datasets have produced lower improvements, for TerraSAR-X data a 62%, compared with the 40% of BEST, and for Sentinel-1 a 63%, while BEST has been a 37%. For all three cases, ESM has been able to produce improvements of 536%, 137% and 148% respectively. The full-pol dataset has been used to generate all possible dual-pol combinations in order to evaluate, under exactly the same conditions, which one performs better. Among them, HH+VV data is the one that produces the highest improvement in number of selected pixels.

The coherence approach with multilooked interferograms has produced lower improvements and, as a general rule, the lower the interferograms resolution (as a combination of the original image resolution and applied multilook) the worst the polarimetric optimization performs. Using the same phase quality threshold as with the D_A approach, the improvements achieved by CMD-PolPSI on numbers of final PS pixels are limited to 40%, 32% and 3% w.r.t the single-pol case for Radarsat-2, TerraSAR-X and Sentinel-1, respectively. It is worth to note that if the selection threshold is more restrictive, this is higher coherence values, the improvements increase as well. For instance, coherencies above 0.9 produce improvements of 139%, 59% and 27% by CMD-PolPSI w.r.t. single-pol case, respectively. In this case,

with the highest coherence thresholds, pixels with a single and significant scattering mechanism are being selected.

Compared with the powerful ESM algorithm, the proposed CMD-PolPSI has a lower computational burden, being around 255 times faster with full-pol data for the D_A based optimization (full resolution optimization). On the other hand, ESM presents much better optimization results as it is able to explore the full space of polarimetric scattering mechanisms. In practice, CMD-PolPSI is able to provide a good compromise between computational burden and pixels' density improvement when performing PSI processing in cases that wide areas have to be processed.

- **Deterministic and distributed scatterers jointly processing for PolPSI**

In [81] (i.e., **Section 5.4**) an adaptive multi-temporal Pol(DIn)SAR filtering and phase optimization algorithm, i.e. SMF-POLOPT, has been proposed. It is inspired by Lee's PolSAR filter [82] and PolDInSAR optimization techniques [36, 58]. This algorithm, which is based on the Scattering-Mechanism based Filtering (SMF) and adaptive POLInSAR OPTimization (POLOPT), can separately filter or (and) optimize PS and DS pixels. Moreover, an inclusive pixel selection method based on pixels' phase standard deviation (STD) has been introduced and developed to identify high quality pixels for PSI processing in this scheme.

Two SAR data sets, full- and dual-polarization, have been used to evaluate the performance of the proposed algorithm. For PolSAR filtering, the SMF achieves the speckle reduction and details preservation simultaneously, and it outperforms the other two well established PolSAR filters [82, 84]. In terms of PolDInSAR phase optimization, the proposed SMF-POLOPT presents better performance than the other algorithms. In both test areas, significant improvements regarding pixels' densities have been achieved by the SMF-POLOPT algorithm. Particularly, an increase of around $\times 7.2$ and $\times 3.8$ in the number of pixels w.r.t. the single-pol D_A method have been achieved with the SMF-POLOPT approach with Barcelona (full-polarization) and Murcia (dual-polarization) SAR data sets, respectively. The corresponding improvements achieved by the ESM and SMF algorithms are $\times 2.7$ and $\times 1.8$ for the full-polarization case, $\times 2.4$ and $\times 1.7$ for the dual-polarization case w.r.t. the single-pol D_A method, respectively.

The advantages and shortcomings of the four employed ground deformation monitoring algorithms have been discussed and analyzed. The proposed SMF method can adaptive filter DS pixels and preserves PS ones, it is thus a good alternative to the ESM approach that mainly optimizes PS pixels. When a high computation cost is acceptable, SMF-POLOPT is the best one among the four methods for both dual- and full-pol SAR data. The proposed adaptive filtering and phase optimization algorithm, i.e. SMF-POLOPT, can be used for adaptive Pol(DIn)SAR images' filtering or interferograms' polarimetric optimization when multi-temporal PolSAR images are available.

To conclude, [77] (i.e., **Section 5.1**) and [78] (i.e., **Section 5.2**) answer the first research question of this thesis, i.e., “*How to identify high phase quality pixels from both PS and DS pixels for PSI applications?*”. The second research question “*How can the interferometric phases be efficient optimized by polarimetric optimization techniques?*” is partially answered by [80] (i.e., **Section 5.3**). The last one “*How can PS and DS pixels of multi-temporal PolDInSAR images be jointly processed to reduce the influence of decorrelation on PSI applications?*” has been answered by [81] (i.e., **Section 5.4**).

4.2 Future Research Lines

There are several open questions and research lines related to the work presented in this thesis that deserve further investigations, the key ones are listed as follows.

- **Polarimetric optimization by using TPC**

The proposed TPC could be used as the interferometric phase quality metric in polarimetric optimization for PolPSI techniques. It should be more effective than the classical D_A or coherence stability as it is applicable on both PSs and DSs. The TPC optimization procedure need to be carefully designed to minimize the computational burden as much as possible, the advantages and flexibility of the TPC based PolPSI required further detailed investigations.

- **Similarity metric to identify spatio-temporal homogeneous SAR pixels**

As more and more time-series SAR images are being acquired everyday, the development of similarity metrics between pixels, which consider spatio-temporal phase and amplitude information of SAR images, for Homogeneous Pixel (HP)s’ identification could be an interesting research topic. This research could be started with the already existing similarity metrics that are mostly for the single-temporal case. For instance, the one in NL-SAR [85] could be extended to multi-temporal cases. It is worth to mention that the computation cost for the estimation of the designed similarity metric is also an important issue to be considered, since it should be applicable for large areas.

- **CMD-PolPSI built by other coherency matrix decomposition algorithms**

As it has been discussed in [80] (i.e., **Section 5.3**), variants of the proposed CMD-PolPSI could be obtained by replacing the eigenvector-based decomposition with others like the classical Huynen and Cloude decomposition [76] or the advanced Yamaguchi decomposition [86–88]. Moreover, a combination of two or more different PolSAR decomposition approaches could be used to retrieve different scattering mechanisms contained within pixels. In this way, better interferometric phase optimization effects could be achieved thanks to that extended exploring solution spaces.

In addition, the factors that undermine polarimetric optimization, like structures' orientations, could be better accounted for.

- **Homogeneous SAR pixels' identification by advanced (Pol)SAR classification methods**

The H/A/Alpha-Wishart PolSAR classifier [76, 89–91] has been used for the PHP identification in [81] (i.e., **Section 5.4**). Similarly, other latest (Pol)SAR image classification methods could be used to identify HPs. Particularly, the deep-learning based (Pol)SAR image classification and segmentation has recently become a research hotspot and achieved good performances than the conventional ones [92–96]. Therefore, it would be interesting to take advantage of these latest methods and apply them on HPs' identifications for SAR image filtering and PSI applications.

5

Chapter 5 Publications

5.1 Article 1. A Temporal Phase Coherence Estimation Algorithm and Its Application on DInSAR Pixel Selection

The content of this section corresponds to the publication: *Feng Zhao and Jordi Mallorqui. A Temporal Phase Coherence Estimation Algorithm and Its Application on DInSAR Pixel Selection[J]. IEEE Transactions on Geoscience and Remote Sensing, 2019 [77].*

Attention



Pages 50 to 61 of te thesis are available at the editor's web
<https://ieeexplore.ieee.org/document/8764576>

5.2 Article 2. Landslide monitoring using multi-temporal SAR interferometry with advanced persistent scatterers identification methods and super high-spatial resolution TerraSAR-X images

The content of this section corresponds to the publication: *Feng Zhao, Jordi Mallorqui, Rubén Iglesias, Josep Gili, and Jordi Corominas. Landslide monitoring using multi-temporal SAR interferometry with advanced persistent scatterers identification methods and super high-spatial resolution TerraSAR-X images[J]. Remote Sensing, 2018, 10(6), 921 [78].*

Article

Landslide Monitoring Using Multi-Temporal SAR Interferometry with Advanced Persistent Scatterers Identification Methods and Super High-Spatial Resolution TerraSAR-X Images

Feng Zhao ^{1,*}, Jordi J. Mallorqui ^{1,*} , Rubén Iglesias ² , Josep A. Gili ³ and Jordi Corominas ³

¹ CommSensLab, Department of Signal Theory and Communications (TSC), Building D3, Universitat Politècnica de Catalunya (UPC), Jordi Girona 1-3, 08034 Barcelona, Spain; feng.zhao@tsc.upc.edu

² Dares Technology, 08860 Castelldefels, Spain; riglesias@dares.tech

³ Department of Civil and Environmental Engineering, Building D2, Universitat Politècnica de Catalunya (UPC), Jordi Girona 1-3, 08034 Barcelona, Spain; j.gili@upc.edu (J.A.G.); jordi.corominas@upc.edu (J.C.)

* Correspondence: mallorqui@tsc.upc.edu; Tel.: +34-93-401-72-29

Received: 25 April 2018; Accepted: 7 June 2018; Published: 11 June 2018



Abstract: Landslides are one of the most common and dangerous threats in the world that generate considerable damage and economic losses. An efficient landslide monitoring tool is the Differential Synthetic Aperture Radar Interferometry (DInSAR) or Persistent Scatter Interferometry (PSI). However, landslides are usually located in mountainous areas and the area of interest can be partially or even heavily vegetated. The inherent temporal decorrelation that dramatically reduces the number of Persistent Scatterers (PSs) of the scene limits in practice the application of this technique. Thus, it is crucial to be able to detect as much PSs as possible that can be usually embedded in decorrelated areas. High resolution imagery combined with efficient pixel selection methods can make possible the application of DInSAR techniques in landslide monitoring. In this paper, different strategies to identify PS Candidates (PSCs) have been employed together with 32 super high-spatial resolution (SHR) TerraSAR-X (TSX) images, staring-spotlight mode, to monitor the Canillo landslide (Andorra). The results show that advanced PSI strategies (i.e., the temporal sub-look coherence (TSC) and temporal phase coherence (TPC) methods) are able to obtain much more valid PSs than the classical amplitude dispersion (D_A) method. In addition, the TPC method presents the best performance among all three full-resolution strategies employed. The SHR TSX data allows for obtaining much higher densities of PSs compared with a lower-spatial resolution SAR data set (Sentinel-1A in this study). Thanks to the huge amount of valid PSs obtained by the TPC method with SHR TSX images, the complexity of the structure of the Canillo landslide has been highlighted and three different slide units have been identified. The results of this study indicate that the TPC approach together with SHR SAR images can be a powerful tool to characterize displacement rates and extension of complex landslides in challenging areas.

Keywords: DInSAR; landslide monitoring; PSI; super high-spatial resolution TerraSAR-X images; pixel selection; measurement pixels' density

1. Introduction

Every year, with the onset of rains and snow melting, landslides represent one of the major natural threats to human life and infrastructures in natural and urbanized environments. In this context, different surveying techniques, such as inclinometers, extensometers, piezometers,

jointmeters, photogrammetry, LiDAR or Global Positioning Satellite System, are typically employed to address landslide monitoring problems [1–8]. Nonetheless, these conventional techniques present several limitations. They are labor intensive, expensive and usually require skillful users for data interpretation. Moreover, they typically provide poor spatial sampling and coverage, which hinder the characterization of complex landslides. Finally, some of these techniques require the direct installation of devices over the landslide surface, which could be a complex task, sometimes impossible to fulfill, in hard-to-reach locations. During the last decade, Synthetic Aperture Radar (SAR) Differential Interferometry (DInSAR) techniques based on space-borne SAR sensors have matured to a widely used geodetic tool for the accurate monitoring of complex displacement phenomena with millimetric accuracy [9–13]. Concretely, the new generation of X-band SAR sensors, like the German TerraSAR-X and TanDEM-X satellites or the Italian constellation Cosmo-SkyMed, have led to a scientific breakthrough presenting a lower revisiting time (up to few days) and an improved spatial resolution (even below the meter), compared with their predecessors ERS-1/2, ENVISAT-ASAR and RADARSAT-1 or the recently Sentinel-1, which worked at the C-band.

Despite all these clear advantages, DInSAR solutions present some limitations, especially for the X-band, over vegetated scenarios in mountainous environments, where landslides typically occur. The DInSAR technique takes advantage of a time-series of SAR images but not all pixels of the image are useful for interferometric processing. Only those pixels with enough phase quality along the whole observing period, i.e., the Persistent Scatterers (PSs), can be used as measurement points (MPs) to derive ground displacement. These PSs, which usually correspond to man-made structures (like buildings, bridges or roads), rocky areas and bare surfaces with no vegetation, are usually scarce in mountainous areas [14,15]. In addition, severe limitations arise from temporal decorrelation over vegetated areas, snow episodes typical in mountainous regions, layover and shadowing effects caused by SAR geometrical distortions, the presence of tropospheric atmospheric artifacts or when rapid displacements are faced, making the processing in such areas difficult and challenging at the same time. Finally, it must be taken into account that SAR sensors are only sensitive to the satellite-to-target component of displacement, i.e., line of sight (LOS) direction, which may notably differ from the real one. The measured displacement will be in fact a projection of the real one [9,12]. Many DInSAR, also known as Persistent Scatterers Interferometry (PSI), techniques and algorithms, which share similar principles, have been developed. They have been tested in the last twenty years using many different sensors, either orbital, airborne or ground-based, and over many different scenarios, making this technique a powerful and reliable tool for monitoring any kind of ground motion episodes [14–21].

Large landslides constitute a very specific and challenging scenario for DInSAR. As they are located in mountainous areas and the displacement is usually down-slope, the landslides have to be mostly oriented east to west in order to be sensitive to the displacement if polar orbital sensors are going to be used [9,10]. Not all landslides are suitable for being monitored with orbital SAR. On the one hand, to avoid problems with phase ambiguity, the displacement rate of the landslide must be small enough, let us say a few decimetres per year (depending on the wavelength and revisiting period of the radar). In other words, the SAR interferometry is suitable for monitoring landslides “Very slow” to “Extremely slow” according to the standard landslide classifications [22,23]. In addition, foreshortening and layover can jeopardize the performance of the DInSAR processing so the selection of the proper acquisition geometry is also crucial. In order to reduce geometric distortion and, at the same time, maximize the projection of the landslide displacement to the LOS, it is advisable to observe, if possible, the landslide from behind, as it has been done in this paper. However, each case can be different from the other and so it would require a detailed analysis considering the landslide particularities and the surrounding topography [9,10,12,24]. Atmospheric artifacts, caused by both tropospheric stratification and turbulent component, can contaminate the interferometric phase and, as they can be strongly correlated with the topography, they can also be difficult to remove [25–29]. Finally, a landslide can present a quite complex behaviour with different sliding units moving at different velocity rates. A good density of PS is required in order to be able to delimit and characterize

the behaviour of the different local displacements, so it would be necessary to use a PSI strategy able to select as much pixels as possible at full resolution in areas where most of the pixels will be severely decorrelated [9,10]. It is evident that the chances of detecting small and isolated PSs within decorrelated areas will arise as the resolution of the images employed increases [11,30,31].

With super high-resolution (SHR) data, the classical Gaussian scattering model used to model speckle is not always fulfilled since it is possible to find resolution cells with few scatterers [24,32]. This approach is known as partially developed speckle [33,34]. In the situation of having an isolated scatterer within the resolution cell, the value is given by the deterministic impulse response of the SAR system, i.e., by a bidimensional sinc response [24,35]. These types of scatterers typically correspond to man-made structures, outcrops, exposed rocks, etc. These objects can be exploited as opportunistic high-quality points for displacement monitoring applications. Of course, in high-resolution SAR images, it is more probable to have this situation in natural environments [11,30]. Taking into account the previous considerations, landslide monitoring will be greatly benefited by the usage of SHR data.

In this paper, 32 Staring Spotlight TerraSAR-X images (acquired from July 2014 to November 2016, with a resolution of 0.23 m in azimuth and 0.59 m in range) and three full-resolution PSI approaches (i.e., the classical amplitude dispersion [14], the temporal sub-look coherence (TSC) [36,37] and the temporal phase coherence (TPC) [38] methods) are employed to monitor a complex landslide located in El Forn de Canillo (Andorran Pyrenees). Although the advantages of the Staring Spotlight TerraSAR-X SAR data have been demonstrated by different applications such as absolute height estimation [39] and measuring rates of archaeological looting [40], the examples in terms of PSI landslide monitoring are still rare. To our knowledge, the work presented in this paper is the first attempt to study the possible benefits of SHR SAR images for landslide monitoring, especially regarding the aspects of pixel density and capability to detect PSs within decorrelated areas. At the same time, the above-mentioned three PS strategies have also been tested to determine the one most suited for this kind of scenario.

The paper is organized as follows. The landslide's geological setting and employed dataset are firstly presented in Section 2. Section 3 introduces the procedures of PSI, where the different strategies are described. Section 4 presents the landslide monitoring results with TerraSAR-X images, which are analyzed and compared with GPS measurements to evaluate their reliability. After that, in Section 5 the advantages of SHR SAR images are highlighted by the comparison of the results with those achieved with lower resolution sensors, Sentinel-1 in this case. Finally, Section 6 presents the conclusions.

2. Study Area and Dataset

2.1. Canillo Landslide

The area selected in this paper corresponds to one of the biggest and ancient landslides of the Andorran Pyrenees. It is located at El Forn de Canillo (42.5610°N, 1.6018°E) in the Principality of Andorra, which is a mountainous country between Spain and France in the Central Pyrenees, as Figure 1a shows. It is a complex structure with deposits composed of overlapped colluvial layers generated by different landslide episodes. It was firstly described by Corominas and Alonso in 1984 [41] and has been the subject of several studies where its morphology, failure mechanisms and evolution has been deeply analyzed. The hillslope of El Forn de Canillo is composed by a sequence of slides and earth-flows with a complex structure, which affects an estimated mass at around $3 \times 10^8 \text{ m}^3$. In this context, different ancient sliding units were identified in 1994 by Santacana [42] (see Figure 1b). The first one corresponds to a slide originated in the area of Pla del Gésnit-Costa de les Gerqueres, located in the southeast of the landslide, which reaches the foot of the hillside. A second event was originated under El Pic de Maïans, reaching the height of 1540 m, and which overlaps with the previous sliding unit, closing in the Valira river valley. Finally, a third rockslide with a lower extension originated on the hillside known as La Roca del Forn, in the northeast side of the hillslope, was identified. Recent local instabilities have been identified in different locations within the landslide mass [43]. The landslide of El Forn de Canillo was originated as the result of the hillside destabilization,

due to a decompression phenomenon after the removal of the Valira Glacier during the Pleistocene, after the Maximum Ice Extent. The Valira River has been progressively eroding the base of the whole mass without reaching the bedrock, and thus originating the landslide [42].

In front of some evidence of displacement (geomorphological signs of instability and some cracking in the road pavement and in a hydroelectric channel that crosses the Forn de Canillo), the authorities promoted several actions in the year 2000 for the management of their geo-hazard threats leading to the monitoring of El Forn de Canillo. Between the years 2007 and 2009, a network of geotechnical devices, including inclinometers, rod extensometers and piezometers, were installed over the landslide surface to characterize and understand the dynamics of the sliding mass. A total of 10 boreholes, reaching typically a depth between 40 and 60 m, were drilled and equipped with this instrumentation [43,44]. The readings recorded have provided evidence that, in addition to a residual movement of some millimeters per year in the main body of the slide, the most active part of the landslide corresponds to the secondary landslide of Cal Borró-Cal Ponet. This area registered a velocity up to roughly 2 cm/month between May and June 2009 when intense sudden rain events and snow melting occurred [44].

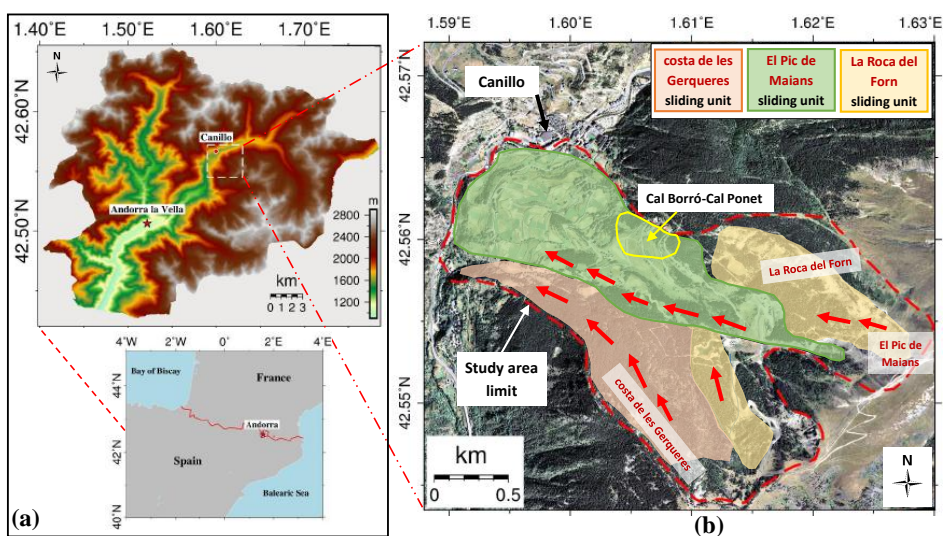


Figure 1. (a) location and topography of the Canillo landslide; (b) aerial view of the study area (Google Earth, 11 October 2017). The town of Canillo is located on the north border of the landslide. The red arrows indicate the moving directions of the ancient landslide units (modified from Santacana, 1994 [42]).

2.2. SAR Dataset

In this study, the slides' motion is monitored with 32 Staring Spotlight TerraSAR-X (TSX) Single Look Complex (SLC) SAR images. This imaging mode is the classical spotlight mode and it is able to enhance the azimuth resolution, compared with the stripmap mode, by steering the antenna in azimuth to a rotation center within the imaged scene [45]. The coverage of the SAR images is around 6.5 km in length and 3 km in width, which has been plotted in Figure 2a (yellow rectangle). The SAR image main parameters are presented in Table 1.

An amplitude image of the SAR dataset is presented in Figure 2b. As it can be seen, the SAR images' geometric distortion effects (i.e., foreshortening, shadow and layover) are not serious within the study area limit. The extended brighter areas of the image are those affected by the foreshortening and layover, due to the steepest topography. Dark areas are those affected by shadowing. This is favoured by a certain parallelism between the topography of the slope and the LOS from the satellite,

thanks to its descending flight direction. The landslide is partially vegetated. Only a few strong scatterers (man-made structures, like buildings and roads, or bare rocks) are sparsely distributed within the study area limit, as is also visible in Figure 1b, thus making it challenging to monitor this landslide with conventional PSI techniques.

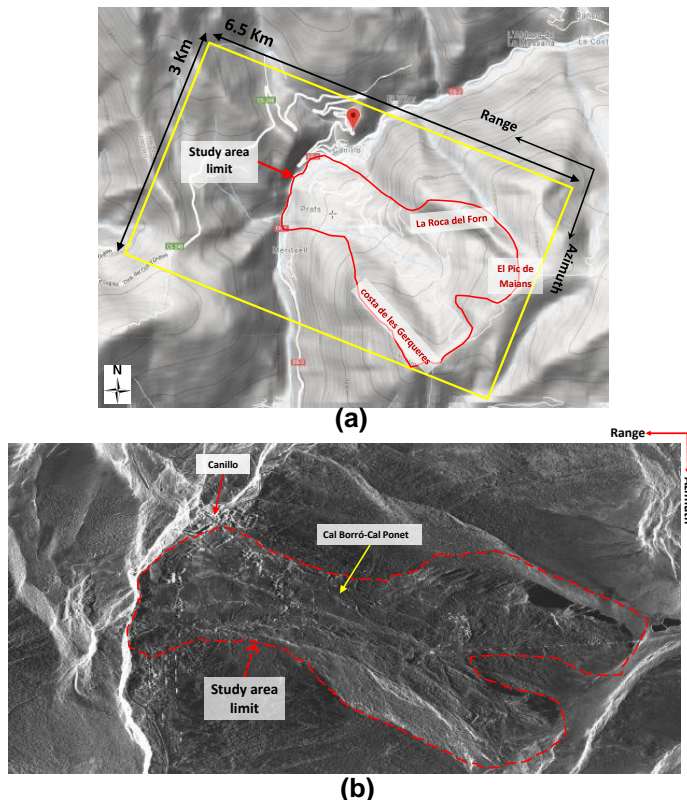


Figure 2. (a) coverage of the TerraSAR-X dataset (i.e., the yellow rectangle) displayed on a topographic map of the area (map from <https://elevationmap.net>); (b) amplitude of an SAR image in radar coordinates (azimuth, slant-range) acquired by the TerraSAR-X sensor in Staring Spotlight mode, and the red line illustrates the boundary of the study area limit.

Table 1. Main parameters of the employed Staring Spotlight TerraSAR-X images. Heading and LOS angles defined clockwise with respect to the north.

Parameter	Value
Acquisition Period	22 July 2014–15 November 2016
Heading Angle	189.8 (degree)
LOS Angle	279.8 (degree)
Incidence Angle	39 (degree)
Azimuth Resolution	0.23 (m)
Slant Range Resolution	0.59 (m)
Wavelength	3.1 (cm)
Revisit Cycle	11 (day)

2.3. GPS Validation Data

The Canillo landslide is monitored with the Global Positioning System (GNSS/GPS) since December 2012. Although several continuous monitoring GPS techniques exist [8], the small rate of displacements justified a discontinuous approach, with yearly field campaigns [7]. A network of 78 GPS points were established at Canillo, covering most of the landslide and the surrounding area as Figure 3 shows. Six points (blue filled triangles in Figure 3) serve as base points to check the stability of the local datum. Once per year, in October, a two day campaign is carried out covering all the control points, spread along the landslide. The GPS method has been the Real Time Kinematic (RTK), with two geodetic-level receivers (Topcon Hiper-Pro, double frequency, double constellation, (Topcon Positioning Systems Inc., Tokyo, Japan)). The final results are the point coordinates in the ETRS89 reference system (Longitude, Latitude and elevation for instance). The estimated accuracy of the resulting coordinate increments is around 1 cm in planimetry and 2 cm in elevation [7].

Three GPS campaigns fit within the study period: October 2014, October 2015 and October 2016. The six base points (E1, E2, E3, E4, E6 and G44 in Figure 3), which are on the assumed stable substrate outside the unstable area, and a total of 72 control points spread over the landslide deposits have been measured. The base points were measured in order to rule out systematic or instrumental errors and thus validate the measures carried out. The control points have been distributed throughout the landslide with the aim of providing a comprehensive overview of its behavior.

The results of the displacement observed at the reference points (points E and G44 in Figure 3), outside the landslide, are within the range of the error and therefore can be considered stable, as expected. Among the 72 GPS control points within the study area limit, 37 are selected for PSI results' validation. The correspondence between GPS points and the PSs has been made with proximity criteria but also discarding any change of geomorphological sub-unit. The difference between GPS and PSI in terms of precision, spatial resolution and temporal resolution is noticeable, but the measured displacement of these selected GPS control points can be used to examine the reliability of the PSI derived ground displacement, as it will be done in Section 4.2.

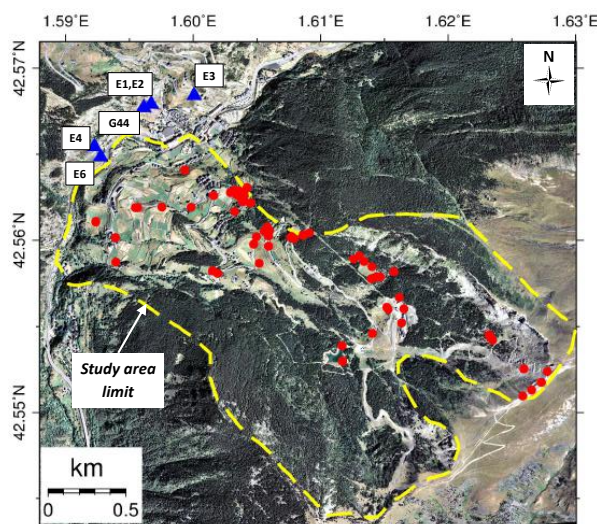


Figure 3. The locations of the GPS measurement points. The filled-in blue triangles and red circles indicate the GPS base points and control points, respectively.

3. Methodology

In this section, the different PSI strategies that will be compared in this paper are introduced. Most of the processing steps are identical for all of them, so the description will be focused on the different PS identification methods used that characterize each strategy.

3.1. Differential SAR Interferometry (DInSAR) Processing

In the conventional strip-map mode, SAR images' azimuth resolution is around half of the azimuth antenna length, which cannot be reduced arbitrarily to improve the resolution without the risk of causing range ambiguities. To overcome this limitation and achieve a higher resolution, the spotlight mode extends the illuminating time of each scatterer by sweeping the azimuth beam backward during imaging [46]. This brings a systematic Doppler centroid drift in the azimuth direction of the focused SAR images.

Prior to the DInSAR processing of the data, the particularities of Staring Spotlight acquisition mode have to be considered during the classical interferometric processing. When performing the image co-registration and common band filtering (if required), all base-banding steps have to consider the azimuth variation of the Doppler spectrum, which is different to the one of the stripmap mode and would require a deramping of the images involved. The details of how to deal with this issue can be found in [37,46]. The other steps of InSAR processing are identical to those of the stripmap case. The spotlight DInSAR processing module, able to work with sliding and staring data, has been implemented in the SUBSOFT-GUI, which is the UPC's DInSAR processing chain based on the Coherent Pixel Technique (CPT) [17,20].

In this study, in order to limit the influence of geometrical and temporal decorrelation on interferograms, we set the interferograms' temporal and spatial baseline thresholds as 365 days and 230 m, respectively. These values have allowed a good interconnection of the images and they act as upper-limits to avoid having interferograms with too long temporal or spatial baselines. The interferograms have been selected using a Delauney triangulation over the SLCs' distribution considering its acquisition time and spatial baselines with respect a master image, as shown in Figure 4. With these restrictions and with the help of an external DEM of the area with 5 m resolution provided by the Government of Andorra, a total of 80 differential interferograms have been generated from the 32 TSX images.

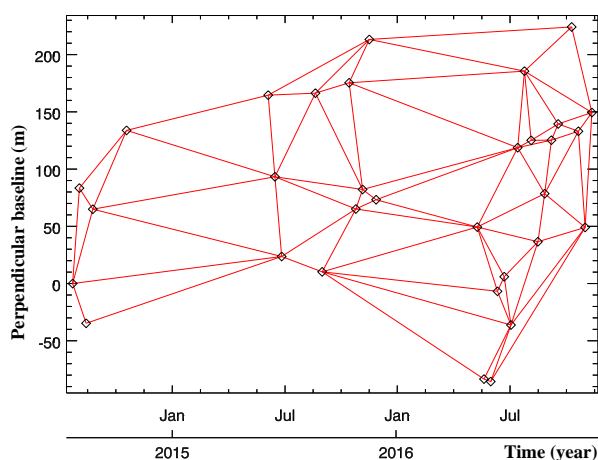


Figure 4. The spatial and temporal baseline distributions of the TerraSAR-X data generated interferograms over the study area. The black diamonds and red lines denote the SAR images and interferograms, respectively.

One of the characteristics of X-band data is that it decorrelates very fast in vegetated areas, but, at the same time, the coherent pixels are able to preserve their phase quality very well over time. In other words, if they are coherent, they keep the coherence well. The main advantage of working with high resolution data is the capability to detect small coherent features embedded in uncorrelated areas. In order to illustrate this, Figure 5 shows two coherence maps obtained from two different interferograms using a multi-look of 5×3 (azimuth \times range). The resolution of the multi-looked interferogram is 1.15×1.77 m. One with a temporal baseline of 11 days and the other with 10 months. The coherence maps look very similar for both cases demonstrating the previous statement.

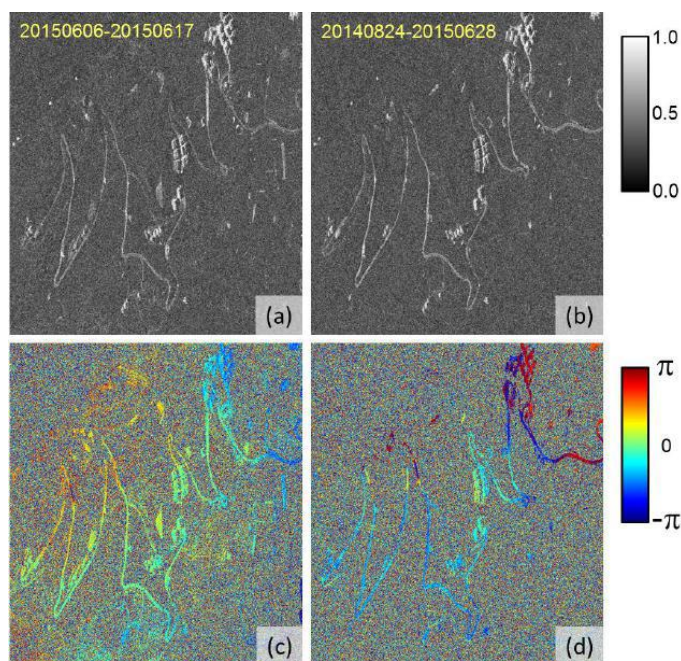


Figure 5. Coherence (a,b) and differential phase (c,d) of two interferograms with temporal baselines of 11 days (a,c) and 10 months (b,d) over the study area. Despite most of the pixels decorrelating very fast, the coherent ones are able preserve their phase quality very well along time.

3.2. Persistent Scatterers Identification

Together with the classical full-resolution pixel selection method (i.e., the amplitude dispersion (D_A) method), another two techniques (the temporal sublook coherence (TSC) and the temporal phase coherence (TPC) methods) have been used to identify pixels with high phase quality, known as PS Candidates (PSCs). As the D_A approach [14] is very well known by the PSI community, we will only introduce briefly the TSC and TPC approaches, which are two pixel selection methods developed by the authors.

3.2.1. PS Candidates Selection by Temporal Sublook Coherence (TSC)

Different from the D_A method, which selects persistent PSs by exploring pixels' amplitude stability, the TSC method intends to identify those pixels that behave like point scatterers in the spectral domain along time [36]. Any target that presents a correlated spectrum in range, azimuth and elevation along time would be identified as PS. In practice, targets usually present a nonuniform azimuth scattering pattern, worsened in the Staring Spotlight case due to the length of the synthetic aperture, and the assumption of correlated spectrum can only be applied in range. This method

presents some advantages. For instance, with this approach, the radiometric calibration of the images is not necessary since amplitude plays no role in the detection and, thus, point-like scatterers that change its amplitude along time can be perfectly selected. An example of the latter case will be highly directive targets whose reflectivity has a strong dependence on the incidence angle. In addition, it was demonstrated in [36] that it is more reliable with reduced sets of images than D_A .

Before TSC estimation, two range sublook (SL) of each SAR image have to be generated. Focused SAR images are usually tapered with a linear window (Hamming, Hanning, Kaiser, etc.) to reduce the impact of the sidelobes. In order to ensure that the two sublooks in which the spectrum will be divided present a symmetrical shape, the original spectrum has to be unweighted to flatten it. Once the range spectrum has been flattened, two sublooks are generated (each one corresponding to one half of the original spectrum) and base banded to the same central frequency to avoid any undesired linear phase term during the later spectral correlation. To reduce once again the sidelobes, each sublook is tapered with a linear window. Finally, the inverse Fourier transform is applied to get both SLs in the spatial domain. A detailed explanation of the whole process is perfectly detailed in [36]. Once the sublooks of all SAR images are obtained, the TSC of any arbitrary pixel (i, j) can be calculated with Equation (1)

$$|\hat{\gamma}_{tmp}(i, j)| = \frac{\left| \sum_{n=1}^{N_{im}} S_1(i, j, n) \cdot S_2^*(i, j, n) \right|}{\sum_{n=1}^{N_{im}} |S_1(i, j, n)|^2 \cdot \sum_{n=1}^{N_{im}} |S_2(i, j, n)|^2}, \tag{1}$$

where S_1 and S_2 are the pixel (i, j) corresponding complex values of the first and second sublook for the acquisition image n , and N_{im} refers to the total number of images. The sketch of the TSC estimation for a generic pixel can be represented by Figure 6.

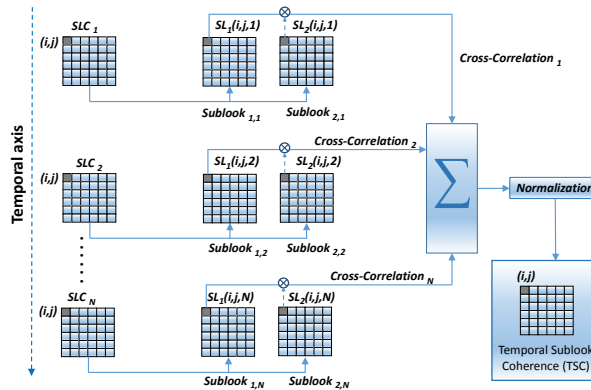


Figure 6. Sketch of the TSC estimation for a generic pixel. From left to right, the Single Look Complex (SLC) images of the dataset, the two sublooks generated from each image, coherence calculation and final TSC [37].

The temporal sublook coherence (TSC) can be regarded as the classical coherence and, similarly, pixels can be selected based on the application of a threshold. High values of TSC would be associated with point-like scatterers. Similarly to the case of classical coherence, relations between the true TSC and the expected one can be established as a function of the number of images employed, as well as the true TSC and the pixel phase standard deviation [36,37]. These relations help to perform the pixel selection based on a phase standard deviation threshold, allowing for using a criterion independent on the number of images. From the phase standard deviation, the corresponding TPC threshold can be

calculated. The selected pixels can then be treated as PSs and processed by the DInSAR algorithm to derive the displacement maps and time-series.

3.2.2. PS Candidates Selection by Temporal Phase Coherence (TPC)

After removing the topographic term using an external DEM, the phase of a differential interferogram can be expressed as Equation (2)

$$\psi = \psi_{def} + \psi_{atm} + \psi_{orb} + \psi_{\xi_{DEM}} + \psi_{noise}, \quad (2)$$

where ψ_{def} , ψ_{atm} and ψ_{orb} denote the phase terms introduced by displacement along the LOS direction, atmospheric artifacts (atmospheric phase screen, APS) and SAR satellite orbit indeterminations. $\psi_{\xi_{DEM}}$ is the residual phase due to the DEM error, and ψ_{noise} is the noise phase term. This latter term can be assumed to present a random behaviour in the neighbourhood of a given pixel while the other can be assumed to be deterministic. Thus, the noise phase term can be used as a metric of pixel's phase quality. The temporal phase coherence (TPC) can be used to evaluate the quality of a pixel from the behaviour of this phase noise along the stack of interferograms. TPC can be estimated based on ψ_{noise} from all generated interferograms, as Equation (3) shows

$$\gamma_{TPC} = \frac{1}{M} \cdot \left| \sum_{i=1}^M e^{j\psi_{noise,i}} \right|, \quad (3)$$

where M is the number of interferograms and $\psi_{noise,i}$ is the noise phase term of the i th interferogram.

To obtain for each interferogram the noise phase term of a pixel, it is necessary to estimate the deterministic terms. In order to do that, the neighbouring pixels will be used assuming, in theory, a spatial low-pass behaviour of all deterministic terms in the vicinity of the pixel whose TPC is being estimated, a.k.a the central pixel. The phase of the neighbouring pixels is estimated by averaging their complex values, but excluding the central pixel, and then calculating the argument of this complex number. With this approach, similarly to the classical multi-looking in interferometry, the pixels' amplitude is used to give more significance to those pixels with higher amplitude in front of those with lower values that, in principle, can be expected to be noisier and less reliable. The first three terms of Equation (2) can be assumed to be spatially low-pass. Indeed, APS, orbital residues and the phase offset of the interferogram perfectly fulfill this condition while, for the deformation, it would be an acceptable approximation. Then, subtracting the neighbouring phase from the central phase gives Equation (4)

$$\psi^{central} - \psi^{neigh} \equiv \psi^{dif} = \psi_{\xi_{DEM}}^{dif} + \psi_{noise}^{dif}, \quad (4)$$

where $\psi_{\xi_{DEM}}^{dif} = \psi_{\xi_{DEM}}^{central} - \psi_{\xi_{DEM}}^{neigh}$ and $\psi_{noise}^{dif} = \psi_{noise}^{central} - \psi_{noise}^{neigh}$. Thus, the terms have been grouped in deterministic along the interferometric stack, $\psi_{\xi_{DEM}}^{dif}$, and random, ψ_{noise}^{dif} . As (4) shows, the estimation of the noise phase of the central pixel, i.e., $\psi_{noise}^{central}$, would be affected by the deterministic terms. The averaging would reduce the noise term of the neighbouring pixels, ψ_{noise}^{neigh} . Thus, we can assume than $\psi_{noise}^{central} \approx \psi_{noise}^{dif}$. Thus, by subtracting the deterministic term $\psi_{\xi_{DEM}}^{dif}$ from ψ^{dif} , the noise phase of the central pixel can be estimated. In the practical implementation, all phase operations are obviously done in the complex domain.

The phases due to DEM errors ($\varepsilon_{DEM}^{central}$ and $\varepsilon_{DEM}^{neigh}$) of the central and neighboring pixels can be rewritten as Equations (5) and (6), respectively:

$$\psi_{\xi_{DEM}}^{central} = \frac{4\pi}{\lambda} \cdot \frac{B_n}{R_0 \cdot \sin(\theta_0)} \cdot \varepsilon_{DEM}^{central}, \quad (5)$$

$$\psi_{\xi_{DEM}}^{neigh} = \frac{4\pi}{\lambda} \cdot \frac{B_n}{R_0 \cdot \sin(\theta_0)} \cdot \varepsilon_{DEM}^{neigh}, \quad (6)$$

where λ , B_n , R_0 and θ_0 are the wavelength, the perpendicular baseline, the absolute range distance in the LOS direction between the sensor and the target and the incidence angle, respectively. Then, we can derive $\psi_{\xi_{DEM}}^{dif}$ as (7)

$$\psi_{\xi_{DEM}}^{dif} = \frac{4\pi}{\lambda} \cdot \frac{B_n}{R_0 \cdot \sin(\theta_0)} \cdot \Delta\varepsilon_{DEM}, \quad (7)$$

where $\Delta\varepsilon_{DEM} = \varepsilon_{DEM}^{central} - \varepsilon_{DEM}^{neigh}$ is the difference of DEM errors between the central and the averaged error of the neighboring pixels. We use Equation (8) to estimate each pixel's $\Delta\varepsilon_{DEM}$ and then the $\psi_{\xi_{DEM}}^{dif}$ is calculated by Equation (7):

$$\arg \max_{\Delta\varepsilon_{DEM}} \{ \gamma_{TPC} = \frac{1}{M} \cdot \left| \sum_{i=1}^M e^{j \cdot \psi_i^{dif} - j \cdot \psi_{\xi_{DEM}^j}^{dif}} \right| \}. \quad (8)$$

Until now, $\psi_{\xi_{DEM}}^{dif}$ has been estimated and then $\psi_{noise}^{central}$ can be derived by Equation (4) under the assumption that $\psi_{noise}^{central} \approx \psi_{noise}^{dif}$. All pixels' noise phase terms of all the interferograms can be estimated by this way and then the TPC can be calculated by Equation (3).

TPC provides a temporal coherence of each pixel and fixing a threshold can perform the identification of PSCs. As in the case of classical coherence or the TSC, a relationship between TPC and the phase standard can be established in order to select a threshold independent on the number of images and interferograms. The derivation of these relations has been discussed in detail in [38].

3.3. Linear and Nonlinear (Time-Series) Displacement Estimation

The linear and nonlinear displacement terms and the DEM error can be estimated by using UPC's ground motion detection software SUBSOFT-GUI (UPC, Barcelona, Spain). SUBSOFT-GUI is a user-friendly software package for PSI processing. It allows for performing all required steps, starting from the image co-registration, differential interferograms generation and filtering, pixel selection and deformation time-series extraction. The software uses a Graphical User Interface (GUI) and most of the steps have been automatized, which facilitates the processing of any dataset. The detailed procedures of the linear and nonlinear blocks in SUBSOFT-GUI can be found by referring to [17,20]. Three independent processes, based on the same set of differential interferograms but with three different PS selection strategies (D_A , TSC and TPC approaches), have been carried out to compare the performance of each pixel selection technique under similar conditions. For each strategy, the measured parameter can be related with a phase standard deviation as shown in Figure 7.

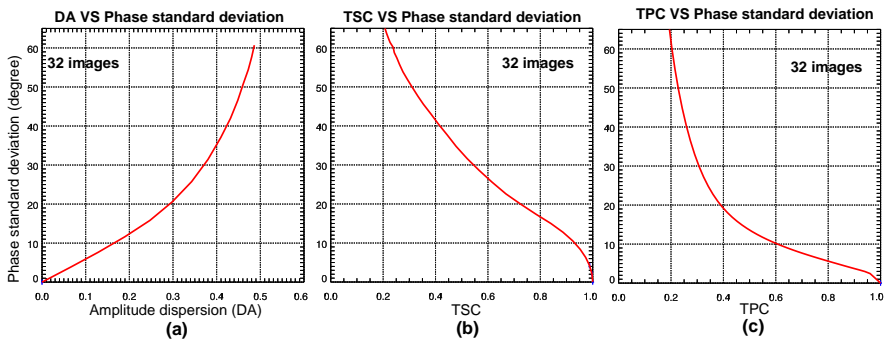


Figure 7. Standard deviation of the interferometric phase as a function of (a) D_A , (b) TSC and (c) TPC for the 32 images set.

The comparison of the different strategies is always a difficult task as there are many parameters that can be adjusted. In this case, the key point that makes the difference is the capability of the different strategies to select PSs. The larger the number, the better performance of the PSI processing, as it allows a better connection of the different areas and reduces the chances of having isolated clusters of PSs. It is also true that the three processes could have been optimized with a fine-tuning of the processing parameters, but, in practice, it is expected that the possible small variations on the final results would not be enough to modify the conclusions.

3.4. Atmospheric Artefacts

InSAR observations are usually plagued by propagation delays, which are also known as atmosphere phase screen (APS). As the atmosphere properties (temperature, pressure, and relative humidity that set the refractive index) between radar platform and the ground targets vary spatially and temporally, the phase delays vary from one day to another. For microwaves, it is well known that propagation delays have two major sources: tropospheric terms and ionosphere effects. At X-band, ionosphere is almost invisible and so the only significant source is the troposphere [26,47]. The atmospheric propagation delay in interferograms can be categorized into vertical stratification and turbulence mixing [26]. While the latter can be compensated, thanks to its random behaviour in time and correlated behaviour in space, with a set of temporal and spatial filters during data processing [14,18,20], the former can be much more difficult. Stratification is prone to occurring in areas with steep topography and the APS appears to be strongly correlated with the elevation. If not properly compensated, APS can be misinterpreted as topography or displacement. Different strategies can be used to characterize and compensate the stratified APS, for instance with models following a linear or quadratic phase-elevation relationship [25,27–29].

The time of the pass of the satellite for the TSX data acquisitions was early in the morning, around 6:03 a.m. UTC (8:03 a.m. in local summer time and 7:03 a.m. in local winter time). At this time of the day, the atmosphere is very stable, compared with the strong fluctuations that can be observed during the day, and stratified APS has not been observed in the dataset.

4. Results and Discussion

4.1. Line-of-Sight (LOS) Monitoring Results

The LOS displacement rate maps derived by the three methods (i.e., the D_A , TSC and TPC) are shown in Figure 8a–c, respectively. To make a fair comparison, the pixel selection thresholds for all the three methods were established based on a phase standard deviation of 15° . Using the plots shown in Figure 7, the corresponding thresholds for each strategy can be selected. Similar displacement trends have been detected by all of them, and the maximum displacement velocity reaches up to -3.5 cm/year (the minus sign means movement away from the satellite, i.e., downslope motion due to the landslide orientation). Within the landslide limits, there are mainly three large displacement subareas (indicated by the red rectangles in Figure 8a–c), located at the El Pic de Maians (subarea A), costa de les Gerqueres (subarea B) and Cal Borró-Cal Ponet (subarea C), respectively. These three subareas' locations and displacement patterns are coincident with the monitoring results obtained with another dataset in 2011 [37]. The dataset consisted on Sliding-spotlight TerraSAR and GB-SAR images, and data from inclinometers deployed in the landslide, all acquired from October 2010 until October 2011. Previous results have confirmed that the location and evolution of the landslide body have not changed significantly during the recent years. This fact is in good agreement with the geological expectations.

Among the three pixel selection methods, D_A and TSC select pixels that behave as point scatterers while TPC can work on both point and distributed scatterers (DSs). Since there are many DS pixels (e.g., the road) in the study area, TPC obtains a much higher density of measurement pixels (MP) than D_A and TSC approaches.

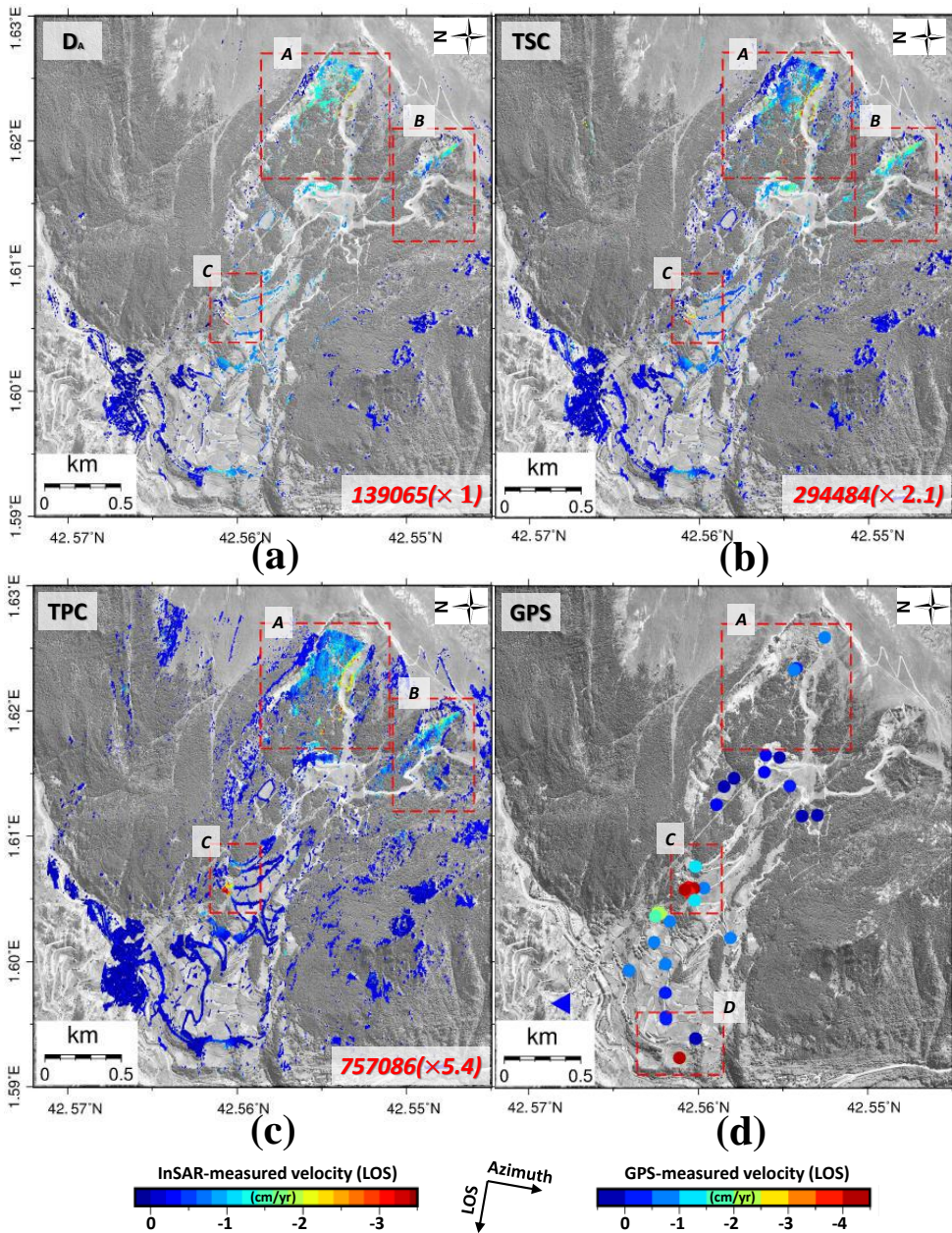


Figure 8. LOS displacement velocity maps derived by (a) D_A , (b) TSC, (c) TPC and (d) GPS approaches, respectively. The filled blue triangle in (d), i.e., E1, indicates the location of the GPS base point. GPS displacements have been projected to LOS. The red rectangles highlight the areas zoomed in Figure 9. The red numbers at the right bottom corner of (a–c) represent the amount of valid pixels obtained by each method.

Notice in Figure 8 how well the TPC method has identified those pixels along the downhill road, while the other two have just selected a reduced set of them. At the same time, the TSC method obtains more PSs than D_A . This can be explained by the fact that the D_A method is very sensitive to the amplitude changes that highly directive scatterers produce when the local incidence angle changes from image to image. Specifically, the number of PSs obtained by TPC method is 757,086, the counterparts of TSC and D_A methods are 139,065 and 294,484, respectively. The improvement of the TPC and TSC methods on D_A is around $\times 5.4$ and $\times 2.1$, respectively. The TPC method thus has the best performance in terms of PSs' density.

To better analyse the details of the landslide, the three subareas' monitoring results have been enlarged and plotted in Figure 9. From column A (results of the subarea A), we can find that the displacement velocities obtained by D_A (-1.3 cm/yr) are greater than those of TSC and TPC (-0.6 cm/yr) at the locations highlighted by the red ellipses. Similar differences can be observed between the TPC derived results and the other two methods within the subarea C (along the downhill road). These displacement velocities' differences are mainly caused by the sparsity of selected pixels that reduces the number of connections of D_A (Figure 9a,c) or TSC (Figure 9f) during the linear displacement estimation. Different areas interconnected by low-quality links can lead to small offsets in the velocity results. The sparser the local connections, the more easily the estimated displacement can be affected by nearby lower quality pixels and APS. Therefore, the high estimated displacement velocities in Figure 9a,c,f are mostly due to the low densities of PSs within these local areas.

As Figure 9g–i shows, thanks to the super high resolution (SHR) of the images and TPC's good performance on pixel selection, the displacement details of the different landslide units are well detected. For instance, more pixels have been selected along the narrow paths (around 1 m in width), as highlighted by red ellipses in Figure 9i. Benefiting from this high density of PSs, the displacement boundaries (illustrated by the yellow dashed lines in Figure 9i) can be clearly determined by the TPC approach in subarea C. These boundaries can hardly be seen from the results of the other two methods, as shown in Figure 9c,f.

Besides the displacement results, PSI techniques can also obtain the DEM error of the selected pixels with respect to the reference DEM used. The inclusion of the retrieved DEM error on the geocoding of the final results largely improves the geolocation quality of the displacement maps. Figure 10 shows some interesting examples that illustrate the capabilities of SHR TSX data to retrieve the vertical distribution of scatterers in manmade structures. The examples shown have been obtained from the TPC processing. Figure 10a shows a communications tower located in Canillo. The vertical distribution of scatterers perfectly follows the tower's structure as the picture validates. It is also interesting, looking at the GoogleEarth image, to compare the distribution of scatterers with the shadow of the tower projected over ground. Figure 10b and c show a couple of chairlifts from the Grandvalira ski station. Once again, the vertical distribution of scatterers perfectly follows the metallic structure, as the pictures and projected shadows demonstrate. Finally, Figure 10d shows a couple of high voltage towers. The good performance of the vertical location of the scatterers, thanks to the inclusion of the calculated DEM error on the geocoding process, can also be used as proof of the reliability of the displacement velocity maps obtained. Both velocity and DEM error have been calculated simultaneously when adjusting the linear model to the interferometric data [17,20].

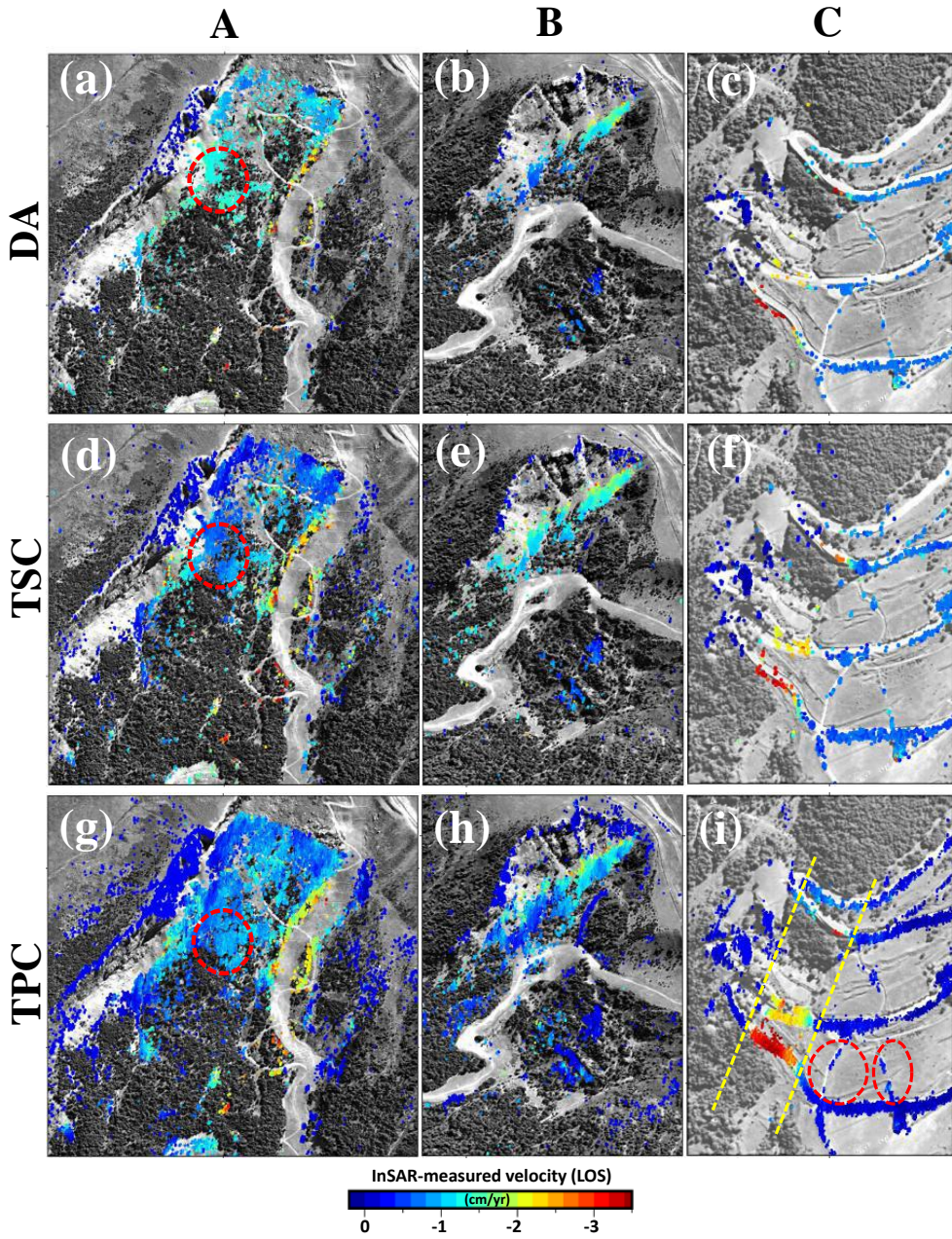


Figure 9. The close-up of the three subareas limited by red rectangles in Figure 8a–c. (a–c) are the results of the D_A method, (d–f) obtained by the TSC method and (g–i) obtained by the TPC method. Red ellipses highlight areas commented in Section 4.1. Yellow dashed lines highlight the edges of the slide.

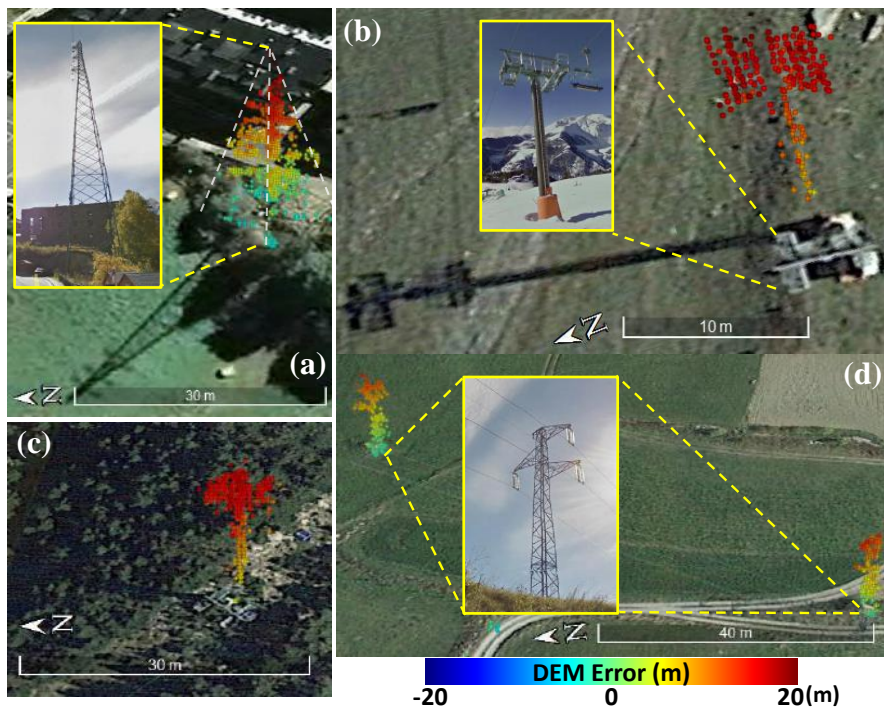


Figure 10. SHR TerraSAR-X data derived DEM errors at the locations of some manmade structures in the study area by the TPC method. (a) communications tower, (b,c) chairlifts towers and (d) high voltage towers. PSs have been geocoded over a GoogleEarth image using the retrieved DEM error.

4.2. Comparison with GPS Measurements

The displacement velocities of the 37 GPS control points introduced in Section 2.3 have been projected to the LOS direction [48,49] to compare them with the DInSAR results, as shown in Figure 8d. In subarea A of Figure 8d, a small displacement with a velocity around -1 cm/yr has been detected. In the subarea C, significant movement with velocity around -4 cm/yr has been monitored by the GPS. In the subareas A and C, the GPS and PSI measured displacement velocities are consistent with each other. Unfortunately, no GPS points were available in the subarea B for comparison. On the contrary, large displacements have been recorded by the GPS within the subarea D (highlighted by the red rectangle in Figure 8d), where there are no counterpart PSI pixels in its near vicinity. However, the further neighboring PSI pixels present LOS velocities about -1.5 cm/yr, providing evidence of the agreement of the GPS and PSI results also in this subarea.

To summarize the comparison, a scatter plot with the GPS and PSI derived displacements is shown in Figure 11. In this plot, the PSI displacements are estimated by averaging those of the neighbouring pixels of the related GPS measurement point (less than 50 m apart). In addition, they have been determined from the displacement time-series taking the overall two year displacement from October 2014 to October 2016, as the GPS date campaigns. As Figure 11 reveals, the GPS and PSI displacements follow the same trends and present a correlation coefficient of $R^2 = 0.90$. For GPS measurement points with noticeable displacement (highlighted by the red ellipse in Figure 11), their surrounding PSI pixels show large displacements as well. Meanwhile, for those stable GPS measurement points (limited by the blue rectangle), with displacements between -2 to 2 cm, their corresponding PSI displacements are also within this range.

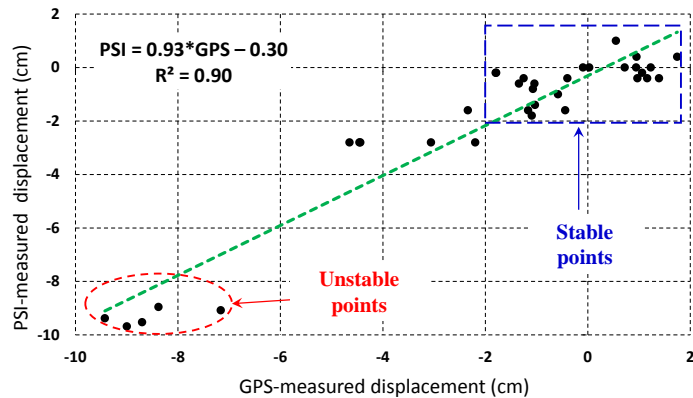


Figure 11. Comparison of PSI and GPS derived displacements (October 2014 to October 2016).

4.3. Down-Slope (DSL) Direction Displacement Monitoring Result

The ground motion derived by DInSAR is along the LOS direction, but it is usually projected to the down-slope (DSL) direction to better interpret the landslide displacement. The detailed LOS to DSL direction projection method can be found by referring to [12,24]. As it is out of the scope of this paper, we do not describe it here. We projected the TPC method's ground displacement velocities to the DSL direction, and the result is shown by Figure 12. It has to be noted that, when doing the projection, only those PSs with projection factors smaller than 3 have been preserved to avoid artificially amplifying displacement values and noise when the slope is gentle. Thanks to the relative orientation of the landslide with respect the satellite path, most of the projection factors within this study area are small. Thus, the majority of PSs have been preserved, and the displacement patterns along the LOS and DSL directions are similar (e.g., the neighboring area of P1). Except for a small set of pixels nearby point P4 in Figure 12, the displacement velocities of the previous three displacement subareas (in Figure 8c) have not been heavily amplified via the projection.

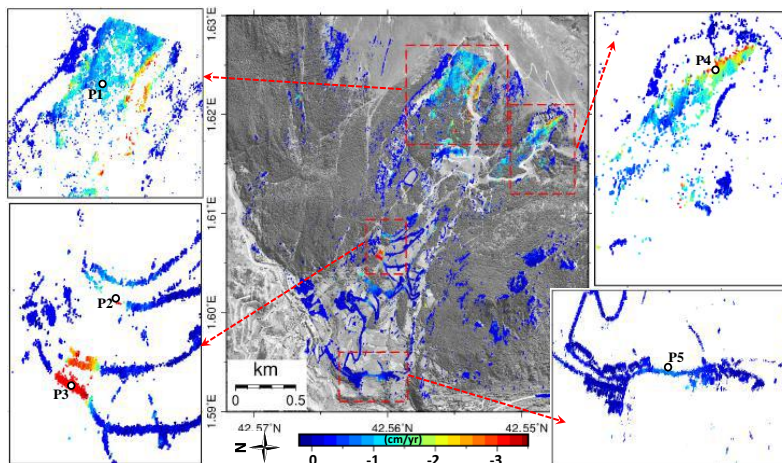


Figure 12. Down-slope displacement velocity map derived by the TPC method. Estimated displacement velocities within subareas A, B, C and D in Figure 8 have been enlarged for a better visualization with a white background. The locations of points P1–P5 in the subareas, which are further analyzed in the text, have also been indicated.

Besides the subareas A, B and C in Figure 8, in Figure 12, we have highlighted another subarea, which is located at the foot of the hill. In this subarea, noticeable displacement has been identified at the location of P5, which may be caused by the extrusion of the landslide main body moving towards the downhill direction.

4.4. PSI Time-Series

To investigate the temporal evolution of the Canillo landslide, the DSL time-series displacement results obtained by the TPC method at two different PSs (P2 and P3 in Figure 12) have been plotted in Figure 13. The displacements observed for both PSs are exhibiting considerable nonlinear components, presenting some acceleration and deceleration periods within each year. From the two PSs' 2016 displacement time-series (Figure 13b,d), we can find that the stable periods start at the beginning of July and end at the middle of August. These periods are coincident with the trend of Canillo averaged monthly precipitation, where the lowest precipitation is in July with an average of 79 mm, as Figure 13e shows. This indicates that the movements of the landslide have some seasonal patterns, which are correlated with the amount of precipitation.

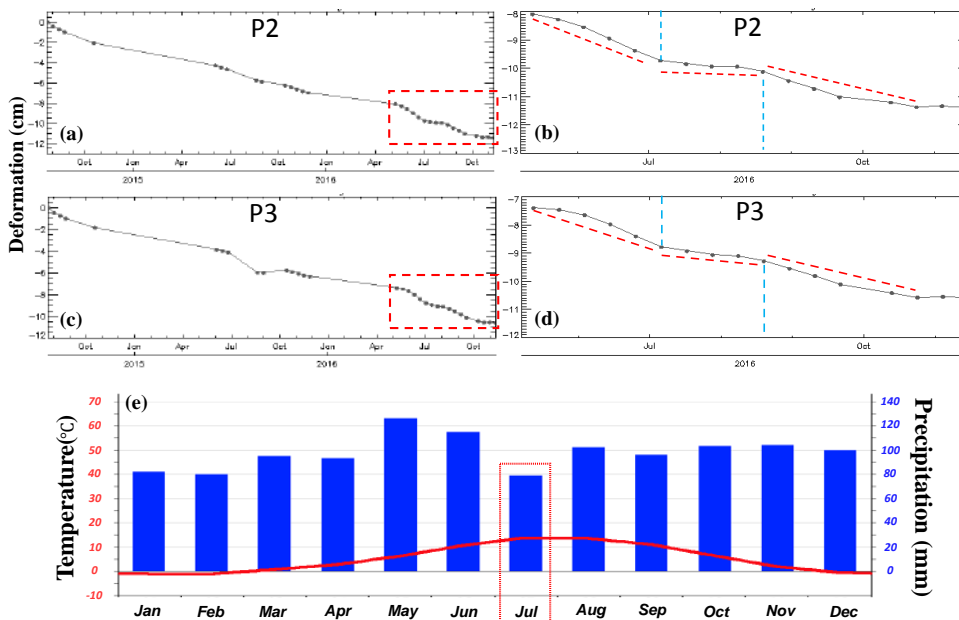


Figure 13. TPC method derived down-slope time-series displacement of P2 and P3, Figure 12. (a,c) cover the period 22 July 2014–15 November 2016 whereas (b,d) are a close-up of the dashed red rectangles inside (a,c), covering the period May 2016–November 2016 approximately. The red lines indicate the different deformation trends while the vertical blue ones the location of trend changes; (e) is the averaged monthly temperature (red line) and precipitation (blue bars) of Canillo (CLIMATE-DATA.ORG, <https://en.climate-data.org/location/13728/>); July has been highlighted with a red rectangle.

5. Comparison with Low-Resolution Data

Sentinel-1A data of the study area have been processed with D_A and TPC methods to highlight the advantages of the SHR data in regional-scale landslide monitoring. TSC has not been included as it provides similar results than TPC. Sentinel-1A images have resolutions of 14 and 2.5 m in azimuth and range directions, respectively. Fourteen Sentinel-1A SAR images acquired from the 11 May 2016

to 19 November 2016 have been employed to generate 33 interferograms. In the pixel selection step, the same phase standard deviation threshold (15°) as with TSX data has been used. The displacement velocity maps obtained using the two PSI strategies, D_A and TPC, are shown in Figure 14.

Similarly to the case of TSX data, TPC is able to obtain much more PSs than D_A ($\times 4.0$), and the displacement trends derived are similar to those of TSX but less detailed. For both methods, their PSs' densities have decreased dramatically compared with the TSX data case. Specifically, for D_A and TPC methods, the numbers of PSs are $\times 146$ and $\times 197$ less w.r.t. that of the TSX case. This significant reduction of the PSs' density is mainly due to two reasons that are closely related. In addition to the logical reduction due to the coarse resolution of Sentinel-1A data, there is also the fact that many small PSs surrounded by decorrelated pixels that were detected with SHR data are now mixed all together due to the worse resolution and, consequently, not detected.

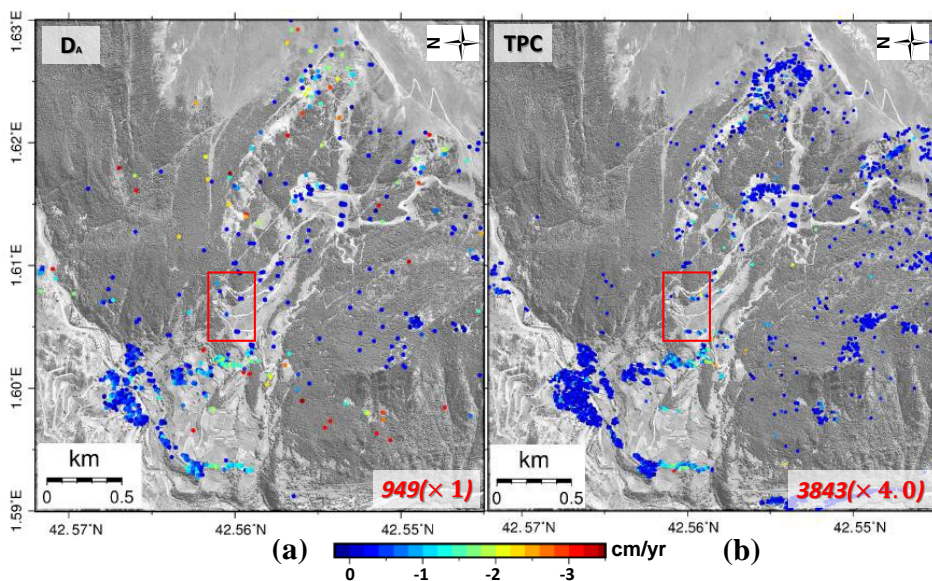


Figure 14. The LOS ground displacement velocity maps derived by (a) D_A and (b) TPC methods with Sentinel-1A SAR images.

The Sentinel-1A data monitoring results of the Cal Borró-Cal Ponet section (subarea C in Figure 8 and where the strongest displacement has been detected) have been highlighted with a red rectangle in Figure 14. In this subsection, the displacement clearly detected with TSX data does not appear in the Sentinel-1A results with none of the pixel selection methods. A detailed view of Cal Borró is shown in Figure 15. Similarly, Figure 14 shows no noticeable displacement in any of the other two subareas (subareas A and B in Figure 8c). However, the small displacement at the base of the landslide is detected with both PSI strategies and agrees with the results of SHR data. Moreover, the sparse distribution of PSs, which can be poorly interconnected, allows the appearance of some outliers, pixels whose velocities are clearly erroneous, scattered along the image. The presence of outliers is more noticeable on the D_A results in the form of isolated red points, those with the highest velocities.

To conclude, for regional-scale landslide monitoring, the TSX SHR SAR images have the advantage of obtaining more detailed monitoring results with better reliability compared with those of lower resolution sensors.

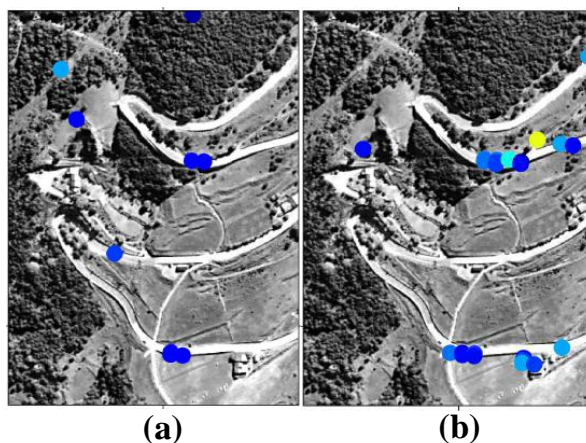


Figure 15. The LOS ground displacement velocity maps, Sentinel-1A SAR images. Enlargement of the red rectangles inside Figure 14. (a) D_A method; (b) TPC method. The color scale for the displacements is the same as that in Figure 14.

6. Conclusions

In this paper, the ability of super high-spatial resolution (SHR) SAR images together with advanced PS selection strategies for regional-scale landslide monitoring in a challenging area has been studied. Thirty-two SHR TerraSAR-X (TSX) images (July 2014 to October 2016), with resolutions of 0.23 and 0.59 m in azimuth and range directions, have been employed to monitor the Canillo landslide (Andorra) by using PSI techniques with three different pixel selection methods.

This study has demonstrated that improving the number of high-quality pixels for its later PSI processing results of crucial importance in landslide monitoring in natural environments. Under the application point of view, to the authors' knowledge, it is one of the first times when such a high density of PS has been obtained in mountainous areas. SHR SAR data jointly with advanced full-resolution PSI strategies allow the achievement of a more robust network of PS (improving the linear estimation without propagation errors and the reliable estimation of APS) and thus favors the reliable estimation of displacement maps in a major number of points inside a landslide. This is a general conclusion that does not depend on the landslide. A different issue is if the particularities of a given landslide (orientation, type of vegetation coverage, local topography, snow episodes, etc.) made it unsuitable for PSI monitoring. Similarly, well-established interferometric techniques for DEM generation fail on forested areas. It is clear that the particular characteristics of the scenario may limit the application of the technique.

The landslide's overall displacement patterns observed by the three methods in El Forn de Canillo are similar. Three main subareas with noticeable displacement have been detected, which are similar to those obtained in previous PSI monitoring results. This indicates that the evolution of the landslide main body did not change significantly during recent years. The PSI measured displacement rates have been compared with GPS measurements of the same period, and they are both in good agreement. It is worth highlighting the higher information/resolution of the PSI techniques in comparison with the GPS low point density, as it can be appreciated in Figure 8. Although already highlighted in the literature, in the Canillo Landslide, the PSI capability for detecting incipient movements in zones not previously surveyed by the geological engineering specialists has been verified (as the subarea costa de les Gerqueres, red rectangle B in Figure 8). The displacement time-series of two significant pixels are characterized by considerable nonlinear components, exhibiting some acceleration and stabilization periods within each year. These periods can be correlated with the averaged monthly precipitation

amounts, revealing the important influence of rain/snow melting episodes on the development of this landslide.

SHR SAR data initially designed for improving monitoring capabilities over man-made structures, such as buildings, bridges, railways or highways, have also demonstrated an outstanding performance over natural reflectors, such as outcrops or exposed rocks with the proper PSs selection strategy. Indeed, this improvement in terms of density allows a better characterization and delineation of complex landslides. Among the three full-resolution PSC selection strategies, the advanced ones (i.e., the TSC and TPC) are able to obtain much more valid PSs than the classical D_A method. The TPC method presents the best performance. Thanks to these huge amount of PSs, the displacement details of the regional-scale landslides can be characterized with better precision when combining the TPC method with SHR TSX data. Compared with the lower-spatial resolution SAR data (Sentinel-1A in this study), SHR data can better characterize the landslide, particularly if the different subareas are small.

The results of this work show that the density of valid PSs can be greatly enhanced by using the TPC method together with SHR SAR images. Thus, they can together be used as a powerful tool for detailed landslide monitoring in difficult areas.

Author Contributions: F.Z., J.J.M. and R.I. developed the methodologies and designed the experiments; F.Z. performed the experiments; J.J.M., J.A.G. and J.C. analyzed and validated the results.

Acknowledgments: This research work has been supported by the China Scholarship Council (Grant 201606420041), by the Spanish Ministry of Economy, Industry and Competitiveness (MINECO), the State Research Agency (AEI) and the European Funds for Regional Development (EFRD) under project TEC2017-85244-C2-1-P and by the National Natural Science Foundation of China (Grant 51574221). CommSensLab is Unidad de Excelencia Maria de Maeztu MDM-2016-0600 financed by the Agencia Estatal de Investigación, Spain. TerraSAR-X data were provided by the German Aerospace Center (DLR) in the scope of the project GEO2468. Sentinel-1A data were provided by the European Space Agency (ESA). Some figures were prepared using the public domain GMT software (Wessel and Smith, 1998).

Conflicts of Interest: The authors declare no conflict of interest.

References

- Dunncliff, J.; Green, G.E. *Geotechnical Instrumentation for Monitoring Field Performance*; John Wiley & Sons: Hoboken, NJ, USA, 1993.
- Pinyol, N.M.; Alonso, E.E.; Corominas, J.; Moya, J. Canelles landslide: Modelling rapid drawdown and fast potential sliding. *Landslides* **2012**, *9*, 33–51. [[CrossRef](#)]
- Ramesh, M.V. Design, development, and deployment of a wireless sensor network for detection of landslides. *Ad Hoc Netw.* **2014**, *13*, 2–18. [[CrossRef](#)]
- Uhlemann, S.; Smith, A.; Chambers, J.; Dixon, N.; Dijkstra, T.; Haslam, E.; Meldrum, P.; Merritt, A.; Gunn, D.; Mackay, J. Assessment of ground-based monitoring techniques applied to landslide investigations. *Geomorphology* **2016**, *253*, 438–451. [[CrossRef](#)]
- Zhang, Y.; Tang, H.; Li, C.; Lu, G.; Cai, Y.; Zhang, J.; Tan, F. Design and Testing of a Flexible Inclinometer Probe for Model Tests of Landslide Deep Displacement Measurement. *Sensors* **2018**, *18*, 224. [[CrossRef](#)] [[PubMed](#)]
- Calcaterra, S.; Cesi, C.; Di Maio, C.; Gambino, P.; Merli, K.; Vallario, M.; Vassallo, R. Surface displacements of two landslides evaluated by GPS and inclinometer systems: A case study in Southern Apennines, Italy. *Nat. Hazards* **2012**, *61*, 257–266. [[CrossRef](#)]
- Gili, J.A.; Corominas, J.; Rius, J. Using Global Positioning System techniques in landslide monitoring. *Eng. Geol.* **2000**, *55*, 167–192. [[CrossRef](#)]
- Malet, J.P.; Maquaire, O.; Calais, E. The use of Global Positioning System techniques for the continuous monitoring of landslides: Application to the Super-Sauze earthflow (Alpes-de-Haute-Provence, France). *Geomorphology* **2002**, *43*, 33–54. [[CrossRef](#)]
- Colesanti, C.; Wasowski, J. Investigating landslides with space-borne Synthetic Aperture Radar (SAR) interferometry. *Eng. Geol.* **2006**, *88*, 173–199. [[CrossRef](#)]
- Wasowski, J.; Bovenga, F. Investigating landslides and unstable slopes with satellite Multi Temporal Interferometry: Current issues and future perspectives. *Eng. Geol.* **2014**, *174*, 103–138. [[CrossRef](#)]

11. Bovenga, F.; Wasowski, J.; Nitti, D.; Nutricato, R.; Chiaradia, M. Using COSMO/SkyMed X-band and ENVISAT C-band SAR interferometry for landslides analysis. *Remote Sens. Environ.* **2012**, *119*, 272–285. [[CrossRef](#)]
12. Hu, X.; Wang, T.; Pierson, T.C.; Lu, Z.; Kim, J.; Cecere, T.H. Detecting seasonal landslide movement within the Cascade landslide complex (Washington) using time-series SAR imagery. *Remote Sens. Environ.* **2016**, *187*, 49–61. [[CrossRef](#)]
13. Confuorto, P.; Di Martire, D.; Centolanza, G.; Iglesias, R.; Mallorqui, J.J.; Novellino, A.; Plank, S.; Ramondini, M.; Thuro, K.; Calcaterra, D. Post-failure evolution analysis of a rainfall-triggered landslide by multi-temporal interferometry SAR approaches integrated with geotechnical analysis. *Remote Sens. Environ.* **2017**, *188*, 51–72. [[CrossRef](#)]
14. Ferretti, A.; Prati, C.; Rocca, F. Permanent scatterers in SAR interferometry. *IEEE Trans. Geosci. Remote Sens.* **2001**, *39*, 8–20. [[CrossRef](#)]
15. Ferretti, A.; Fumagalli, A.; Novali, F.; Prati, C.; Rocca, F.; Rucci, A. A new algorithm for processing interferometric data-stacks: SqueeSAR. *IEEE Trans. Geosci. Remote Sens.* **2011**, *49*, 3460–3470. [[CrossRef](#)]
16. Berardino, P.; Fornaro, G.; Lanari, R.; Sansosti, E. A new algorithm for surface deformation monitoring based on small baseline differential SAR interferograms. *IEEE Trans. Geosci. Remote Sens.* **2002**, *40*, 2375–2383. [[CrossRef](#)]
17. Mora, O.; Mallorqui, J.J.; Broquetas, A. Linear and nonlinear terrain deformation maps from a reduced set of interferometric SAR images. *IEEE Trans. Geosci. Remote Sens.* **2003**, *41*, 2243–2253. [[CrossRef](#)]
18. Lanari, R.; Mora, O.; Manunta, M.; Mallorquí, J.J.; Berardino, P.; Sansosti, E. A small-baseline approach for investigating deformations on full-resolution differential SAR interferograms. *IEEE Tran. Geosci. Remote Sens.* **2004**, *42*, 1377–1386. [[CrossRef](#)]
19. Hooper, A.; Zebker, H.; Segall, P.; Kampes, B. A new method for measuring deformation on volcanoes and other natural terrains using InSAR persistent scatterers. *Geophys. Res. Lett.* **2004**, *31*, doi:10.1029/2004GL021737.
20. Blanco-Sanchez, P.; Mallorquí, J.J.; Duque, S.; Monells, D. The coherent pixels technique (CPT): An advanced DInSAR technique for nonlinear deformation monitoring. *Pure Appl. Geophys.* **2008**, *165*, 1167–1193. [[CrossRef](#)]
21. Iglesias, R.; Monells, D.; Fabregas, X.; Mallorqui, J.J.; Aguasca, A.; Lopez-Martinez, C. Phase quality optimization in polarimetric differential SAR interferometry. *IEEE Trans. Geosci. Remote Sens.* **2014**, *52*, 2875–2888. [[CrossRef](#)]
22. Cruden, D.M.; Varnes, D.J. Landslide types and processes. In *Landslides: Investigation and Mitigation*; Turner, A., Schuster, R., Eds.; Transportation Research Board, US National Research Council: Washington, DC, USA, 1996; Volume 247, Chapter 3; pp. 36–75.
23. Hungr, O.; Leroueil, S.; Picarelli, L. The Varnes classification of landslide types, an update. *Landslides* **2014**, *11*, 167–194. [[CrossRef](#)]
24. Iglesias, R. High-Resolution Space-Borne and Ground-Based SAR Persistent Scatterer Interferometry for Landslide Monitoring. Ph.D. Thesis, Universitat Politècnica de Catalunya, Barcelona, Spain, 2015.
25. Beauducel, F.; Briole, P.; Froger, J.L. Volcano-wide fringes in ERS synthetic aperture radar interferograms of Etna (1992–1998): Deformation or tropospheric effect? *J. Geophys. Res. Solid Earth* **2000**, *105*, 16391–16402. [[CrossRef](#)]
26. Hanssen, R.F. *Radar Interferometry: Data Interpretation and Error Analysis*; Vol. 2, Springer Science & Business Media: Dordrecht, The Netherlands, 2001.
27. Elliott, J.; Biggs, J.; Parsons, B.; Wright, T. InSAR slip rate determination on the Altyn Tagh Fault, northern Tibet, in the presence of topographically correlated atmospheric delays. *Geophys. Res. Lett.* **2008**, *35*, doi:10.1029/2008GL033659.
28. Iglesias, R.; Fabregas, X.; Aguasca, A.; Mallorqui, J.J.; López-Martínez, C.; Gili, J.A.; Corominas, J. Atmospheric phase screen compensation in ground-based SAR with a multiple-regression model over mountainous regions. *IEEE Trans. Geosci. Remote Sens.* **2014**, *52*, 2436–2449. [[CrossRef](#)]
29. Hu, Z.; Mallorquí, J.J.; Centolanza, G.; Duro, J. InSAR atmospheric delays compensation: Case study in Tenerife island. In Proceedings of the 2017 IEEE International Geoscience and Remote Sensing Symposium (IGARSS), Fort Worth, TX, USA, 23–28 July 2017; pp. 3167–3170.

30. Bamler, R.; Eineder, M.; Adam, N.; Zhu, X.; Gernhardt, S. Interferometric potential of high resolution spaceborne SAR. *Photogramm.-Fernerkund.-Geoinf.* **2009**, *2009*, 407–419. [[CrossRef](#)]
31. Prati, C.; Ferretti, A.; Perissin, D. Recent advances on surface ground deformation measurement by means of repeated space-borne SAR observations. *J. Geodyn.* **2010**, *49*, 161–170. [[CrossRef](#)]
32. Lee, J.S.; Jurkevich, L.; Dewaele, P.; Wambacq, P.; Oosterlinck, A. Speckle filtering of synthetic aperture radar images: A review. *Remote Sens. Rev.* **1994**, *8*, 313–340. [[CrossRef](#)]
33. Daba, J.S.; Jreije, P. Advanced stochastic models for partially developed speckle. *World Acad. Sci. Eng. Technol.* **2008**, *41*, 566–570.
34. Lopes, A.; Nezry, E.; Touzi, R.; Laur, H. Structure detection and statistical adaptive speckle filtering in SAR images. *Int. J. Remote Sens.* **1993**, *14*, 1735–1758. [[CrossRef](#)]
35. Curlander, J.C.; McDonough, R.N. *Synthetic Aperture Radar*; John Wiley & Sons: New York, NY, USA, 1991; Volume 396.
36. Iglesias, R.; Mallorqui, J.J.; López-Dekker, P. DInSAR pixel selection based on sublook spectral correlation along time. *IEEE Trans. Geosci. Remote Sens.* **2014**, *52*, 3788–3799. [[CrossRef](#)]
37. Iglesias, R.; Mallorqui, J.J.; Monells, D.; López-Martínez, C.; Fabregas, X.; Aguasca, A.; Gili, J.A.; Corominas, J. PSI deformation map retrieval by means of temporal sublook coherence on reduced sets of SAR images. *Remote Sens.* **2015**, *7*, 530–563. [[CrossRef](#)]
38. Zhao, F.; Mallorqui, J.J. A temporal phase coherence estimation algorithm and its application on DInSAR pixel selection. *IEEE Trans. Geosci. Remote Sens.* **2018**, Undergoing Review.
39. Duque, S.; Breit, H.; Bals, U.; Parizzi, A. Absolute height estimation using a single TerraSAR-X staring spotlight acquisition. *IEEE Geosci. Remote Sens. Lett.* **2015**, *12*, 1735–1739. [[CrossRef](#)]
40. Tapete, D.; Cigna, F.; Donoghue, D.N. ‘Looting marks’ in space-borne SAR imagery: Measuring rates of archaeological looting in Apamea (Syria) with TerraSAR-X Staring Spotlight. *Remote Sens. Environ.* **2016**, *178*, 42–58. [[CrossRef](#)]
41. Corominas, J.; Alonso, E. Inestabilidad de Laderas en el Pirineo Catalán. Tipología y causas. In Proceedings of the Inestabilidad de laderas en el Pirineo, Barcelona, Spain, 16–17 January 1984; pp. 1–53.
42. Santacana, N. Estudi dels Grans Esllavissaments d’Andorra: Els Casos del Forn i del Vessant d’Encampadana. Master’s Thesis, Department of Dynamic Geology, Geophysics and Paleontology, Faculty of Geology, University of Barcelona, Barcelona, Spain, 1994.
43. Corominas, J.; Iglesias, R.; Aguasca, A.; Mallorquí, J.J.; Fàbregas, X.; Planas, X.; Gili, J.A. Comparing satellite based and ground based radar interferometry and field observations at the Canillo landslide (Pyrenees). In *Engineering Geology for Society and Territory-Volume 2*; Springer: Cham, Switzerland, 2015; pp. 333–337.
44. Torredadella, J.; Villaró, I.; Altimir, J.; Amigó, J.; Vilaplana, J.; Corominas, J.; Planas, X. El deslizamiento del Forn de Canillo en Andorra. Un ejemplo de gestión del riesgo geológico en zonas habitadas en grandes deslizamientos. In Proceedings of the VII Simposio Nacional Sobre Taludes y Laderas Inestables, Barcelona, Spain, 27–30 October 2009; pp. 403–414.
45. Mittermayer, J.; Wollstadt, S.; Prats-Iraola, P.; Scheiber, R. The TerraSAR-X staring spotlight mode concept. *IEEE Trans. Geosci. Remote Sens.* **2014**, *52*, 3695–3706. [[CrossRef](#)]
46. Eineder, M.; Adam, N.; Bamler, R.; Yague-Martínez, N.; Breit, H. Spaceborne spotlight SAR interferometry with TerraSAR-X. *IEEE Trans. Geosci. Remote Sens.* **2009**, *47*, 1524–1535. [[CrossRef](#)]
47. Davis, J.; Herring, T.; Shapiro, I.; Rogers, A.; Elgered, G. Geodesy by radio interferometry: Effects of atmospheric modeling errors on estimates of baseline length. *Radio Sci.* **1985**, *20*, 1593–1607. [[CrossRef](#)]
48. Cascini, L.; Fornaro, G.; Peduto, D. Advanced low-and full-resolution DInSAR map generation for slow-moving landslide analysis at different scales. *Eng. Geol.* **2010**, *112*, 29–42. [[CrossRef](#)]
49. Monserrat, O.; Moya, J.; Luzi, G.; Crosetto, M.; Gili, J.; Corominas, J. Non-interferometric GB-SAR measurement: Application to the Vallcebre landslide (eastern Pyrenees, Spain). *Nat. Hazards Earth Syst. Sci.* **2013**, *13*, 1873. [[CrossRef](#)]



5.3 Article 3. Coherency Matrix Decomposition Based Polarimetric Persistent Scatterer Interferometry

The content of this section corresponds to the publication: *Feng Zhao and Jordi Mal-lorqui. Coherency Matrix Decomposition Based Polarimetric Persistent Scatterer Interferometry[J]. IEEE Transactions on Geoscience and Remote Sensing, 2019 [80].*

Attention

Pages 87 to 99 of the thesis are available at the editor's web
<https://ieeexplore.ieee.org/abstract/document/8734735>

5.4 Article 4. SMF-POLOPT: An Adaptive Multi-temporal Pol(DIn)SAR Filtering and Phase Optimization Algorithm for PSI Applications

The content of this section corresponds to the publication: *Feng Zhao and Jordi Mallorqui. SMF-POLOPT: An Adaptive Multi-temporal Pol(DIn)SAR Filtering and Phase Optimization Algorithm for PSI Applications[J]. IEEE Transactions on Geoscience and Remote Sensing, 2019* [81].

Attention

Pages 101 to 113 of the thesis are available at the editor's web
<https://ieeexplore.ieee.org/document/8709996>

5.5 List of Conference Articles

The conference articles generated during the development of this thesis are listed as follows:

1. Zhao, Feng, and Jordi J. Mallorqui. "An Adaptive Scattering-Mechanism-Based Filtering for Multitemporal Pol(In)SAR Data." In EUSAR 2018; 12th European Conference on Synthetic Aperture Radar, pp. 1-4. VDE, 2018.
2. Zhao, Feng, and Jordi J. Mallorqui. "A Temporal Phase Coherence Estimation Algorithm." In EUSAR 2018; 12th European Conference on Synthetic Aperture Radar, pp. 1-4. VDE, 2018.
3. Zhao, Feng, and Jordi J. Mallorqui. "An Adaptive Multilooking Scheme for Multitemporal InSAR Data." In IGARSS 2018-2018 IEEE International Geoscience and Remote Sensing Symposium, pp. 2204-2207. IEEE, 2018.

ACRONYMS

APS Atmospheric Phase Screen

CDS Coherent Distributed Scatterer

CPT Coherent Pixel Technique

CS Coherent Scatterer

D_A Dispersion of Amplitude

DEM Digital Elevation Model

DInSAR Differential Interferometry SAR

DS Distributed Scatterer

GPS Global Positioning System

HP Homogeneous Pixel

InSAR Interferometry SAR

LDEB Linear Deformation Estimation Block

LOS Line of Sight

MTInSAR Multi-Temporal InSAR

NLDEB Non-linear Deformation Estimation Block

PDF Probability density function

PHP Polarimetric Homogeneous Pixel

PolInSAR Polarimetric SAR interferometry

PolPSI Polarimetric Permanent Scatterer Interferometry

PRF Pulse Repetition Frequency

PS Permanent Scatterer

PSC Persistent Scatterer Candidate

PSI Persistent Scatterer Interferometry

RAR Real Aperture Radar

RDS Random Distributed Scatterer

SAR Synthetic Aperture Radar

SHP Statistically Homogeneous Pixel

SHR Super High-spatial Resolution

SNR Signal to Noise Ratio

SLC Single Look Complex

SLR Spatial Low Resolution

STD Standard Deviation

SVD Singular Value Decomposition

TPC Temporal Phase Coherence

TSC Temporal Sublook Coherence

UPC Universitat Politècnica de Catalunya

LIST OF FIGURES

1.1	Two categories of pixels.	3
1.2	Standard deviation of the phase as a function of (a) D_A , (b) TSC for the data set of 32 SAR images.	4
1.3	Interferometric phase standard deviation vs. coherence for different number of effective looks (different color lines).	6
1.4	Coherence estimator validity: (a) True coherence γ_{SPC} vs estimated coherence $\hat{\gamma}_{SPC}$. (b) True coherence γ_{SPC} vs coherence estimation STD. Lines of different colors shows the cases of different effective looks.	7
2.1	SAR acquisition geometry.	12
2.2	Synthetic aperture radar concept.	13
2.3	Geometrical acquisition distortions.	14
2.4	Interferogram acquisition geometry.	15
2.5	Diagram for the estimation of the linear components of CPT.	18
2.6	Diagram for the estimation of the non-linear displacement of CPT.	20
3.1	Deformation velocity map in Barcelona "El Prat" Airport retrieved by (a) the PS (D_A) approach, (b) the classical spatial coherence (SPC) approach, and (c) the proposed temporal phase coherence (TPC) approach. The number in the bracket represents the amount of selected pixels by each approach.	27
3.2	LOS displacement velocity maps derived by (a) D_A , (b) TSC, (c) TPC and (d) GPS approaches, respectively. The filled blue triangle in (d), i.e., E1, indicates the location of the GPS base point. GPS displacements have been projected to LOS. The red rectangles highlight the areas of deformation. The red numbers at the right bottom corner of (a–c) represent the amount of valid pixels obtained by each method.	30
3.3	Comparison of PSI and GPS derived displacements (October 2014 to October 2016).	31
3.4	(a) Dispersion of amplitude (D_A) histograms using HH polarimetric channel or the SM1, BEST, SM-BEST, ESM and the proposed CMD-PolPSI D_A optimization methods over Barcelona. (b) Detail for D_A values from 0 to 0.25.	33

3.5	Ground deformation estimated by (a) HH, (b) BEST, (c) CMD-PolPSI and (e) ESM approaches over Barcelona . (d) the additional pixels of CMD-PolPSI w.r.t. BEST, and (f) the additional pixels of ESM w.r.t. CMD-PolPSI. The number in brackets represents the final number of PS pixels for each approach, and the improvement percentage is w.r.t. those derived by the HH approach.	35
3.6	Original and filtered Pauli RGB composites over the Barcelona airport. Bottom row shows the close-up of the area limited by the red rectangle in the top row. The color channels are $R = HH - VV$, $G = 2HV$, and $B = HH + VV$	37
3.7	An interferogram phase optimization results of Barcelona airport by different algorithms. The black dashed lines in (a) indicate the locations of roads where the SMF-POLOPT approach presents the best optimization effect.	38
3.8	Close-up of the phase optimization results of Fig 3.7, which corresponds to the area of the airport terminal.	39
3.9	Barcelona airport ground deformation velocity maps obtained by (a) D_A , (b) ESM, (c) SMF and (d) SMF-POLOPT. The number in the brackets represents the amount of pixels in each algorithm derived deformation result.	40

BIBLIOGRAPHY

- [1] J. Almendros, J. M. Ibáñez, E. Carmona, and D. Zandomenighi, “Array analyses of volcanic earthquakes and tremor recorded at las cañadas caldera (tenerife island, spain) during the 2004 seismic activation of teide volcano,” *Journal of Volcanology and Geothermal Research*, vol. 160, no. 3-4, pp. 285–299, 2007. (Cited on page 1.)
- [2] J. Fernández, P. Tizzani, M. Manzo, A. Borgia, P. González, J. Martí, A. Pepe, A. Camacho, F. Casu, P. Berardino *et al.*, “Gravity-driven deformation of tenerife measured by insar time series analysis,” *Geophysical Research Letters*, vol. 36, no. 4, 2009. (Cited on page 1.)
- [3] A. H.-M. Ng, L. Ge, X. Li, and K. Zhang, “Monitoring ground deformation in beijing, china with persistent scatterer sar interferometry,” *Journal of Geodesy*, vol. 86, no. 6, pp. 375–392, 2012. (Cited on page 1.)
- [4] S. V. Samsonov, N. d’Oreye, P. J. González, K. F. Tiampo, L. Ertolahti, and J. J. Clague, “Rapidly accelerating subsidence in the greater vancouver region from two decades of ers-envisat-radarsat-2 dinsar measurements,” *Remote sensing of environment*, vol. 143, pp. 180–191, 2014. (Cited on page 1.)
- [5] A. H.-M. Ng, L. Ge, and X. Li, “Assessments of land subsidence in the gippsland basin of australia using alos palsar data,” *Remote Sensing of Environment*, vol. 159, pp. 86–101, 2015. (Cited on page 1.)
- [6] R. Bamler and P. Hartl, “Synthetic aperture radar interferometry,” *Inverse problems*, vol. 14, no. 4, p. R1, 1998. (Cited on pages 1 and 5.)
- [7] A. K. Gabriel, R. M. Goldstein, and H. A. Zebker, “Mapping small elevation changes over large areas: differential radar interferometry,” *Journal of Geophysical Research: Solid Earth*, vol. 94, no. B7, pp. 9183–9191, 1989. (Cited on page 1.)
- [8] R. Bürgmann, P. A. Rosen, and E. J. Fielding, “Synthetic aperture radar interferometry to measure earth’s surface topography and its deformation,” *Annual review of earth and planetary sciences*, vol. 28, no. 1, pp. 169–209, 2000. (Cited on page 1.)

- [9] H. A. Zebker and J. Villasenor, “Decorrelation in interferometric radar echoes,” *IEEE Transactions on geoscience and remote sensing*, vol. 30, no. 5, pp. 950–959, 1992. (Cited on pages 1 and 2.)
- [10] A. Ferretti, C. Prati, and F. Rocca, “Permanent scatterers in sar interferometry,” *IEEE Transactions on geoscience and remote sensing*, vol. 39, no. 1, pp. 8–20, 2001. (Cited on pages 1, 2, 3, 4, 17, and 32.)
- [11] —, “Permanent scatterers in sar interferometry,” in *IEEE 1999 International Geoscience and Remote Sensing Symposium. IGARSS’99 (Cat. No. 99CH36293)*, vol. 3. IEEE, 1999, pp. 1528–1530. (Cited on pages 2 and 17.)
- [12] P. Berardino, G. Fornaro, R. Lanari, and E. Sansosti, “A new algorithm for surface deformation monitoring based on small baseline differential SAR interferograms,” *IEEE Transactions on Geoscience and Remote Sensing*, vol. 40, no. 11, pp. 2375–2383, 2002. (Cited on pages 2, 5, and 17.)
- [13] O. Mora, J. J. Mallorqui, and A. Broquetas, “Linear and nonlinear terrain deformation maps from a reduced set of interferometric SAR images,” *IEEE Transactions on Geoscience and Remote Sensing*, vol. 41, no. 10, pp. 2243–2253, 2003. (Cited on pages 2, 5, 9, and 17.)
- [14] R. Lanari, O. Mora, M. Manunta, J. J. Mallorquí, P. Berardino, and E. Sansosti, “A small-baseline approach for investigating deformations on full-resolution differential SAR interferograms,” *IEEE Transactions on Geoscience and Remote Sensing*, vol. 42, no. 7, pp. 1377–1386, 2004. (Cited on pages 2, 5, and 17.)
- [15] A. Hooper, H. Zebker, P. Segall, and B. Kampes, “A new method for measuring deformation on volcanoes and other natural terrains using InSAR persistent scatterers,” *Geophysical research letters*, vol. 31, no. 23, 2004. (Cited on pages 2, 5, 7, 17, and 26.)
- [16] A. Hooper, P. Segall, and H. Zebker, “Persistent scatterer interferometric synthetic aperture radar for crustal deformation analysis, with application to volcán alcedo, galápagos,” *Journal of Geophysical Research: Solid Earth*, vol. 112, no. B7, 2007. (Cited on pages 2, 3, 5, 17, and 26.)
- [17] P. Blanco-Sanchez, J. J. Mallorquí, S. Duque, and D. Monells, “The coherent pixels technique (CPT): An advanced DInSAR technique for nonlinear deformation monitoring,” *Pure and Applied Geophysics*, vol. 165, no. 6, pp. 1167–1193, 2008. (Cited on pages 2, 5, 9, and 17.)
- [18] A. Ferretti, A. Fumagalli, F. Novali, C. Prati, F. Rocca, and A. Rucci, “A new algorithm for processing interferometric data-stacks: SqueeSAR,” *IEEE Transactions on Geoscience and Remote Sensing*, vol. 49, no. 9, pp. 3460–3470, 2011. (Cited on pages 2, 3, 8, 17, and 36.)

- [19] R. Iglesias, J. J. Mallorqui, and P. López-Dekker, “DInSAR pixel selection based on sublook spectral correlation along time.” *IEEE Trans. Geoscience and Remote Sensing*, vol. 52, no. 7, pp. 3788–3799, 2014. (Cited on pages 2, 4, 7, and 17.)
- [20] G. Fornaro, S. Verde, D. Reale, and A. Pauciuolo, “CAESAR: An approach based on covariance matrix decomposition to improve multibaseline–multitemporal interferometric SAR processing,” *IEEE Transactions on Geoscience and Remote Sensing*, vol. 53, no. 4, pp. 2050–2065, 2015. (Cited on pages 2, 3, 8, and 17.)
- [21] G. Savio, A. Ferretti, F. Novali, S. Musazzi, C. Prati, and F. Rocca, “PSInSAR validation by means of a blind experiment using dihedral reflectors,” in *FRINGE 2005 workshop*, vol. 610, 2006. (Cited on page 2.)
- [22] F. Casu, M. Manzo, and R. Lanari, “A quantitative assessment of the SBAS algorithm performance for surface deformation retrieval from DInSAR data,” *Remote Sensing of Environment*, vol. 102, no. 3-4, pp. 195–210, 2006. (Cited on page 2.)
- [23] D. Perissin and A. Ferretti, “Urban-target recognition by means of repeated spaceborne SAR images,” *IEEE Transactions on Geoscience and Remote Sensing*, vol. 45, no. 12, pp. 4043–4058, 2007. (Cited on page 2.)
- [24] D. Perissin and T. Wang, “Repeat-pass SAR interferometry with partially coherent targets,” *IEEE Transactions on Geoscience and Remote Sensing*, vol. 50, no. 1, pp. 271–280, 2012. (Cited on page 4.)
- [25] R. Z. Schneider, K. P. Papathanassiou, I. Hajnsek, and A. Moreira, “Polarimetric and interferometric characterization of coherent scatterers in urban areas,” *IEEE Transactions on Geoscience and Remote Sensing*, vol. 44, no. 4, pp. 971–984, 2006. (Cited on page 4.)
- [26] P. Shanker and H. Zebker, “Persistent scatterer selection using maximum likelihood estimation,” *Geophysical Research Letters*, vol. 34, no. 22, 2007. (Cited on page 5.)
- [27] K. Ishitsuka, T. Matsuoka, and M. Tamura, “Persistent scatterer selection incorporating polarimetric SAR interferograms based on maximum likelihood theory,” *IEEE Transactions on Geoscience and Remote Sensing*, vol. 55, no. 1, pp. 38–50, 2017. (Cited on pages 5 and 7.)
- [28] S. Samsonov and K. Tiampo, “Polarization phase difference analysis for selection of persistent scatterers in SAR interferometry,” *IEEE Geoscience and Remote Sensing Letters*, vol. 8, no. 2, pp. 331–335, 2011. (Cited on page 5.)
- [29] G. Kouroupis and V. Anastassopoulos, “Polarimetric decomposition for the selection of persistent scatterers,” *Remote sensing letters*, vol. 8, no. 3, pp. 271–279, 2017. (Cited on page 5.)

- [30] S. Navneet, J.-W. Kim, and Z. Lu, “A New InSAR Persistent Scatterer Selection Technique Using Top Eigenvalue of Coherence Matrix,” *IEEE Transactions on Geoscience and Remote Sensing*, vol. 56, no. 4, pp. 1969–1978, 2018. (Cited on page 5.)
- [31] T. Tanaka and O. Hoshuyama, “Cluster Based Method to Identify Persistent Scatterers for Nonlinear Displacement Analysis of Structures,” in *IGARSS 2018-2018 IEEE International Geoscience and Remote Sensing Symposium*. IEEE, 2018, pp. 2180–2183. (Cited on page 5.)
- [32] R. F. Hanssen, *Radar interferometry: data interpretation and error analysis*. Springer Science & Business Media, 2001, vol. 2. (Cited on page 5.)
- [33] L. Pipia, X. Fabregas, A. Aguasca, C. Lopez-Martinez, S. Duque, J. J. Mallorqui, and J. Marturia, “Polarimetric differential SAR interferometry: First results with ground-based measurements,” *IEEE Geoscience and Remote Sensing Letters*, vol. 6, no. 1, pp. 167–171, 2009. (Cited on page 7.)
- [34] V. D. Navarro-Sanchez, J. M. Lopez-Sanchez, and F. Vicente-Guijalba, “A contribution of polarimetry to satellite differential SAR interferometry: Increasing the number of pixel candidates,” *IEEE Geoscience and Remote Sensing Letters*, vol. 7, no. 2, pp. 276–280, 2010. (Cited on pages 7 and 23.)
- [35] V. D. Navarro-Sanchez, J. M. Lopez-Sanchez, and L. Ferro-Famil, “Polarimetric approaches for persistent scatterers interferometry,” *IEEE Transactions on Geoscience and Remote Sensing*, vol. 52, no. 3, pp. 1667–1676, 2014. (Cited on pages 7, 22, 26, and 39.)
- [36] R. Iglesias, D. Monells, X. Fabregas, J. J. Mallorqui, A. Aguasca, and C. Lopez-Martinez, “Phase quality optimization in polarimetric differential SAR interferometry,” *IEEE transactions on geoscience and remote sensing*, vol. 52, no. 5, pp. 2875–2888, 2014. (Cited on pages 7, 22, 23, 24, 26, 36, 39, and 45.)
- [37] D. Monells, R. Iglesias, J. J. Mallorquí, X. Fàbregas, and C. Lopez-Martinez, “Phase quality optimization in orbital differential SAR interferometry with fully polarimetric data,” in *Geoscience and Remote Sensing Symposium (IGARSS), 2012 IEEE International*. IEEE, 2012, pp. 1864–1867. (Cited on page 7.)
- [38] R. Iglesias, X. Fabregas, A. Aguasca, C. López-Martínez, and A. Alonso-González, “Advanced polarimetric optimization for DInSAR applications with ground-based SAR,” in *Synthetic Aperture Radar, 2012. EUSAR. 9th European Conference on. VDE*, 2012, pp. 513–516. (Cited on page 7.)
- [39] V. D. Navarro-Sanchez and J. M. Lopez-Sanchez, “Improvement of persistent-scatterer interferometry performance by means of a polarimetric optimization,” *IEEE Geoscience and Remote Sensing Letters*, vol. 9, no. 4, pp. 609–613, 2012. (Cited on

page 7.)

- [40] R. Iglesias, D. Monells, X. Fabregas, J. J. Mallorqui, A. Aguasca, and C. Lopez-Martínez, “Phase quality optimization techniques and limitations in polarimetric differential SAR interferometry,” *transformation*, vol. 17, p. 18, 2013. (Cited on pages 7 and 21.)
- [41] B. Wu, L. Tong, Y. Chen, and L. He, “New methods in multibaseline polarimetric SAR interferometry coherence optimization,” *IEEE Geoscience and Remote Sensing Letters*, vol. 12, no. 10, pp. 2016–2020, 2015. (Cited on pages 7 and 32.)
- [42] —, “Improved SNR optimum method in PolDInSAR coherence optimization,” *IEEE Geoscience and Remote Sensing Letters*, vol. 13, no. 7, pp. 982–986, 2016. (Cited on pages 7 and 32.)
- [43] Z. Sadeghi, M. J. V. Zoj, and J.-P. Muller, “Monitoring land subsidence in a rural area using a combination of ADInSAR and polarimetric coherence optimization,” *IEEE Journal of Selected Topics in Applied Earth Observations and Remote Sensing*, vol. 10, no. 8, pp. 3582–3590, 2017. (Cited on page 7.)
- [44] M. Esmaili and M. Motagh, “Improved persistent scatterer analysis using amplitude dispersion index optimization of dual polarimetry data,” *ISPRS Journal of Photogrammetry and Remote Sensing*, vol. 117, pp. 108–114, 2016. (Cited on page 7.)
- [45] M. Esmaili, M. Motagh, and A. Hooper, “Application of dual-polarimetry SAR images in multitemporal InSAR processing,” *IEEE Geoscience and Remote Sensing Letters*, vol. 14, no. 9, pp. 1489–1493, 2017. (Cited on page 7.)
- [46] A. G. Mullissa, V. Tolpekin, A. Stein, and D. Perissin, “Polarimetric differential SAR interferometry in an arid natural environment,” *International journal of applied earth observation and geoinformation*, vol. 59, pp. 9–18, 2017. (Cited on page 7.)
- [47] A. G. Mullissa, D. Perissin, V. A. Tolpekin, and A. Stein, “Polarimetry-based distributed scatterer processing method for PSI applications,” *IEEE transactions on geoscience and remote sensing*, vol. 56, no. 6, pp. 3371–3382, 2018. (Cited on pages 7 and 8.)
- [48] Z. Sadeghi, M. J. V. Zoj, and J.-P. Muller, “Combination of persistent scatterer interferometry and single-baseline polarimetric coherence optimisation to estimate deformation rates with application to tehran basin,” *PFG–Journal of Photogrammetry, Remote Sensing and Geoinformation Science*, vol. 85, no. 5, pp. 327–340, 2017. (Cited on page 7.)
- [49] R. Iglesias, D. Monells, C. López-Martínez, J. J. Mallorqui, X. Fabregas, and A. Aguasca, “Polarimetric optimization of temporal sublook coherence for DInSAR

- applications,” *IEEE Geoscience and Remote Sensing Letters*, vol. 12, no. 1, pp. 87–91, 2015. (Cited on page 7.)
- [50] Z. Sadeghi, M. J. V. Zojj, A. Hooper, and J. M. Lopez-Sanchez, “A new polarimetric persistent scatterer interferometry method using temporal coherence optimization,” *IEEE Transactions on Geoscience and Remote Sensing*, no. 99, pp. 1–9, 2018. (Cited on page 7.)
- [51] Y. Wang, X. Zhu, and R. Bamler, “Retrieval of phase history parameters from distributed scatterers in urban areas using very high resolution SAR data,” *ISPRS Journal of Photogrammetry and Remote Sensing*, vol. 73, pp. pp–89, 2012. (Cited on page 8.)
- [52] K. Goel and N. Adam, “A distributed scatterer interferometry approach for precision monitoring of known surface deformation phenomena,” *IEEE Transactions on Geoscience and Remote Sensing*, vol. 52, no. 9, pp. 5454–5468, 2014. (Cited on page 8.)
- [53] Y. Morishita and R. F. Hanssen, “Deformation parameter estimation in low coherence areas using a multisatellite InSAR approach,” *IEEE Transactions on Geoscience and Remote Sensing*, vol. 53, no. 8, pp. 4275–4283, 2015. (Cited on page 8.)
- [54] M. Jiang, X. Ding, R. F. Hanssen, R. Malhotra, and L. Chang, “Fast statistically homogeneous pixel selection for covariance matrix estimation for multitemporal InSAR,” *IEEE transactions on geoscience and remote sensing*, vol. 53, no. 3, pp. 1213–1224, 2015. (Cited on page 8.)
- [55] M. A. Stephens, “Use of the Kolmogorov-Smirnov, cramér-von Mises and related statistics without extensive tables,” *Journal of the Royal Statistical Society. Series B (Methodological)*, pp. 115–122, 1970. (Cited on page 8.)
- [56] A. Parizzi and R. Brcic, “Adaptive InSAR stack multilooking exploiting amplitude statistics: A comparison between different techniques and practical results,” *IEEE Geoscience and Remote Sensing Letters*, vol. 8, no. 3, pp. 441–445, 2011. (Cited on page 8.)
- [57] N. Cao, H. Lee, and H. C. Jung, “A phase-decomposition-based PSInSAR processing method,” *IEEE Transactions on Geoscience and Remote Sensing*, vol. 54, no. 2, pp. 1074–1090, 2016. (Cited on page 8.)
- [58] V. D. Navarro-Sanchez and J. M. Lopez-Sanchez, “Spatial adaptive speckle filtering driven by temporal polarimetric statistics and its application to PSI,” *IEEE Transactions on Geoscience and Remote Sensing*, vol. 52, no. 8, pp. 4548–4557, 2014. (Cited on pages 8, 22, 23, 26, 36, 39, and 45.)
- [59] M. I. Skolnik, *Introduction to Radar Systems*. McGraw-Hill, 1981. (Cited on

page 12.)

- [60] J. C. Curlander and R. N. McDonough, *Synthetic Aperture Radar: Systems and Signal Processing*. New York, USA: John Wiley & Sons, Inc., 1992. (Cited on page 13.)
- [61] G. Franceschetti and R. Lanari, *Synthetic Aperture Radar Processing*. Taylor & Francis, 1999. (Cited on page 13.)
- [62] I. G. Cumming and F. H.-C. Wong, *Digital Signal Processing of Synthetic Aperture Radar Data: Algorithms and Implementation*. Artech House, Inc., 2005. (Cited on page 13.)
- [63] M. Costantini, “A novel phase unwrapping method based on network programming,” *IEEE Transactions on Geoscience and Remote Sensing*, vol. 36, no. 3, pp. 813–821, May 1998. (Cited on page 16.)
- [64] C. W. Chen and H. A. Zebker, “Two-dimensional phase unwrapping with use of statistical models for cost functions in nonlinear optimization,” *Journal of the Optical Society of America A*, vol. 18, no. 2, p. 338, 2001. (Cited on page 16.)
- [65] —, “Phase unwrapping for large SAR interferograms: statistical segmentation and generalized network models,” *IEEE Transactions on Geoscience and Remote Sensing*, vol. 40, no. 8, pp. 1709–1719, Aug. 2002. (Cited on page 16.)
- [66] G. Herrera, R. Tomás, F. Vicente, J. Lopez-Sanchez, J. Mallorquí, and J. Mulas, “Mapping ground movements in open pit mining areas using differential sar interferometry,” *International Journal of Rock Mechanics and Mining Sciences*, vol. 47, no. 7, pp. 1114–1125, 2010. (Cited on page 17.)
- [67] D. Di Martire, R. Iglesias, D. Monells, G. Centolanza, S. Sica, M. Ramondini, L. Pagano, J. J. Mallorquí, and D. Calcaterra, “Comparison between differential sar interferometry and ground measurements data in the displacement monitoring of the earth-dam of conza della campania (italy),” *Remote sensing of environment*, vol. 148, pp. 58–69, 2014. (Cited on page 17.)
- [68] R. Tomás, M. Cano, J. Garcia-Barba, F. Vicente, G. Herrera, J. M. Lopez-Sanchez, and J. Mallorquí, “Monitoring an earthfill dam using differential sar interferometry: La pedrera dam, alicante, spain,” *Engineering geology*, vol. 157, pp. 21–32, 2013. (Cited on page 17.)
- [69] P. Confuorto, D. Di Martire, G. Centolanza, R. Iglesias, J. J. Mallorqui, A. Novellino, S. Plank, M. Ramondini, K. Thuro, and D. Calcaterra, “Post-failure evolution analysis of a rainfall-triggered landslide by multi-temporal interferometry sar approaches integrated with geotechnical analysis,” *Remote sensing of environment*, vol. 188, pp.

- 51–72, 2017. (Cited on page 17.)
- [70] A. Pulido-Bosch, J. Delgado, F. Sola, Á. Vallejos, F. Vicente, J. M. López-Sánchez, and J. J. Mallorquí, “Identification of potential subsidence related to pumping in the almería basin (se spain),” *Hydrological processes*, vol. 26, no. 5, pp. 731–740, 2012. (Cited on page 17.)
- [71] J. Fernandez, J. F. Prieto, J. Escayo, A. G. Camacho, F. Luzón, K. F. Tiampo, M. Palano, T. Abajo, E. Pérez, J. Velasco *et al.*, “Modeling the two-and three-dimensional displacement field in lorca, spain, subsidence and the global implications,” *Scientific reports*, vol. 8, 2018. (Cited on page 17.)
- [72] G. Bru, J. Escayo, J. Fernández, J. Mallorqui, R. Iglesias, E. Sansosti, T. Abajo, and A. Morales, “Suitability assessment of x-band satellite sar data for geotechnical monitoring of site scale slow moving landslides,” *Remote Sensing*, vol. 10, no. 6, p. 936, 2018. (Cited on page 17.)
- [73] P. Blanco-Sanchez, “SAR Differential Interferometry for deformation monitoring under a multi-frequency approach,” Ph.D. dissertation, Ph. D. Thesis, Universitat Politècnica de Catalunya, Barcelona, Spain, 2009. (Cited on pages 17, 18, and 19.)
- [74] R. Iglesias, “High-Resolution Space-Borne and Ground-Based SAR Persistent Scatterer Interferometry for Landslide Monitoring,” Ph.D. dissertation, Ph. D. Thesis, Universitat Politècnica de Catalunya, Barcelona, Spain, 2015. (Cited on pages 18 and 19.)
- [75] S. R. Cloude and K. P. Papathanassiou, “Polarimetric SAR interferometry,” *IEEE Transactions on Geoscience and Remote Sensing*, vol. 36, no. 5, pp. 1551–1565, 1998. (Cited on pages 21, 22, and 23.)
- [76] J.-S. Lee and E. Pottier, *Polarimetric radar imaging: from basics to applications*. CRC press, 2009. (Cited on pages 22, 23, 46, and 47.)
- [77] F. Zhao and J. J. Mallorqui, “A Temporal Phase Coherence Estimation Algorithm and Its Application on DInSAR Pixel Selection,” *IEEE Transactions on Geoscience and Remote Sensing*, pp. 1–12, 2019. (Cited on pages 25, 26, 28, 32, 41, 46, and 49.)
- [78] F. Zhao, J. J. Mallorqui, R. Iglesias, J. Gili, and J. Corominas, “Landslide monitoring using multi-temporal SAR interferometry with advanced persistent scatterers identification methods and super high-spatial resolution TerraSAR-X images,” *Remote Sensing*, vol. 10, no. 6, p. 921, 2018. (Cited on pages 28, 29, 32, 41, 42, 46, and 62.)
- [79] R. Iglesias, J. J. Mallorqui, D. Monells, C. López-Martínez, X. Fabregas, A. Aguasca, J. A. Gili, and J. Corominas, “Psi deformation map retrieval by means of temporal

- sublook coherence on reduced sets of sar images,” *Remote Sensing*, vol. 7, no. 1, pp. 530–563, 2015. (Cited on page 29.)
- [80] F. Zhao and J. J. Mallorqui, “Coherency Matrix Decomposition Based Polarimetric Persistent Scatterer Interferometry,” *IEEE Transactions on Geoscience and Remote Sensing*, pp. 1–13, 2019. (Cited on pages 31, 32, 33, 34, 36, 41, 44, 46, and 86.)
- [81] —, “SMF-POLOPT: An Adaptive Multitemporal Pol(DIn)SAR Filtering and Phase Optimization Algorithm for PSI Applications,” *IEEE Transactions on Geoscience and Remote Sensing*, pp. 1–13, 2019. (Cited on pages 36, 37, 38, 39, 41, 45, 46, 47, and 100.)
- [82] J.-S. Lee, M. R. Grunes, D. L. Schuler, E. Pottier, and L. Ferro-Famil, “Scattering-model-based speckle filtering of polarimetric SAR data,” *IEEE Transactions on Geoscience and Remote Sensing*, vol. 44, no. 1, pp. 176–187, 2006. (Cited on pages 36, 37, and 45.)
- [83] J.-S. Lee, M. R. Grunes, and G. De Grandi, “Polarimetric SAR speckle filtering and its implication for classification,” *IEEE Transactions on Geoscience and remote sensing*, vol. 37, no. 5, pp. 2363–2373, 1999. (Cited on page 36.)
- [84] G. Vasile, E. Trouvé, J.-S. Lee, and V. Buzuloiu, “Intensity-driven adaptive-neighborhood technique for polarimetric and interferometric SAR parameters estimation,” *IEEE Transactions on Geoscience and Remote Sensing*, vol. 44, no. 6, pp. 1609–1621, 2006. (Cited on pages 37 and 45.)
- [85] C.-A. Deledalle, L. Denis, F. Tupin, A. Reigber, and M. Jäger, “NL-SAR: A unified nonlocal framework for resolution-preserving (Pol)(In) SAR denoising,” *IEEE Transactions on Geoscience and Remote Sensing*, vol. 53, no. 4, pp. 2021–2038, 2015. (Cited on page 46.)
- [86] Y. Yamaguchi, T. Moriyama, M. Ishido, and H. Yamada, “Four-component scattering model for polarimetric SAR image decomposition,” *IEEE Transactions on Geoscience and Remote Sensing*, vol. 43, no. 8, pp. 1699–1706, 2005. (Cited on page 46.)
- [87] Y. Yamaguchi, Y. Yajima, and H. Yamada, “A four-component decomposition of polsar images based on the coherency matrix,” *IEEE Geoscience and Remote Sensing Letters*, vol. 3, no. 3, pp. 292–296, 2006. (Cited on page 46.)
- [88] Y. Yamaguchi, A. Sato, W.-M. Boerner, R. Sato, and H. Yamada, “Four-component scattering power decomposition with rotation of coherency matrix,” *IEEE Transactions on Geoscience and Remote Sensing*, vol. 49, no. 6, pp. 2251–2258, 2011. (Cited on page 46.)
- [89] J.-S. Lee, M. R. Grunes, T. L. Ainsworth, L.-J. Du, D. L. Schuler, and S. R.

- Cloude, “Unsupervised classification using polarimetric decomposition and the complex Wishart classifier,” *IEEE Transactions on Geoscience and Remote Sensing*, vol. 37, no. 5, pp. 2249–2258, 1999. (Cited on page 47.)
- [90] E. Pottier and J.-S. Lee, “Application of the H/A/alpha polarimetric decomposition theorem for unsupervised classification of fully polarimetric SAR data based on the wishart distribution,” in *SAR workshop: CEOS Committee on Earth Observation Satellites*, vol. 450, 2000, p. 335. (Cited on page 47.)
- [91] L. Ferro-Famil, E. Pottier, and J.-S. Lee, “Unsupervised classification of multifrequency and fully polarimetric SAR images based on the H/A/Alpha-Wishart classifier,” *IEEE Transactions on Geoscience and Remote Sensing*, vol. 39, no. 11, pp. 2332–2342, 2001. (Cited on page 47.)
- [92] X. X. Zhu, D. Tuia, L. Mou, G.-S. Xia, L. Zhang, F. Xu, and F. Fraundorfer, “Deep learning in remote sensing: A comprehensive review and list of resources,” *IEEE Geoscience and Remote Sensing Magazine*, vol. 5, no. 4, pp. 8–36, 2017. (Cited on page 47.)
- [93] C. Henry, S. M. Azimi, and N. Merkle, “Road Segmentation in SAR Satellite Images With Deep Fully Convolutional Neural Networks,” *IEEE Geoscience and Remote Sensing Letters*, no. 99, pp. 1–5, 2018. (Cited on page 47.)
- [94] W. Wu, H. Li, X. Li, H. Guo, and L. Zhang, “PolSAR Image Semantic Segmentation Based on Deep Transfer Learning—Realizing Smooth Classification With Small Training Sets,” *IEEE Geoscience and Remote Sensing Letters*, 2019. (Cited on page 47.)
- [95] F. Mohammadimanesh, B. Salehi, M. Mahdianpari, E. Gill, and M. Molinier, “A new fully convolutional neural network for semantic segmentation of polarimetric SAR imagery in complex land cover ecosystem,” *ISPRS Journal of Photogrammetry and Remote Sensing*, vol. 151, pp. 223–236, 2019. (Cited on page 47.)
- [96] H. Bi, J. Sun, and Z. Xu, “A Graph-Based Semisupervised Deep Learning Model for PolSAR Image Classification,” *IEEE Transactions on Geoscience and Remote Sensing*, vol. 57, no. 4, pp. 2116–2132, 2019. (Cited on page 47.)